Title
Exploring the Wind-Driven Near-Antarctic Circulation

Author
Hazel, Julia Eileen

Publication Date
2019

Peer reviewed|Thesis/dissertation

UNIVERSITY OF CALIFORNIA

Los Angeles

Exploring the Wind-Driven

Near-Antarctic Circulation

A dissertation submitted in partial satisfaction

of the requirements for the degree

Doctor of Philosophy in Atmospheric and Oceanic Sciences

by

Julia Eileen Hazel

2019

ABSTRACT OF THE DISSERTATION

Exploring the Wind-Driven
Near-Antarctic Circulation

by

Julia Eileen Hazel
Doctor of Philosophy in Atmospheric and Oceanic Sciences
University of California, Los Angeles, 2019
Professor Andrew Leslie Stewart, Chair

The circulation at the margins of Antarctica closes the meridional overturning circulation, ventilating the abyssal ocean with 0_2 and modulating deep CO_2 storage on millennial timescales. This circulation also mediates the melt rates of Antarctica's floating ice shelves, and thereby exerts a strong influence on future global sea level rise. The near-Antarctic circulation has been hypothesized to respond sensitively to changes in the easterly winds that encircle the Antarctic coastline. In particular, the easterlies may be expected to weaken in response to the ongoing strengthening and poleward shifting of the mid-latitude westerlies, associated with a trend toward the positive index of the Southern Annular Mode (SAM). However, multi-decadal changes in the easterlies have not been systematically quantified, and previous studies have yielded limited insight into the oceanic response to such changes.

In this work we first quantify multi-decadal changes in wind forcing of the near-Antarctic ocean using a suite of reanalysis products that compare favorably with local meteorological measurements. Contrary to expectations, we find that the circumpolar-averaged easterly wind stress has not weakened over the past 3-4 decades, and if anything has slightly strengthened. However, there has been a substantial increase in the seasonality of the easterlies: our results suggest that in austral summer the intensification of the SAM has weakened the easterly winds, while during austral winter an intensification of Antarctica's katabatic winds has strengthened the easterlies. These trends have wide-ranging implications for oceanic transport of heat to Antarctica's floating

glaciers, formation of dense waters on the continental shelf, and sea ice production and export.

To explore the impacts of Antarctica' changing winds, we develop a comprehensive model of the southern Weddell Sea, including the Filchner-Ronne Ice Shelf (FRIS), Antarctica's largest floating glacier. We investigate the wind-driven sensitivity of the circulation, dense water production, and glacial melt to idealized climate changes. We find that the circulation is relatively insensitive to changes in the zonal winds and atmospheric temperature, but strongly sensitive to changes in the meridional winds. Varying the strength of the meridional winds by a few tens of percent is sufficient to switch the FRIS cavity circulation between bi-stable "warm" and "cold' states, accompanied by an order of magnitude change in the glacier's melt rate. These findings imply that Antarctica's major ice shelves may experience rapid changes in melt if certain climatic thresholds are exceeded, and that such changes would strongly inhibit a return to present-day melt rates. Alternatively, existing cold, dense water masses within the cavities might buffer against future intrusions of warm water and acceleration of Antarctic mass loss.

The dissertation of Julia Eileen Hazel is approved.

Andrew Thompson

Marcelo Chamecki

James C. McWilliams

Andrew Leslie Stewart, Committee Chair

University of California, Los Angeles

2019

TABLE OF CONTENTS

LIST OF TABLES

ACKNOWLEDGMENTS

The calculations of the wind stress trends were conducted using the reanalysis data provided by ERA-Interim, MERRA, CFSR, and JRA-55. I would like to thank ECMWF, NASA GISS, and NCAR for access to the available data. In addition, I would like to thank Andrew Thompson for his constructive comments on the wind stress analysis.

The Weddell Sea model incorporates SOSE, AMPS, and RTOPO data into its initial conditions and forcing. I would like to thank Matt Mazloff, the Polar Meteorology Group, and Janin Schaffer and Ralph Timmermann for access to these datasets, respectively.

Model Validation was made possible by access to Sea Surface Height, Ice Area, CTD, and seal data. I would like to acknowledge Tiago Dotto for access to the WOCE A12 and SR4 CTD data. Additionally, I want to thank Tom Armitage for access to Cryosat-2 data, the National Snow and Ice Data Center, and Tore Hatterman for access to his 17W transect upstream of the Filchner-Ronne Ice Shelf Cavity.

The work on the regional Weddell Sea model is supported by NSF award PLR-1543388.

VITA

2012–2013	Undergraduate Researcher under Professor Nicholas Cassar, Duke University. Analyzed nitrogen fixation in moss using a newly developed 'Acetylene Reduction Assays by Cavity-Laser Absorption Spectroscopy' Method
2013	B.S. (Earth and Ocean Science), Duke University.
2013–2017	Teaching Assistant, Atmospheric and Ocean Sciences Department, UCLA. Taught sections of AOS 1 (Climate Change:Puzzles and Policy), AOS 103 (Physical Oceanography) and AOS 105 (Chemical Oceanography)
2015	M.S. (Atmospheric and Ocean Science), UCLA
2016–present	Department Matlab tutor, Department of Atmospheric and Oceanic Sciences, UCLA.
2016–present	Research Assistant, Department of Atmospheric and Oceanic Sciences, UCLA.

PUBLICATIONS AND PRESENTATIONS

Are the near-Antarctic easterly winds weakening in response to enhancement of the Southern Annular Mode?, published in Journal of Climate, 2019

Role of Eddies and Tides in Water Mass Production and Ice Shelf Basal Melt in the Weddell Sea, presented at the 2018 Ocean Sciences Meeting, co-sponsored by the American Geophysical Union, 2018

Modeling Water Mass Production and Basal Melt in the Weddell Sea, Posters presented at the

American Geophysical Conference in 2016, 2018 and at the 2017 Southern Ocean Meeting at NCAR, 2017

CHAPTER 1

Motivation

1.1 Introduction

The dynamics of the Southern Hemisphere ocean currents have impacts on the global scale. The unbounded flow of the Antarctic Circumpolar Current (ACC) allows for the strongest current worldwide, transporting 130 Sv and spanning 24,000km (Whitworth III, 1983; Olbers et al., 2004). The ACC also permits a link between the Indian, Atlantic, and Pacific basins, closing the Meridional Overturning Circulation (MOC). Formation of deep water in the MOC stores dissolved CO_2, and this interaction of the ocean with atmospheric CO_2 may be an important driver of long-term climate change (Toggweiler, Russell, and Carson, 2006; Toggweiler, 2008). When bottom water is formed, the deep ocean is also ventilated with oxygen (Orsi et al., 2001).

The overturning and water mass transformation of the MOC takes place in the upper ocean in the near-Antarctic region. Here, buoyancy fluxes create a strong front enhanced by the mean (Eulerian) wind-induced Ekman transport (Döös and Webb, 1994) that serves to overturn isopycnals. The stored potential energy of the system is released as baroclinic instability in an overturning circulation as eddies attempt to restore the isopycnals to the horizontal (Marshall and Radko, 2003). The momentum balance of the near-Antarctic region is dependent on this baroclinicity. Zonal momentum is transferred through tilted isopycnals and standing/transient eddies down through the water column to the bottom of the ocean (Olbers et al., 2004). The strong eastward momentum of the ACC is thus balanced by topographic form stress (McWilliams, Holland, and Chow, 1978; Munk and Palmén, 1951).

The ACC is composed of two main fronts, the Subantarctic Front and the Polar Front, that correspond to water mass boundaries and form jets of eastward flow (Orsi, Whitworth, and Nowlin, 1995). Subantarctic Mode Water (SAMW) exists on the equatorward side of the ACC and is formed by deep winter convection (Hanawa and Talley, 2001). Antarctic Intermediate Water, identified by a salinity minimum layer that descends near the Subantarctic Front, outcrops poleward in the fresh Antarctic Surface Water. Upper Circumpolar Deep Water (UCDW) is an oxygen minimum layer sourced from low-oxygen Pacific and Indian ocean basins (Callahan, 1972). Deeper in the ocean is Lower Circumpolar Deep Water (LCDW), a salinity maximum layer that originates from North Atlantic Deep Water. Both types of Circumpolar Deep Water (CDW) spread southward and eventually outcrop at the surface south of the ACC. Finally, Antarctic Bottom Water (AABW) is formed primarily through a combination of brine rejection and heat loss (Foster and Carmack, 1976), primarily in polynyas in the Weddell and Ross Sea regions, where cyclonic gyres are the dominant patterns of flow.

The complexity of near-Antarctic circulation and its significance for global climate regulation, including ocean ventilation, highlight the importance for ongoing research efforts in this region. In addition to these motivational drivers to focus on the region, the thinning or potential collapse of ice shelves of Antarctica are crucial in the estimation of sea level rise used in future climate scenarios (Dinniman, Klinck, and Hofmann, 2012; Gille, McKee, and Martinson, 2016; Dutrieux et al., 2014; DeConto and Pollard, 2016). For example, in recent decades, the Amundsen Sea Embayment (ASE) of West Antarctica has seen an acceleration and thinning of glaciers (Turner et al., 2017) related to the inflow of warm CDW onto the shelf. This retreat of ice sheets is a potential sign, among other similar scenarios in West Antarctica, that hint at a possible future collapse of the West Antarctic Ice Sheet. Other ice shelves may also be vulnerable to similar changes in the coastal dynamics. Without thorough research into glacial dynamics and the ocean bed topography, accurate predictive modeling of glacial melt rates in future climate scenarios is unattainable. In addition, a diagnosis of ice sheet melt depends upon the knowledge of the ocean circulation patterns, stratification, and forcing trends, which are difficult to quantify given the paucity of observations.

1.2 Changes in Wind forcing and the impact on Southern Ocean Dynamics

The large-scale circulation patterns in the Southern Ocean are dependent upon the wind stress imparted by the atmosphere (Munk and Palmén, 1951). The strong westerly winds of the Southern Hemisphere (SH) mid-latitudes drive the ACC (Gnanadesikan and Hallberg, 2000). Further south, however, easterly winds force the ocean around the Antarctic coast. Though the easterlies force a much narrower band of the ocean surface than the westerlies, they are critical to the exchange of water masses across the Antarctic shelf break. In particular, they sustain the Antarctic Slope Front (ASF), across which newly-formed dense water is exported from the continental shelf (Gill, 1973; Jacobs, 1991).

The most prominent change in the near-Antarctic climate has been the southward shift of the westerly winds over the past few decades (Thompson and Solomon, 2002). This shift coincides with the trend in the positive phase of the Southern Annular Mode (SAM) (Turner et al., 2005). When the SAM is in a positive phase, a high-pressure signal exists over the SH mid-latitudes with low pressure towards the higher latitudes. A positive SAM lends to a stronger, poleward-shifting westerly wind belt (Thompson and Solomon, 2002). The shift in the SAM has spurred more research and interest into the strength and the energy of the westerly winds that drive the ACC (Meredith and Hogg, 2006; Swart and Fyfe, 2012). The recent trends in the Southern Ocean surface forcing resemble the SAM, but they are likely responses to Greenhouse Gas (GHG) and ozone emissions (Wang, Cai, and Purich, 2014). These trends are expected to result in long-term reductions in CO_2 and heat uptake in the Southern Ocean (Sallée, Speer, and Rintoul, 2010; Lenton and Matear, 2007).

A poleward shift of the westerlies may be expected to weaken the near-Antarctic easterly wind belt. However, few studies have thoroughly explored this possibility and examined to what degree the trend would impact aspects of near-Antarctic circulation.

1.2.1 Easterly Wind Stress Changes: Implications for Near-Antarctic Circulation

Previous studies detail various mechanisms by which near-Antarctic surface forcing influences the circulation. In this section, we identify four distinct processes of the circulation and their relationship to the prevailing easterly near-Antarctic winds. These processes include AABW formation, oceanic heat transport towards the Antarctic continent, sea ice formation, and broader Southern Ocean circulation.

1.2.1.1 Antarctic Bottom Water formation

Changes to the relative strength of the easterly winds have implications for the rate of AABW formation and export. AABW formation closes the MOC as it takes up CO_2 from the atmosphere and ventilates the deep ocean with oxygen (Orsi et al., 2001). Comprised of entrained Warm Deep Water, High Salinity Shelf Water (HSSW) formed in coastal polynyas, and Ice Shelf Water (ISW) from basal melting (Nicholls et al., 2009), the bulk of AABW outflow occurs as an overflow over from the Filchner Depression to the Weddell Sea through a deep channel (Foldvik et al., 2004). As the overflow enters the Weddell at the shelf break, it reaches the Antarctic Slope Front (ASF). The presence of both the ASF and the AABW outflow creates a 'V' shape density structure (Gill, 1973).

We expect that changes in the near-Antarctic easterly winds would impact the depth of the pycnocline near the Antarctic shelf, thereby altering the strength of the ASF. Wind-driven changes to the pycnocline may alter the pressure gradient between cold, dense outflow water and lighter water off the shelf (Kida, 2011). Variation in bottom water export could also occur with a changes to gyre baroclinicity as a result of changes in the cyclonic wind forcing (McKee et al., 2011). Given stronger easterly winds, we expect higher levels of dense water export with a doming of isopycnals in the center of the gyre and a deepening of isopycnals at the gyre rim (Meredith et al., 2008; Jullion et al., 2010). Thermal wind balance would necessitate that there would then be stronger velocity at depth to enhance such an export.

AABW properties and rate of export are sensitive to seasonal variations in the easterly wind stress around the Weddell Sea (*e.g.* Wang et al., 2012; Gordon et al., 2009) . The barotropic and the baroclinic components of the outflow are impacted by the strength of the winds. Both reach a maximum transport in austral fall and a minimum in austral spring, corresponding to the time when the pycnocline is at its deepest and shallowest, respectively (Su, Stewart, and Thompson, 2014).

An increase (decrease) in the easterlies around austral fall could lead to an increase (decline) in AABW export. In addition, Gordon, Huber, and Busecke (2015) provide evidence that the strength of the easterly wind stress controls AABW properties in the annual cycle. Dense water is produced on the shelf during austral winter when the easterly winds are strongest; when the winds weaken during spring and summer, this dense water shifts towards the continental slope to escape into the deep ocean (Gordon et al., 2009; Gordon, Huber, and Busecke, 2015).

1.2.1.2 Heat Transport Towards the Continental Margins

The oceanic transport of heat toward Antarctica's marine-terminating glaciers is mainly supplied by warm Circumpolar Deep Water (CDW). The transport of CDW across the continental shelves of Antarctica depends upon the strength and variability of the westward Antarctic Slope Current (ASC) (Jenkins, Hellmer, and Holland, 2001). The ASC has been shown to vary in response to changes in local wind stress (*e.g.* Stewart and Thompson, 2015a; Dinniman, Klinck, and Smith, 2011) as well as to wind changes from larger climate modes of variability (*e.g.* Nakayama et al., 2014; Spence et al., 2014). The highest thinning of glaciers at the Antarctic margins occurs where heat can access thick ice sheets via submarine troughs that cross-cut the continental shelf (Pritchard and Padman, 2012). In the Amundsen and Bellingshausen Seas, stronger westerly winds and enhanced upwelling has been shown to be the primary driver behind increased basal and surface ablation in recent decades (Holland, Jenkins, and Holland, 2010; Thoma et al., 2008).

The Amundsen Sea Low (ASL) has deepened in recent decades, which is associated with the trend toward more a positive SAM (Turner et al., 2013). The trend toward weaker austral summer/spring easterly wind stress adjacent to the Amundsen and Bellingshausen Seas may be enhancing the shoreward flux of CDW (Thoma et al., 2008). When the ASL is stronger, a westward current develops over the outer continental shelf and slope, allowing CDW to travel towards the coast along isopyncnals. This is contributing to the ongoing warming of these west Antarctic continental shelves (Schmidtko et al., 2014).

In the eastern Weddell Sea, the modeling studies of Hellmer et al. (2012) and Hellmer et al. (2017) suggest that overall strengthening of the easterlies should tend to redirect the ASC through the Filchner depression (FD), carrying more CDW beneath the Filchner-Ronne Ice Shelf (FRIS). In contrast, a *weakening* of the easterlies in the western Ross and Weddell Seas could also be expected to enhance shoreward CDW transport by raising the pycnocline at the shelf break. (Thompson et al., 2014; Stewart and Thompson, 2015a). Offshore of the Fimbul Ice Shelf, two wind-influenced mechanisms of shoreward heat transport have been identified that are tied to the easterly wind stress: Ekman transport of relatively warm summer surface water (Zhou et al., 2014), and deep intrusion of CDW (Nøst et al., 2011; Hattermann et al., 2014). If the easterlies were to decrease in strength, this effect may be expected to enhance the intrusion of CDW (Nøst et al., 2011) and suppress the shoreward transport of warm surface water (Zhou et al., 2014), leading to reduced melting at the close to the ice shelf face and enhanced melting close to the grounding line (Hattermann et al., 2014).

1.2.1.3 Sea Ice Formation

Near-Antarctic sea ice is strongly coupled to atmosphere-ocean processes that occur in the Southern Ocean. Sea ice around Antarctica has a prominent seasonal cycle (Gordon and Taylor, 1975) with significant consequences for ocean-atmosphere heat exchange. The seasonal cycle of growth and retreat controls albedo and radiative uptake (*e.g.* Ebert and Curry, 1993); sea ice insulates the ocean from fluxes of heat and momentum with the overlying atmosphere (Lee et al., 2017). Seasonal changes to the southerly winds at the Antarctic coast, in particular, play a large role in controlling the rate of open-ocean polynya formation (Zhang et al., 2015; Stössel, Zhang, and Vihma, 2011). As a consequence, the wind strength impacts brine release and HSSW production, thereby controlling rates dense shelf water export (Ohshima et al., 2013).

Coastal wind stress plays a leading role in the formation and drift of Antarctic sea ice (Lee et al., 2017). Winds are the primary contributors to the ice motion trends, while sea ice concentration trends are dominated by both thermodynamic and dynamic effects (Holland and Kwok, 2012). Over West Antarctica, ice motion trends are linked to dynamic forcing of the winds, while elsewhere thermodynamic forcing by the winds is the driver of ice motion (Holland and Kwok, 2012). Various studies have also shown that sea ice trends near Antarctica are partially driven from larger climate modes of variability including ENSO and SAM (*e.g.* Matear et al., 2015; Stammerjohn et al., 2008). The projection of such climate modes onto the Southern Ocean wind field impacts wind-driven heat fluxes and ice growth near Antarctica.

1.2.1.4 Broader Southern Ocean Circulation

Changes in the wind stress close to Antarctica also have implications for the broader circulation of the Southern Ocean. A net increase in the easterly wind stress along a near-Antarctic potential vorticity (f/h) contour can decelerate the ACC via the barotropic "free mode" (Hughes, Meredith, and Heywood, 1999; Zika et al., 2013). Over the Antarctic continental slope the potential vorticity contours and bathymetric contours are approximately aligned, and our calculated wind stress trends along the 1000m depth contour may be expected to modify the ACC transport via this mechanism. Thus, even with increasingly strong westerlies over the ACC, the southern portion of the ACC may be slowed by the overall strengthening of the easterlies (Langlais, Rintoul, and Zika, 2015).

1.3 The case for Modeling Near-Antarctic Circulation at High Resolution

The importance of the easterly wind stress and its influence on near-Antarctic circulation has been outlined. High frequency processes, such as eddies and tides, are significant to volume and heat transport as well as cross-shelf exchange (Stewart and Thompson, 2013; Padman et al., 2009; Nøst et al., 2011; Stewart and Thompson, 2016). The challenge remains in properly quantifying and diagnosing these processes both in observations and in modeling efforts. In addition to the small scales of motion, the remote location of Antarctica, the strength of its coastal currents, and the expansive sea ice cover combine to enhance the difficulty of obtaining observations for model validation. In fact, many years and seasons lack data coverage across an array of Antarctic shelf regions (Schmidtko et al., 2014).

Over the last decade, numerous studies have shown the impacts of tides in cross-slope exchange at the Antarctic margins (*e.g.* Mack et al., 2017; Padman et al., 2009; Wang et al., 2013). Tidal currents around Antarctica have instantaneous speeds up to $\mathscr{O}(1\text{m/s})$ and residual Lagrangian mean flows ranging from $\mathscr{O}$(.5-1m/s) along the Antarctic margins (Padman et al., 2009). Tidal mixing has been shown to play a role in dense water export (Padman et al., 2009) and and water mass transformation along the Antarctic shelf (Wang et al., 2013) as tidal currents act to mix dense water with overlying CDW (Whitworth and Orsi, 2006). In particular, an increase in tidal amplitude during spring tide has been correlated with an increase in dense water export, primarily through diapycnal mixing in the benthic layer (Fer, Darelius, and Daae, 2016). The outflow of AABW from the continental shelf occurs in downslope gravity currents with velocity scales of $\mathscr{O}$(1m/s) (Gordon et al., 2009) Mesoscale eddies have also been demonstrated to comprise a large role in transporting CDW towards the shelf (*e.g.* Stewart and Thompson, 2013). Eddies carry CDW, the principle source of heat, along isopycnals towards the shelf, which influences AABW export (Stewart and Thompson, 2015a; Nakayama et al., 2014). The quantification of the heat flux from mesoscale eddies is necessary in order to accurately estimate basal melting around the circumpolar ice shelves (Hattermann et al., 2014; Thompson et al., 2014; St-Laurent, Klinck, and Dinniman, 2013).

As we have improved our understanding of eddies and tides around Antarctica over the past decade, climate models have likewise advanced in their simulation of dense water overflows (Legg et al., 2009). While climate models have the capacity to form open-ocean deep convection, they remain too coarse to capture the mechanisms involved in both AABW formation (Heuzé et al., 2013) and the export of dense waters along the continental slope (De Lavergne et al., 2014). Coarse resolution models fail to resolve the topography over which the gravity waves descend, causing excessive grid-scale lateral mixing (Legg et al., 2009; Snow et al., 2015). In addition, coarse resolution atmospheric components in global climate models fail to capture the local component of the katabatic winds (Bromwich and Fogt, 2004), which are key to coastal polynya formation and dense water production (Jacobs, 2004).

1.4 The Weddell Sea Regional Model

1.4.1 Significance of the Weddell Sea

The understanding of near-Antarctic circulation and the oceanic processes that govern the circulation itself is essential given the importance of Antarctica in the context of global climate regulation. This motivates the development of a fully comprehensive model of the Weddell Sea that includes the adjacent FRIS, which we describe in §3. The aim is to achieve a 'normal' year model simulation with refinement towards 1/24° ($\mathcal{O}$(1km)) resolution. The Weddell gyre is an ideal location to resolve near-Antarctic circulation processes at high resolution since as it is one of the largest sources of AABW export (Gordon, Visbeck, and Huber, 2001; Gordon, 1981). Resolving tides, eddies, and the small-scale processes that contribute to water mass transport and transformation in this region will aid in the understanding of their relative contributions to these trends and to AABW formation as a whole. AABW formation in the Weddell depends upon the interplay of several water masses, including Modified Weddell Deep Water (mWDW), HSSW, and ISW. Observations suggest that within the FRIS cavity, ISW may escape and flows northward through the FD. When ISW crosses the sill and descends the continental slope, ISW becomes a primary component in the formation of AABW (Gammelsrød et al., 1994). The core of the northward transport of ISW that crosses the Filchner sill and contributes to bottom water formation occurs on the eastern side flank of the FD (Darelius et al., 2014). Meanwhile, HSSW formed west of Berkner Island within the Ronne depression transforms into a primary component of ISW (Nicholls et al., 2009). ISW from Berkner inflow that is too dense to escape Filchner sill and flow northward instead recirculates cyclonically within the cavity, which is filled 200-300m deep with ISW. To the east of the FD, the ASF carries ESW along the coast, below which remains a layer or warmer Modified Weddell Deep Water (mWDW). Successfully modeling AABW formation requires the simulation of these water masses and processes.

1.4.2 Past Modeling Efforts in the Weddell Sea

In order to avoid repetition of previous modeling studies as well as to emphasize the need for a high-resolution model, we highlight a few relevant past modeling efforts of the Weddell Sea.

The Bremerhaven regional ice–ocean simulations (BRIOS) model is a coupled ice-ocean model that resolves the Southern Ocean south of 50° with a horizontal resolution of 1.5° and cosine scaling in the meridional direction (Beckmann, Hellmer, and Timmermann, 1999). BRIOS-1 is coupled to the base of the 10 major Antarctic ice-shelves, allowing for heat, salt, and momentum transfer across the ice-ocean boundary layer (Hellmer, 2004). Although not eddy-resolving, validation of BRIOS against observations shows that the model was able to resolve the overturning and gyre circulation of the Weddell (Beckmann, Hellmer, and Timmermann, 1999; Hellmer, 2004). Recently, experimentation with BRIOS has surrounded the fate of the FRIS in response to atmospheric forcing changes in future climate scenarios (Hellmer et al., 2017).

Another modeling effort involves the Finite Element Sea Ice Ocean Model (FESOM), a multi-resolution ocean/sea-ice/ice-shelf model that solves the equations of motion with an unstructured mesh grid (Timmermann, Wang, and Hellmer, 2012). The ice-ocean state in FESOM is coupled to an NCEP-derived atmospheric state with topographic data from Rtopo-1. With a horizontal FESOM resolution of 1.5°, the model cannot resolve submesoscale processes within the Weddell and parameterizes sub-gridscale processes with a rotated Redi/Gent-McWilliams scheme (Timmermann, Danilov, and Schröter, 2009). FESOM is capable of reproducing modern FRIS melt rates but fails to capture the temperature and salinity stratification on the shelf (Timmermann, Wang, and Hellmer, 2012).

Overall, previous modeling studies as described above and others, including those of Wang et al. (2012) and Graham et al. (2013), piece together the circulation and the hydrography of the Weddell Sea. However, an understanding of the physical mechanisms involved in the transport and transformation of the water masses within the Weddell is lacking (Dinniman et al., 2016). We aim to develop a regional model that is fully-comprehensive and includes shelf-ice, sea-ice, tides, and a fine vertical grid to resolve the ice shelf cavity stratification. In addition, the model will be refined to eventually reach a high resolution to understand the relative roles of eddies, tides, and the broader circulation in the transport of water masses across the continental slope, cross-shelf water mass exchange, and in deep water formation.

CHAPTER 2

Are the near-Antarctic easterly winds weakening in response to enhancement of the Southern Annular Mode?

2.1 Motivation for Analysis of the Easterly Wind Stress Trend

This chapter has been adapted from the article published in Journal of Climate (Hazel and Stewart, 2019). The motivation for diagnosing the trend in the easterly wind stress has been detailed in §1.2. The easterlies have substantial impacts on near-Antarctic circulation, including AABW formation, sea ice drift, and heat transport towards the ice shelves. While the majority of Southern Ocean research has focused on the impact of the southward-intensifying shifting westerlies on the ACC, few studies have attempted to quantify the trend in the easterly wind stress and its potential significance on regional ocean dynamics. Spence et al. (2014) prescribed an experimental weakening of the easterly wind stress and found that this weakening influences bottom water formation through a reduction of cold surface shoreward Ekman water transport. Stewart and Thompson (2015a) and Stewart and Thompson (2013) also demonstrate that the Circumpolar Deep Water (CDW) intrusion to the ASF and the Meridional Overturning Circulation (MOC) will shift with changes to the easterly wind stress. The studies outlined are just a few of the several done that have prescribed wind stress perturbations on the near-Antarctic system *e.g.* Zhou et al., 2014; Dinniman, Klinck, and Smith, 2011; Thoma et al., 2008.

The large scale circulation in the Southern Ocean is dependent upon the wind stress imparted by the atmosphere (Munk and Palmén, 1951). The strong westerly winds of the Southern Hemisphere (SH) mid-latitudes drive the Antarctic Circumpolar Current ACC, Gnanadesikan and Hallberg, 2000, a strong, unbounded flow that connects the major ocean basins and permits a global overturning circulation (Rintoul, 2010). Further south, easterly winds force the ocean around the Antarctic coast. Though the easterlies force a much narrower band of the ocean surface than the westerlies, they remain critical to the exchange of water masses across the Antarctic shelf break. In particular, they sustain the Antarctic Slope Front (ASF), across which newly-formed dense water is exported from the continental shelf (Gill, 1973; Jacobs, 1991). Fig. 2.1(a-b) shows the multi-decadal mean surface wind stress over the Southern Ocean, and Fig. 2.1(c) contrasts the mid-latitude westerlies with the band of easterlies around the Antarctic margins. Though for convenience we refer to the latter as “easterly winds", it is more accurate to describe their direction as “anticyclonic" because they tend to be oriented parallel to the coastline rather than strictly easterly. The easterlies are supported by a combination of geostrophic flow associated with the pressure gradient between the high-altitude continental interior and the low-pressure coastal trough, and Coriolis deflection of offshore katabatic winds toward the west (Parish and Bromwich, 1997). As a result, the shape of the continent obscures this band in a zonal average, so in Fig. 2.1(d-e) we plot the more dynamically relevant, alongshore component of the wind stress (see §2.2 for details). Here the mean alongshore wind stress is easterly except at the Antarctic Peninsula, which protrudes into the ACC.

Table 2.1: Definitions of labeled reference points along the Antarctic coast

Acronym	Location
F	Filchner Ice Shelf
AIS	Amery Ice Shelf
T	Totten Glacier
R	Ross Sea
A	Amundsen Sea
AP	Antarctic Peninsula
W	Weddell Sea

The most prominent change in the near-Antarctic climate has been the enhancement of the westerly winds over the past few decades (Thompson and Solomon, 2002). This shift coincides with the trend towards the high-index polarity of the Southern Annular Mode (SAM) (Marshall,

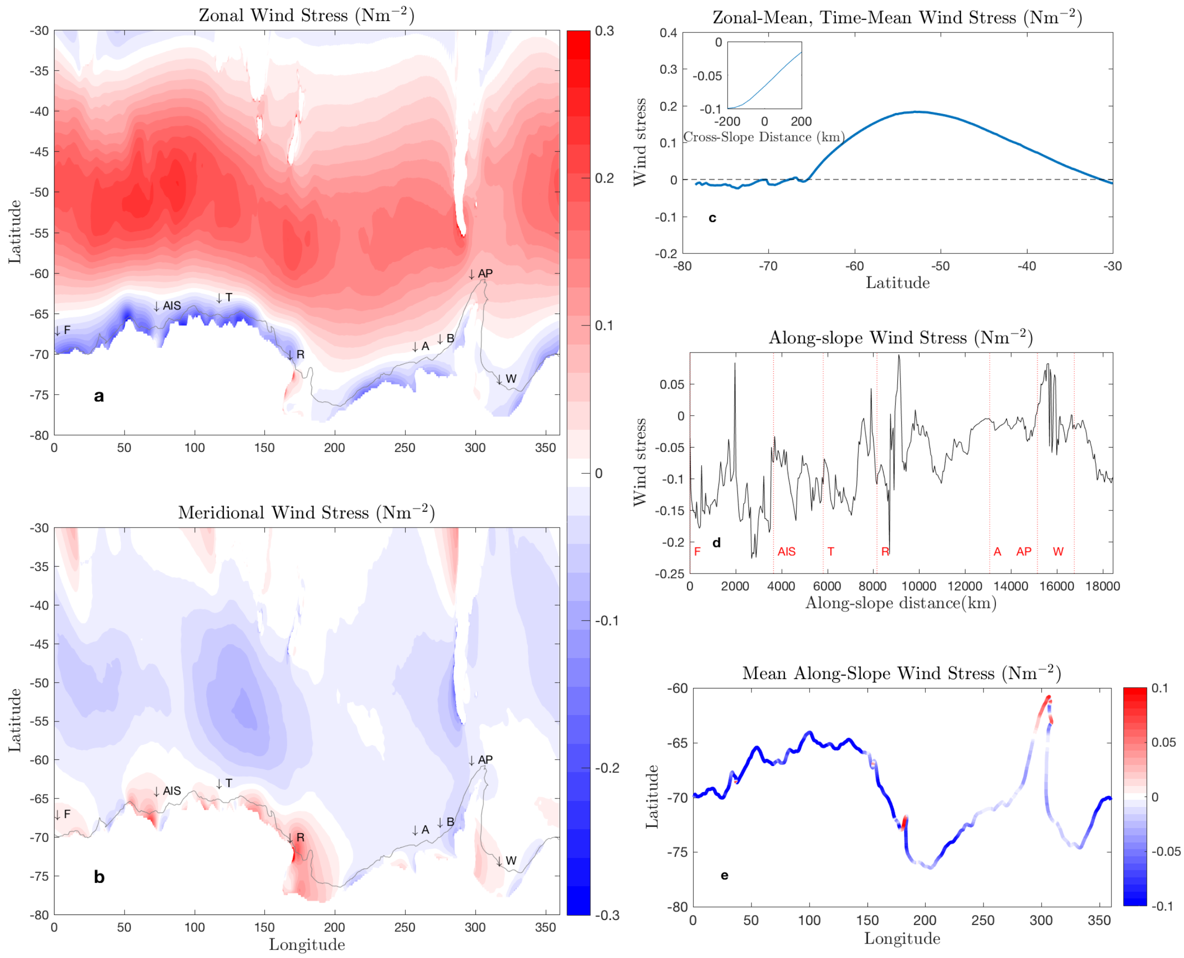

Figure 2.1: Multi-decadal mean surface wind forcing around the Antarctic margins from 1979–2014 ERA-Interim reanalysis data (Dee et al., 2011). (a) Mean zonal wind stress (N/m^2), (b) mean meridional wind stress (N/m^2), (c) zonal- and time-mean wind stress (N/m^2), (d) mean along-slope wind stress (N/m^2) as a function of along-slope distance and (e) mean along-slope wind stress (N/m^2) projected onto the circum-Antarctic 1000m depth contour. The inset in panel (c) shows an alternative wind stress profile obtained by averaging in time and along the coast. Labels in panels (a) and (b) indicate reference points to aid interpretation of panel (d). See Table 2.1 for further details.

2003; Turner et al., 2005). When the SAM is in this positive phase, a high pressure signal exists over the SH mid-latitudes with low pressure towards the higher latitudes. A positive SAM induces a stronger, poleward-shifted westerly wind belt (Thompson and Solomon, 2002). The trend in the SAM has spurred more research and interest into the changes in the strength of the westerly winds and their impact on the ocean circulation (Meredith and Hogg, 2006; Swart and Fyfe, 2012; Hogg et al., 2015; Bracegirdle, 2013). This trend is likely a response to both Greenhouse Gas (GHG) and ozone emissions (Wang, Cai, and Purich, 2014), and is expected to result in long-term reductions in CO_2 and heat uptake in the Southern Ocean (Sallée, Speer, and Rintoul, 2010; Lenton and Matear, 2007). The first EOF of the SAM projects onto the Antarctic coastline, so enhancement of the SAM may be expected to decrease the strength of the near-Antarctic easterlies *e.g.* Langlais, Rintoul, and Zika, 2015.

The easterly winds play a central role in modulating exchanges across the Antarctic shelf break. The oceanic transport of heat toward Antarctica's marine-terminating glaciers and ice shelves is supplied by warm, salty Circumpolar Deep Water (CDW) (Jenkins et al., 2016; Heywood et al., 2016). Spence et al. (2014) use a $\frac{1}{4}^{\circ}$ ocean/sea ice model to show that a reduction of Ekman pumping occurs due to weakened easterly winds and strengthened, southward-shifting westerly winds. This leads to CDW intrusion and rapid heating of ice shelf waters. However, this mechanism may be less efficient where the Antarctic Slope Current (ASC) experiences strong tidal forcing (Flexas et al., 2015; Stewart, Klocker, and Menemenlis, 2018). A weakening of the easterlies in the western Ross and Weddell Seas could also be expected to enhance shoreward CDW transport by raising the pycnocline at the shelf break. (Thompson et al., 2014; Stewart and Thompson, 2015a).

Trends in the near-Antarctic easterly wind stress have impacts beyond their influence on the Antarctic coast. For example: (i) A reduction or a shift in the easterly wind stress around the continent may directly modify the rate of Antarctic Bottom Water (AABW) export across the continental slope (Stewart and Thompson, 2012; Stewart and Thompson, 2013). Globally, AABW has been warming, freshening and thinning over the past few decades (Purkey and Johnson, 2010; Jullion et al., 2013; Meijers et al., 2016), though the cause remains unclear. The export of AABW from the Weddell Gyre is also mediated by the changes in the winds around the Antarctic margins (Jullion et al., 2010). (ii) Changes in the easterly winds have the potential to alter the strength of the southern branch of the ACC via the 'free mode' mechanism, in which the depth-averaged velocity of the ACC is accelerated by the near-Antarctic wind stress along a circum-Antarctic f/h contour (Hughes, Meredith, and Heywood, 1999; Zika et al., 2013). (iii) The coastal winds play a leading role in ice formation and export (Holland and Kwok, 2012; Kwok, Pang, and Kacimi, 2017; Haumann et al., 2016).

In addition to changes associated with the enhancement of the westerly wind belt, the easterlies are influenced by changes in the Antarctic katabatic winds. The pole-to-coast downslope pressure gradient drives these winds down the sloping continent toward the coast, where they turn westward under the influence of the Coriolis force (Parish and Waight III, 1987). A large-scale low atmospheric pressure system over the Antarctic Coast enhances katabatic winds (Parish, Pettré, and Wendler, 1993; Parish and Bromwich, 2007), which may in turn be expected to enhance alongshore winds.

In this article we quantify the trends in the easterly surface forcing around Antarctica over the past several decades to examine their response to the enhancement of the SAM. In §2.2, we describe our data sources and methods used to calculate the wind stress trends, the trends in the SAM, and the strength of the katabatic winds. In §2.3 we show that the air-sea momentum exchange in the easterly wind band has remained approximately unchanged, but that there has been a substantial change in the seasonal cycle of the alongshore wind forcing. We further perform a comparison of these results against other observationally-validated reanalysis products. In §2.4 we summarize our findings and discuss the potential implications of the diagnosed trends, and in §2.5 we provide concluding remarks and discuss the outlook for further research.

2.2 Data and Methods

2.2.1 Data

We use the wind stress reported by reanalysis datasets for our calculations because insufficient direct observations are available to calculate the trends. Our primary dataset is ERA-Interim (Dee et al., 2011), which we use to calculate the trend in the easterly wind stress from the monthly mean surface fluxes. We compare ERA-Interim with the Japanese 55-year Reanalysis (JRA-55) (Kobayashi et al., 2015), the NCEP Climate Forecast System Reanalysis (CFSR) (Saha et al., 2010), and the NASA Modern Era Retrospective-Analysis for Research and Applications Version 2 (MERRA2) (Gelaro et al., 2017). All of these products provide data over multiple decades and compare favorably with available observations (Bracegirdle and Marshall, 2012). We focus on the surface easterly wind stress instead of wind velocity because wind stress more directly quantifies atmosphere-ocean momentum transfer and is thus more relevant to the wind-driven ocean circulation around the Antarctic margins. Note, however, that we are unable to distinguish between stress applied to the surface of the ocean and stress applied to the sea ice. While wind momentum imparted to sea ice may be transferred through to the ocean, densely packed sea ice that is immediately adjacent to land can also transfer momentum to the continent via internal stress (Leppäranta, 2011).

The wind stress in ERA-Interim is calculated using the ECMWF bulk parameterization scheme (Renfrew et al., 2002). The ERA-Interim surface stress data has a spatial resolution of .75° x .75° and spans the years 1979–2014 (Dee et al., 2011). The sea ice, essential for proper flux measurements, is estimated by using the daily output from NCEP and the new global, operational, high-resolution, combined sea surface temperature (SST) and sea ice analysis system (OSTIA) (Stark et al., 2007). In comparison with *in situ* measurements, ERA-Interim exhibits correlations in MSLP of greater than .98 and correlations between annual mean surface temperatures of .88. ERA-Interim is the most accurate reanalysis dataset in its quantification of mean sea level pressure (MSLP) and geopotential height over Antarctica in the past three decades (1979–2008), with substantially smaller decadal-mean biases than other reanalysis products (Bracegirdle and Marshall, 2012). ERA-Interim also most accurately reproduces the geostrophic winds around the Amundsen Sea compared to 6 other reanalysis products (Bracegirdle, 2013).

For validation purposes, we calculate the easterly wind stress trend in MERRA, CFSR, and JRA-55. All of the reanalysis products considered here use similar bulk parameterization schemes to assimilate wind speed observations. All products use a 3D variational assimilation method to compute air-sea fluxes from 6-hourly integrated fluxes that are based on roughness length parameterizations (Smith, Hughes, and Bourassa, 2011). The drag coefficients are derived from a modified

Charnock formula and empirical stability functions. JRA calculates the drag coefficient in a similar manner but does not include a stability term into the calculation of the Monin-Obukhov length scale. The 10m wind speed is used to calculate the wind stress values, so there are strong qualitative similarities between the calculated wind stress trends reported in §2.3 and the 10m wind speed trends, as discussed in §2.6. In the Appendix in §2.6, we reproduce a subset of our wind stress trend calculations using an independent estimate of the stresses derived from the 10m wind speeds via a simple quadratic bulk formula. These calculations demonstrate that the diagnosed trends are primarily due to changes in the winds, rather than, for example, changes in surface roughness due to changes in sea ice concentration.

Global reanalysis products remain at resolutions too coarse to resolve coastal features, and orography height biases contribute to errors in model temperature (Bracegirdle and Marshall, 2012; Bromwich and Fogt, 2004). Therefore, we additionally compare ERA-Interim with the Antarctic Mesoscale Prediction System Powers et al., 2003a; Powers et al., 2012, henceforth AMPS, which spans 2006—2015. AMPS does not provide surface stresses, so instead we compare the 10m velocity fields (see §2.6 Fig. 2.13). AMPS employs higher spatial resolution and is able to resolve a consistently swifter band of easterly winds around the Antarctic coast. Our comparison (see §2.6) shows that the enhancement of the alongshore winds in AMPS, relative to ERA-Interim, is typically higher than the diagnosed trends in the 30-year ERA-Interim data. This is a caveat to the present study: it is likely that the magnitudes of the ERA-Interim trends reported in this study would change with a higher spatial resolution.

2.2.2 Methods

2.2.2.1 Wind Stress Trends

We calculate the annual and seasonal linear trends in the zonal and meridional components of the wind stress over the 36-year 1979–2014 ERA-Interim reanalysis timespan as well as the 1973–2012 JRA-55 (40 years), 1979–2015 MERRA (36 years), and 1980–2010 CFSR (31 years) datasets, respectively. Due to the variable latitudinal extent of the Antarctic coastline, neither the zonal nor the meridional components of the wind stress products provide a robust measure of the alongshore wind stress, which is arguably the most relevant for near-Antarctic circulation because it sets the cross-slope Ekman transport (Nøst et al., 2011; Stewart and Thompson, 2015b; Zhou et al., 2014). We therefore additionally quantify the mean and trend of the wind stress directed along the Antarctic continental shelf break, which we define as the circum-Antarctic 1000m depth contour, taken from ETOPO-1 (Amante and Eakins, 2009). We emphasize the component of the wind stress parallel to the Antarctic coast, as this component directly influences water mass exchanges across the continental slope e.g. Thompson et al., 2014; Stewart and Thompson, 2016. This also motivates our use of the 1000m depth contour to define the Antarctic "coastline", as this consistently tracks the location of the continental shelf break.

To facilitate calculation of the along-slope winds, we derive a high-resolution 1000m depth contour to represent the coastline from the ETOPO-1 bathymetric dataset (Amante and Eakins, 2009). For compatibility with the spatial resolution of the ERA-Interim wind stress data, we approximated this contour as a series of piecewise-linear (in latitude/longitude space) sections of 1° in length. We then interpolated and rotated the wind stress data in order to calculate the wind stress directed along each section. To compensate for our somewhat arbitrary selection of the 1000m depth contour to define the coastline, we calculated the wind stress along each section as an average over a box that spans the length of the section and a prescribed width perpendicular to the section. More precisely, along each section we define a coordinate system (s,n), in which the s and n coordinates lie parallel and perpendicular to the section, respectively. We define a grid of points (s_i,n_j), with $i = 1,\ldots,M$ and $j = 1,\ldots,N$, that spans the length L of the section and a width W perpendicular to the section. We then interpolate and rotate the wind stress to each point on this $M \times N$ grid. To create the plots in our manuscript, we used a grid of $M = 10$ by $N = 11$ points and averaged over the entire grid to calculate a single alongshore wind stress value for each section. Using finer discretizations (higher M and/or N) did not change the calculated along-slope wind stress. We use a box width $W = 100\,\text{km}$ that is comparable to the width of the Antarctic continental slope (Amblas and Dowdeswell, 2018). The exception is the inset in Fig. 2.1(c), for which we used a box width of $W = 400\,\text{km}$ and averaged in the s-direction over all sections, in order to create an extended cross-slope profile of along-slope wind stress for comparison with the zonal-mean wind stress.

2.2.2.2 Interannual Variability in the SAM and the Pole-to-Coast Pressure Gradient

Motivated by the impact of the SAM on the southward-shifting westerly winds and the hypothesized influence on the near-shore easterly wind stress, we calculate the correlations between the calculated interannual easterly wind stress trends and the calculated interannual ΔP_{SAM}. We develop the ΔP_{SAM} calculation based on the difference in the zonal MSLP between 40°–65°S. We use the method described by (Marshall, 2003) to calculate this difference by linearly interpolating the MSLP from the reanalysis products (to the nearest .1°) to six observational stations at 40°S and six at 65°S. These stations are listed in Table 2.2. In the interest of achieving a self-contained presentation, we use the mean of the six differences between the interpolated values at 40°S and 65°S to calculate ΔP_{SAM}.

Station Name	Latitude°S	Longitude °E
Marion Island	46.9	37.9
Ile Nouvelle Amsterdam	37.8	77.5
Hobart	42.9	147.3
Christchurch	43.5	172.6
Valdivia	39.6	-73.1
Gough Island	40.4	-9.9
Novolazarevska	70.8	11.8
Mawson	67.6	62.9
Mirny	66.6	93.0
Casey	66.3	110.5
Dumont D'Urville	66.7	140.0
Faraday/Vernadsky	65.2	-64.3

Table 2.2: Meteorological station locations used to calculate ΔP_{SAM}

Anticipating that the easterlies should also vary in response to the pole-to-coast pressure gradient that drives the katabatic winds, we define ΔP_{Kat}, an analogue of ΔP_{SAM}, to capture changes in this gradient. ΔP_{Kat} is defined as the magnitude of the zonal MSLP between 85°S and 65°S. In contrast to ΔP_{SAM}, this pressure difference is calculated using straightforward averages of the pressure around latitude circles. We find the MSLP at 85°S and 65°S and subtract the difference to find ΔP_{Kat}. We note that ERA-interim uses a bias-correction scheme to eliminate inconsistencies in the SLP measurements (Dee et al., 2011) that may exclude measurements of surface pressure on elevated terrain. However, its accuracy in reproducing pressure and temperature measurements close to the pole remains comparable to that close to the coast (Bracegirdle and Marshall, 2012).

2.3 Circum-Antarctic wind stress trends

2.3.1 Annual-mean wind stress trend

Fig. 2.2(a-b) shows the overall zonal and meridional wind stress trends calculated from ERA-Interim data. The most prominent feature of this trend is an enhanced eastward stress due to the strengthening of westerly winds, primarily between 45°S and 60°S. This eastward strengthening approaches $0.05\,\mathrm{N\,m^{-2}}$ in the Pacific sector and bears a pattern that qualitatively resembles the first principal component of the SAM (*e.g.* Langlais, Rintoul, and Zika, 2015). However, this eastward stress trend does not extend to the Antarctic coastline. With the exceptions of the western Ross Sea and the tip of the Antarctic peninsula, the trend shows an enhanced westward wind stress along the coast. There are also substantial regional variations in the amplitude of this strengthening trend, with the area around the Amery ice shelf exhibiting a particularly pronounced intensification of the westward stress over this time period.

Panels (c) and (d) of Fig. 2.2 show the trend in the alongshore wind stress (defined positive for a “westerly" or cyclonic trend) as a function of alongshore distance and mapped onto the 1000m depth contour, respectively. This trend further suggests that the annual-mean easterly wind stress around the Antarctic coast is strengthening, albeit weakly, which is contrary to the expected weakening associated with the SAM. Averaged around the coastline the easterly wind stress increased in magnitude by $.0044\,\mathrm{N\,m^{-2}}$ from 1979 to 2014. Note, however, that this strengthening is not statistically significant at the 5% level ($p = .25$, see table 2.4). The exceptions to this easterly trend are found in the northwestern Ross and northwestern Weddell Seas. This is largely due to a northerly meridional wind stress trend in these regions which acts to reduce the strength of the katabatics that drive the easterlies.

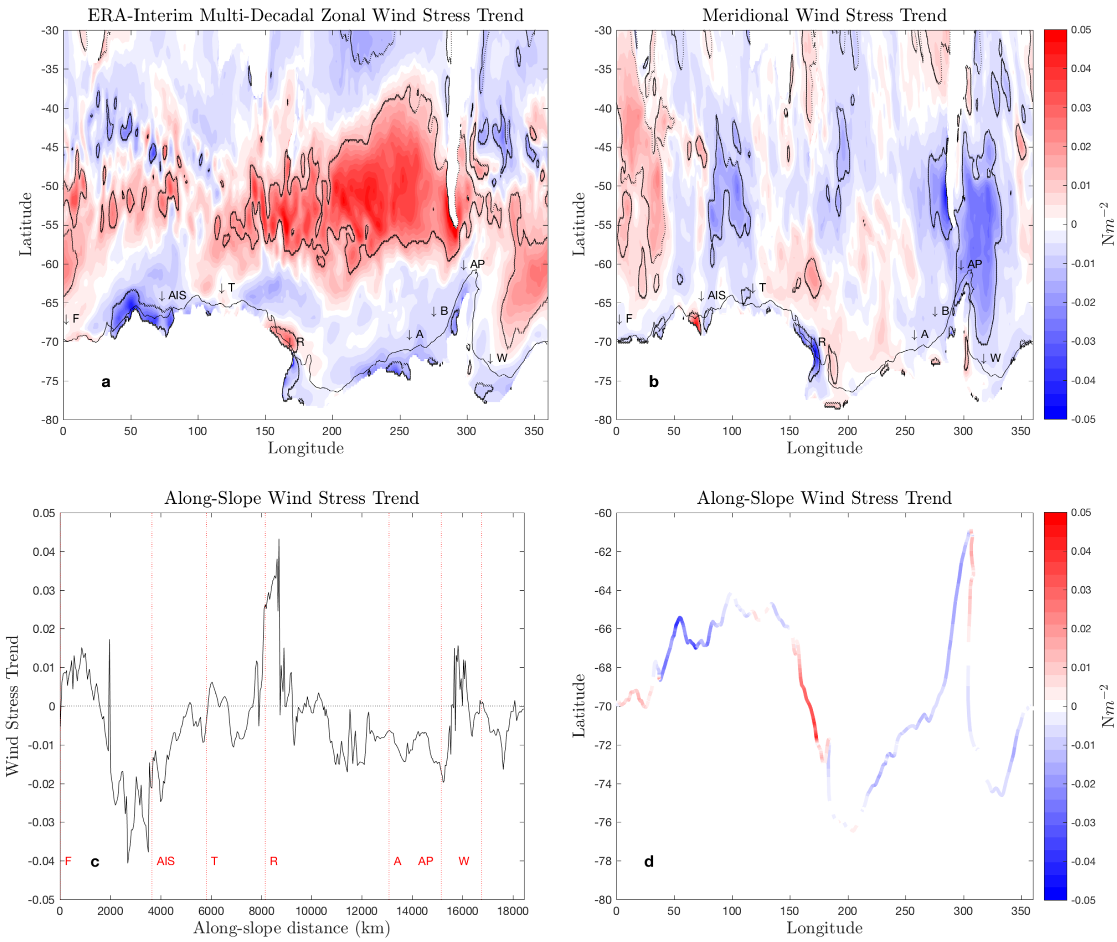

Figure 2.2: Multi-decadal trends in the mean surface wind stress (N/m^2) around the Antarctic margins, from 1979–2014 ERA-Interim reanalysis data (Dee et al., 2011). Black contours envelop regions that are statistically significant at the 5% level. (a) Mean zonal wind stress trend (N/m^2), (b) mean meridional wind stress trend (N/m^2), (c,d) along-slope wind stress trend as a function of along slope distance and mapped onto the 1000m depth contour.

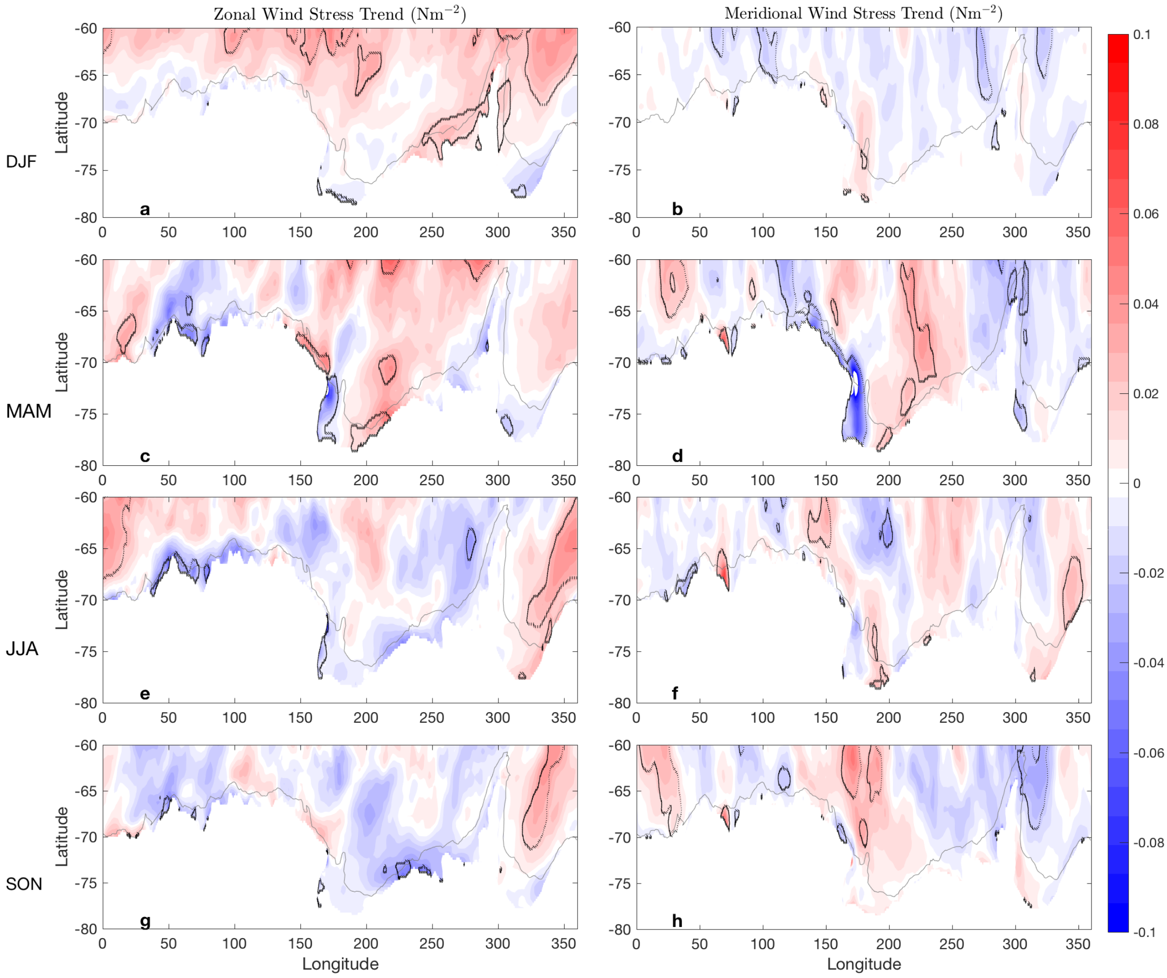

Figure 2.3: Multi-decadal trends in the seasonal-mean zonal and meridional wind stress (in N/m^2), calculated from 1979–2014 ERA-Interim reanalysis data (Dee et al., 2011). Black contours envelop trends that are statistically significant at the 10% level. (a) DJF zonal wind stress trend, (b) DJF meridional wind stress trend, (c) MAM zonal wind stress trend, (d) MAM meridional wind stress trend, (e) JJA zonal wind stress trend, (f) JJA meridional wind stress trend, (g) SON zonal wind stress trend, and (h) SON meridional wind stress trend.

2.3.2 Trend in the seasonal cycle

The pronounced seasonal cycle around Antarctica (Meehl, 1991; Simmonds and Jones, 1998; Mathiot et al., 2011; Wang et al., 2012; Gordon, 1981) warrants a calculation of the trends in

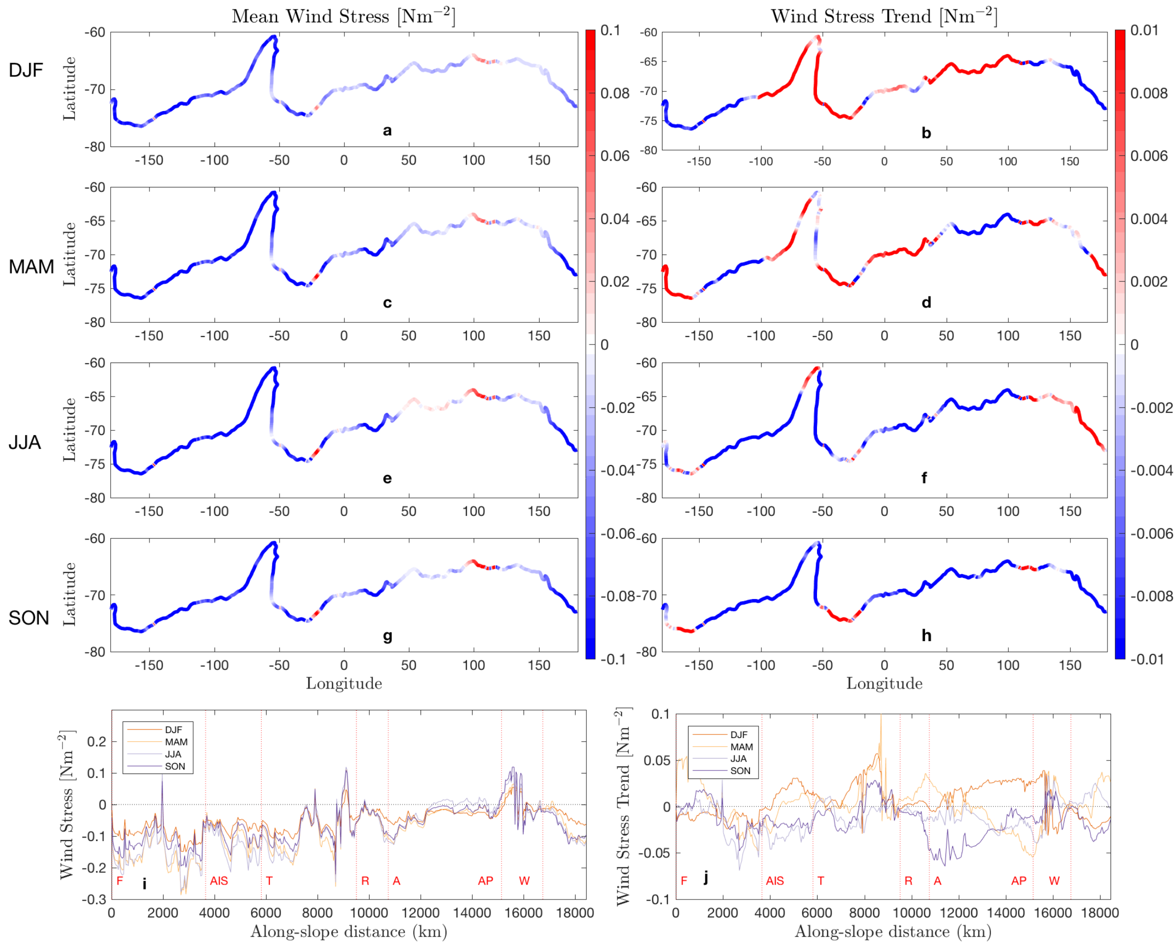

Figure 2.4: Multi-decadal mean and trend of the seasonal-mean along-slope wind stress N/m^2, from 1979–2014 ERA-Interim reanalysis data (Dee et al., 2011). (a) DJF mean, (b) DJF trend, (c) MAM mean, (d) MAM trend, JJA mean (e), JJA trend (f), SON mean (g) and (h) SON trend. (i,j) Compilation of the mean and trend of along-slope wind stress, respectively, as functions of along-slope distance.

the seasonally-averaged wind stress. Figs. 2.3 and 2.4 show the seasonal breakdown of the zonal/meridional and alongshore wind stress trends. There are pronounced local variations in the signs and amplitudes of the alongshore trends in Fig. 2.3. For example, in Fig. 2.2 we find a weakening of the easterlies in the western Ross Sea and the western Weddell Sea. Fig. 2.3(a,c) shows that the weakening is statistically significant in DJF in the western Weddell Sea and in DJF and MAM in the Ross Sea. Austral summer and autumn also have significant northerly strengthening trends in these regions, which will augment the trend of weakening circumpolar-averaged anti-cyclonic wind stress. In contrast, parts of East Antarctica show a strengthening of the prevailing easterly wind stress trend in all seasons, with this trend being significant in all seasons at the 5% level with the exception of DJF.

Figs. 2.3 and 2.4 both visually suggest an overall pattern of austral summer weakening and austral winter strengthening of the prevailing easterly winds. More quantitatively, from 1979 to 2014, DJF and MAM exhibit weakening trends of magnitudes of $.0055\,\mathrm{N\,m^{-2}}$ ($p = .26$) and $.0022\,\mathrm{N\,m^{-2}}$ ($p = .76$), respectively. The SAM has been shown to be most positive in DJF and MAM (Marshall, 2003), consistent with the widespread enhancement of the westerly wind stress visible in Fig. 2.3(a,c). This westerly anomaly is compensated in JJA and SON by strengthening of the prevailing easterly wind stress trends of $.0112\,\mathrm{N\,m^{-2}}$ ($p = .17$) and $.0143\,\mathrm{N\,m^{-2}}$ ($p = .03$), respectively. Fig. 2.3(e,g) shows widespread easterly wind stress anomalies, particularly close to the Antarctic coast. In various locations these easterly trends are accompanied by strong southerly wind stress anomalies within a few latitudinal degrees of the coast, visible in Fig. 2.4(f,h), suggesting that trend toward stronger winter easterlies may be associated with stronger katabatic winds.

In summary, the annual-mean circumpolar alongshore wind stress trends are small but indicate a slight strengthening of the easterlies, in contrast to the expected weakening due to enhancement of the SAM. However, the trends are regionally and seasonally much larger, notably in DJF and SON in the Amundsen and East Antarctic sectors. At the continental scale this implies a trend toward a larger seasonal cycle (see Fig. 2.4(j)), with a weakening of the alongshore easterlies in summer and a strengthening in winter. We discuss implications of this trend in §2.4.

2.3.3 Attribution of the Circum-Antarctic Wind Stress Trends

The trends in the circumpolar wind stress in ERA-Interim show a weakening during austral summer and autumn and a strengthening during austral winter and spring. As stated previously, the high-index polarity of the SAM is characterized by lower pressure at mid-latitudes with higher pressures and cold temperatures over the Antarctic continent (Thompson and Solomon, 2002; Shindell and

Schmidt, 2004). Periods of anomalously cold temperatures are also associated with slope-inversion pressure gradients in interior East Antarctica (Kodama and Wendler, 1986). We now examine both multidecadal variations in the SAM (ΔP_{SAM}) and in the pole-to-coast pressure gradient (ΔP_{Kat}) to determine the extent to which the coastal wind trends can be related to these indicators of Southern Hemisphere climate variability.

Fig. 2.5 shows the seasonal trend in the ERA-Interim ΔP_{SAM}, ΔP_{Kat} and the circumpolar easterly wind stress trend with the corresponding Pearson's correlation coefficients (r). Fig. 2.5(a,b) shows that the increase in ΔP_{SAM} is largest during DJF and MAM and is accompanied by a weakening of the easterly wind stress, particularly in DJF. In contrast, SON shows a weakened ΔP_{SAM} and a strengthened easterly wind stress accompanied by a strengthening of ΔP_{Kat}. All seasons demonstrate a positively correlated circumpolar-averaged westerly wind stress with ΔP_{SAM} (equivalent to a negative correlation between circumpolar-averaged easterly wind stress with ΔP_{SAM}) and a negatively correlated circumpolar-averaged westerly wind stress and ΔP_{Kat} (equivalent to a positive correlation between circumpolar-averaged easterly wind stress and ΔP_{Kat}). The interannual correlations between ΔP_{Kat} and the easterly wind stress are consistently stronger. Thus positive ΔP_{SAM} and ΔP_{Kat} periods are typically accompanied by weakening and strengthening of the easterly wind stress, respectively.

To attribute the long-term seasonal trends in the alongshore wind stress, we now consider seasonal trends in ΔP_{Kat} and ΔP_{SAM}. We list the seasonal ΔP_{Kat}, ΔP_{SAM} trends and the seasonal wind stress trends in Table 2.3 with their corresponding p-values. The trend in ΔP_{SAM} is positive in all seasons except for SON. In DJF, ΔP_{SAM} has its greatest trend of 12.74 hPa Century^{-1}, with a significance of 1%. However, DJF is the only season where ΔP_{SAM} is significant at less than 10%. In terms of ΔP_{Kat}, we see positive trends in JJA and SON, but these trends lack significance. This supports the hypothesis that multi-decadal weakening of the easterlies in DJF is associated with the increase in ΔP_{SAM}. In SON, although ΔP_{SAM} has decreased, its trend is not statistically significant and so does not explain the intensification of the easterlies. In contrast ΔP_{Kat} exhibits its strongest trend in SON, strengthening by 4.04 hPa Century^{-1}. This trend is marginally insignificant at the 10% level ($p = 0.11$), despite the strong interannual correlation $r = -.74$, due to the large amplitude of the interannual fluctuations in ΔP_{Kat}. Thus, while the trends suggest a relationship

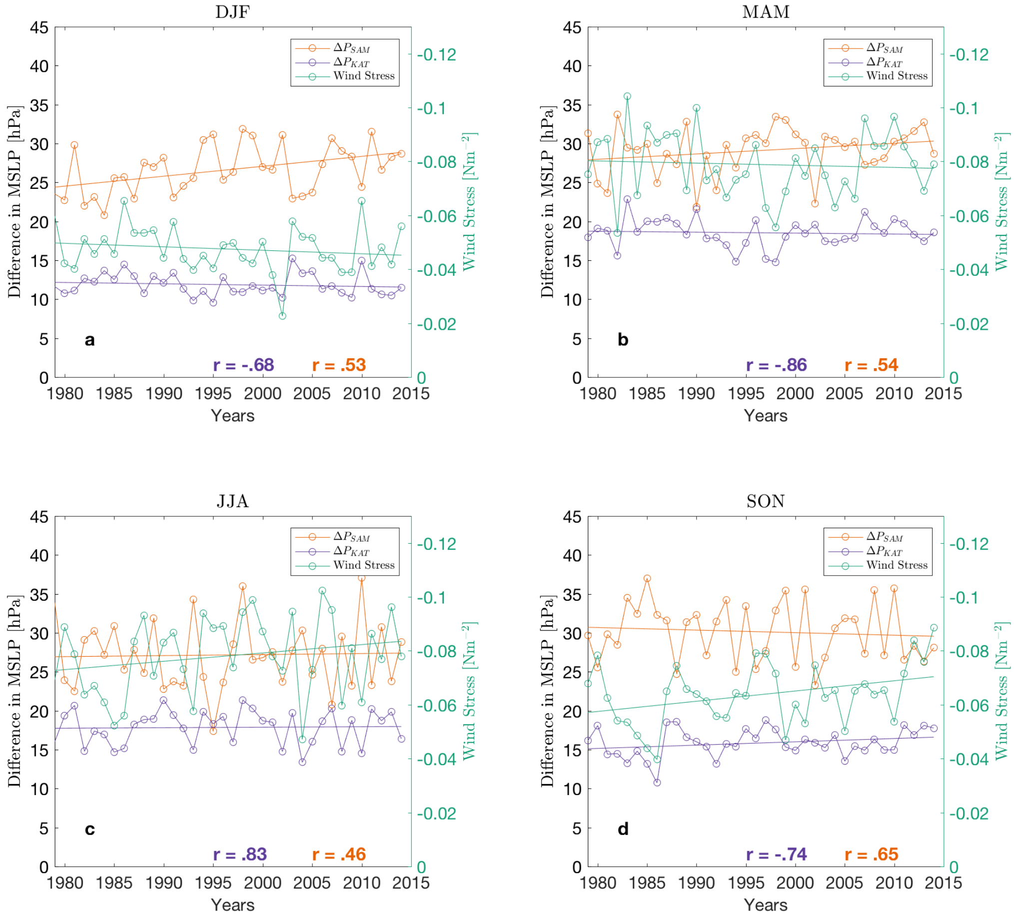

Figure 2.5: The seasonal breakdown (a) DJF, (b) MAM, (c) JJA, (d) SON of the multi-decadal trend in the ΔP_{SAM} and ΔP_{Kat} from 1979–2014 ERA-Interim reanalysis data (Dee et al., 2011). We calculate ΔP_{SAM} (orange) as the difference in the MSLP from six observational stations at 40°S and 65°S that are interpolated to the nearest .1°. We calculate ΔP_{Kat} (purple) as the difference in the MSLP between 85–65°S. Superimposed on ΔP_{SAM} and ΔP_{Kat} are their trends, the mean along-slope annual wind stress $\mathrm{N\,m^{-2}}$ (green), and the trend in the mean seasonal along-slope wind stress $\mathrm{N\,m^{-2}}$. The correlation between the mean seasonal ΔP_{SAM} and ΔP_{Kat} with the along-slope wind stress $\mathrm{N\,m^{-2}}$ is provided on the bottom of each plot.

between intensification of both ΔP_{Kat} and the easterlies in SON, an unambiguous attribution is not possible based on our analysis.

Trend	DJF	MAM	JJA	SON
Wind Stress Trend [N m^{-2} Century^{-1}]	.015$^{.26}$	.006$^{.76}$	-.031$^{.17}$	-.040$^{\mathbf{.03}}$
ΔP_{SAM} Trend [hPa Century^{-1}]	12.74$^{\mathbf{.01}}$	6.86$^{.19}$	1.32$^{.95}$	-3.28$^{.48}$
ΔP_{Kat} Trend [hPa Century^{-1}]	-1.68$^{.44}$	-2.05$^{.77}$	.369$^{.68}$	4.04$^{.11}$

Table 2.3: ERA-Interim seasonal trends in the circumpolar-averaged alongshore wind stress and meridional pressure gradients with the corresponding p-values as superscripts. P-values in bold are significant at 10%.

In summary, a combined consideration of interannual correlations between the large-scale pressure gradients ΔP_{SAM} and ΔP_{Kat}, combined with the linear multi-decadal trends given in Table 2.3, suggest two connections: intensification of the DJF ΔP_{SAM} with weakening of the easterlies, and intensification of the SON ΔP_{Kat} with strengthening of the easterlies. However, pronounced interannual variability renders only the DJF ΔP_{SAM} trend and SON wind stress trend significant at the 10% level, so there remains some ambiguity as to the drivers of the wind stress trends. The complexity of the dynamics near Antarctica implies that our calculated trends may be influenced by other phenomena, such as the Semi-Annual Oscillation (SAO), related to semi-annual expansion and contraction of cyclonic activity in the mid and high-Southern Hemisphere latitudes (Meehl, 1991; Simmonds and Jones, 1998).

2.3.4 Consistency Among Reanalysis Products

As outlined in §2.2.1, ERA-Interim is used to quantify the trend in the multi-decadal easterly wind stress and provides the closest comparison to Antarctic meteorological stations (Bracegirdle and Marshall, 2012). However, as stated previously, reanalysis data is less constrained by observations in high latitudes than in other parts of the world (Dee et al., 2011). Therefore, we check the

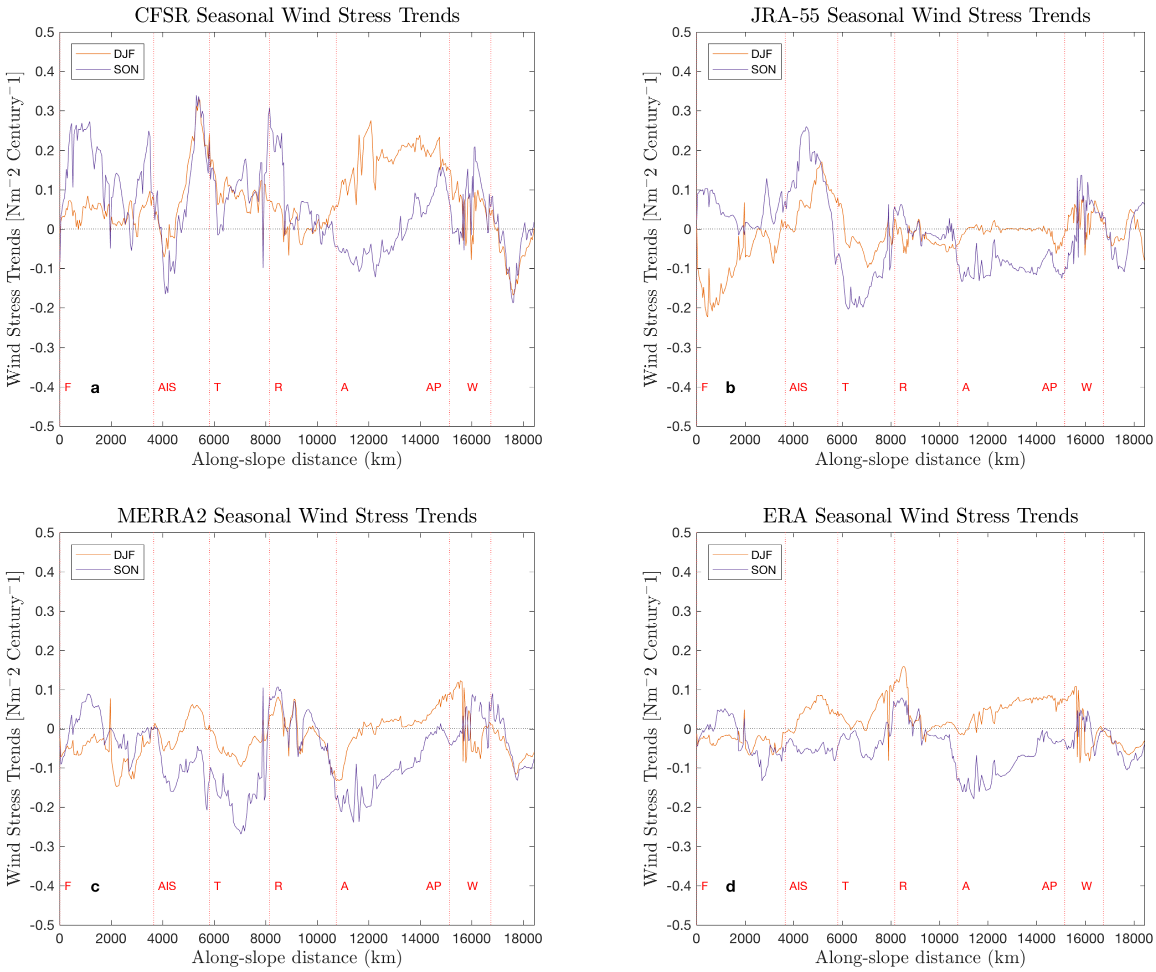

Figure 2.6: Multi-decadal DJF and SON along-slope circumpolar wind stress [$\mathrm{N\,m^{-2}\,Century^{-1}}$] trends from (a) 1980-2010 CFSR (Saha et al., 2010), (b) 1972-2013 JRA-55 (Kobayashi et al., 2015), (c) 1980-2015 MERRA2 (Gelaro et al., 2017) data, and (d) 1979-2014 ERA (Dee et al., 2011) reanalysis products. Red labels indicate reference points to aid geographical interpretation. See Table 2.1 for further details.

consistency in the diagnosed trends of ΔP_{SAM}, ΔP_{Kat}, and the easterly wind stress across three other reanalysis products: JRA-55 (Kobayashi et al., 2015), CFSR (Saha et al., 2010), and MERRA2 (Gelaro et al., 2017), selected because they perform comparably to one another in reproducing measurements from meteorological stations, though not as well as ERA-Interim (Bracegirdle and Marshall, 2012).

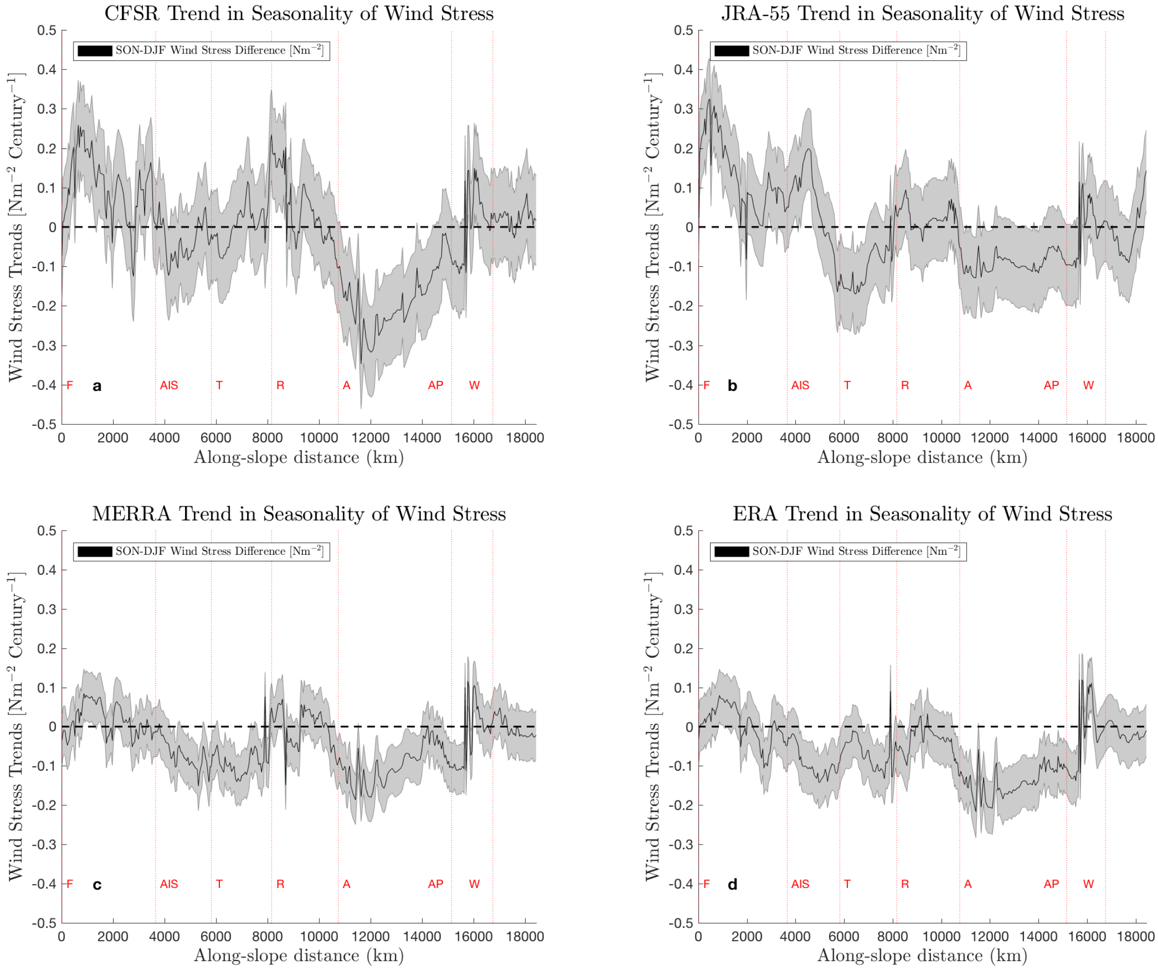

Figure 2.7: Multi-decadal trends in the SON - DJF wind stress difference [$\mathrm{N\,m^{-2}\,Century^{-1}}$] as a function of along-slope distance, error bars are standard deviations from the multi-decadal mean SON-DJF wind stress for (a) 1980-2010 CFSR (Saha et al., 2010), (b) 1972-2013 JRA-55 (Kobayashi et al., 2015), (c) 1980-2015 MERRA2 (Gelaro et al., 2017), and (d) 1979-2014 ERA-Interim (Dee et al., 2011) reanalysis products. Red labels indicate reference points to aid geographical interpretation. See Table 2.1 for further details.

Fig. 2.6 compares the multi-decadal seasonal wind stress trends from the four reanalysis products during DJF and SON ,the seasons that exhibit the strongest and most significant trends in ERA-Interim. As expected, all trends differ quantitatively from one another. Aside from CFSR, all products also demonstrate a strengthening of the easterly wind stress during SON. Moreover, all four products capture the divergence between the DJF and SON trends, implying that all products exhibit a widening of the gap between the weaker DJF easterly wind stress and the stronger SON easterly wind stress. This enhancement appears to be concentrated in approximately the same sectors of the Antarctic coastline. For instance, the Amundsen region shows a stronger change in the difference of the wind stress trend between DJF and SON, consistent with the deepening of the Amundsen Sea low (ASL) (Turner et al., 2013).

To visualize the regional variations of the changes in seasonality and their amplitude compared to the interannual variability, Fig. 2.7 shows the difference in the SON and DJF wind stress trends as a function of distance along the Antarctic slope. Here it is clear that the magnitude of the change in the seasonality of the wind stress depends highly on location. Areas that visually have large summer-to-winter diverging seasonal cycles, especially the Amundsen and East Antarctic region, exhibit the largest trends in the SON-DJF wind stress changes. One caveat specific to the Amundsen region is the impact of ENSO on the depth of the ASL in winter and spring (Clem et al., 2016), which may be a driver of our calculated trends during these seasons.

Table 2.4 summarizes the annual mean wind stress trends, the DJF and SON wind stress trends, and the ΔP_{SAM} and ΔP_{Kat} trends in SON and DJF. Aside from CFSR, all products exhibit annual-mean strengthened easterly wind stress trends. CFSR has been shown to have persistent high temperature biases during winter (Bracegirdle and Marshall, 2012), which may contribute to differing wind stress trends in the multi-decadal and seasonal analyses. In addition, all reanalysis products exhibit a DJF weakening of the easterly wind stress along with a DJF increase of ΔP_{SAM}. Aside from CFSR, all products have a linear trend in the ΔP_{SAM} that is increasing with a significance of less than 10%. We plot the DJF and SON wind stress trends of CFSR, MERRA2, JRA-55, and ERA-Interim in conjunction with the calculated DJF ΔP_{SAM} and ΔP_{Kat} in Fig. 2.8. Similarly to ERA-Interim, all reanalysis products show positive interannual correlations, which implies an eastward anomaly with a strengthened ΔP_{SAM}. This supports a connection between strengthening of the SAM and weakening of the easterlies in austral summer.

Table 2.4 reveals that during SON, all products except for CFSR show an increase of strength in the easterly wind stress and an increase in ΔP_{Kat}. CFSR is an outlier among the products in that it exhibits a weakening, rather than strengthening, of the easterlies and ΔP_{Kat} in SON. The

SON trends in ΔP_{Kat} are significant in MERRA2 and JRA-55, at 1% and 2%, respectively. While MERRA2 also exhibits a stronger intensification of the SON easterlies ($-0.056\,\text{N}\,\text{m}^{-2}\,\text{Century}^{-1}$, $p = 0.04$), the SON intensification of ΔP_{Kat} in JRA is not accompanied by a statistically significant enhancement of the easterlies. MERRA2 is therefore the only product with a positive SON trend in ΔP_{Kat} and a stronger intensification of the SON easterlies which is significant.

Similarly to Fig. 2.8, Fig. 2.9 compares the SON easterly wind stress trends and the calculated ΔP_{Kat} trends. Fig. 2.9 shows that the katabatic winds have the smallest interannual correlation with the wind stress in CFSR. In the other products, the variations in the ΔP_{Kat} can explain about 50% of the variance in the interannual wind stress trends. MERRA2, CFSR and JRA-55 therefore generally support the relationships between ΔP_{SAM}, ΔP_{Kat} and the easterly wind stress inferred from ERA-Interim, though with substantial discrepancies that might be expected based on these products' lower accuracy in reproducing meteorological measurements (Bracegirdle and Marshall, 2012).

2.4 Implications of increased alongshore wind seasonality for near-Antarctic circulation

In §2.1 we provided an overview of the impacts of the easterly winds on near-Antarctic circulation. In our results in §2.3, we found that the annual-mean wind stress has not changed significantly, but that the seasonality of the wind stress has changed substantially. For example, Fig. 2.6(d) shows that the ERA-Interim DJF and SON wind stresses have diverged from one another, with strengthening easterly wind stress in SON and weakening easterly wind stress in DJF. Fig. 2.8 demonstrates the consistency among reanalysis products, and each shows an enhancement of the wind stress difference between DJF and SON.

An increase in the seasonality of the wind stress may have consequences for several aspects of the near-Antarctic circulation. For instance, ice motion trends during autumn, especially in the Pacific and Atlantic sectors of the Antarctic coast, are strongly correlated to the changes in the autumn 10m wind forcing (Holland and Kwok, 2012). Other potential impacts of the near-Antarctic winds on the circulation include changes in AABW export, changes in the properties of

Variable	ERA-Interim	MERRA2	CFSR	JRA-55
Mean Annual Wind Stress Trend [$\mathrm{N\,m^{-2}}$ Century^{-1}]	-.012$^{.25}$	-.045$^{\mathbf{.007}}$	.058$^{\mathbf{.006}}$	-.002$^{.81}$
DJF Wind Stress Trend [$\mathrm{N\,m^{-2}}$ Century^{-1}]	.015$^{.26}$	-.022$^{.15}$	.068$^{\mathbf{.06}}$	-.011$^{.30}$
DJF ΔP_{SAM} [hPa Century^{-1}]	12.7$^{\mathbf{.01}}$	11.1$^{\mathbf{.02}}$	8.19$^{.20}$	20.0$^{\mathbf{.00003}}$
DJF ΔP_{Kat} [hPa Century^{-1}]	-1.68$^{.44}$	-6.57$^{\mathbf{.001}}$	-1.48$^{.66}$	1.40$^{.85}$
SON Wind Stress Trend [$\mathrm{N\,m^{-2}}$ Century^{-1}]	-.04$^{\mathbf{.03}}$	-.056$^{\mathbf{.04}}$	.061$^{\mathbf{.04}}$	-.010$^{.40}$
SON ΔP_{SAM} [hPa Century^{-1}] Trend	-3.28$^{.48}$	-5.56$^{.27}$	-2.09$^{.78}$	12.9$^{\mathbf{.013}}$
SON ΔP_{Kat} [hPa Century^{-1}] Trend	4.04$^{.11}$	8.28$^{\mathbf{.01}}$	1.92$^{.54}$	4.73 $^{\mathbf{.02}}$

Table 2.4: Trends in the circumpolar-averaged alongshore wind stress and meridional pressure gradients with the corresponding statistical p-values in the superscript of each trend. P-values in bold are significant at 10%.

Product	DJF ΔP_{SAM}	SON ΔP_{SAM}	DJF ΔP_{Kat}	SON ΔP_{Kat}
ERA-Interim	$\mathbf{1\times10^{-3}}$	$\mathbf{2\times10^{-5}}$	$\mathbf{3\times10^{-6}}$	$\mathbf{3\times10^{-7}}$
CFSR	$\mathbf{3\times10^{-3}}$	4×10^{-1}	$\mathbf{2\times10^{-7}}$	$\mathbf{1\times10^{-1}}$
JRA-55	$\mathbf{3\times10^{-2}}$	$\mathbf{5\times10^{-4}}$	$\mathbf{8\times10^{-7}}$	$\mathbf{5\times10^{-5}}$
MERRA2	$\mathbf{6\times10^{-3}}$	$\mathbf{6\times10^{-4}}$	$\mathbf{2\times10^{-3}}$	$\mathbf{3\times10^{-6}}$

Table 2.5: P-values of the interannual correlations between ΔP_{SAM}, ΔP_{Kat} and the wind stress. Values in bold are significant at 10%.

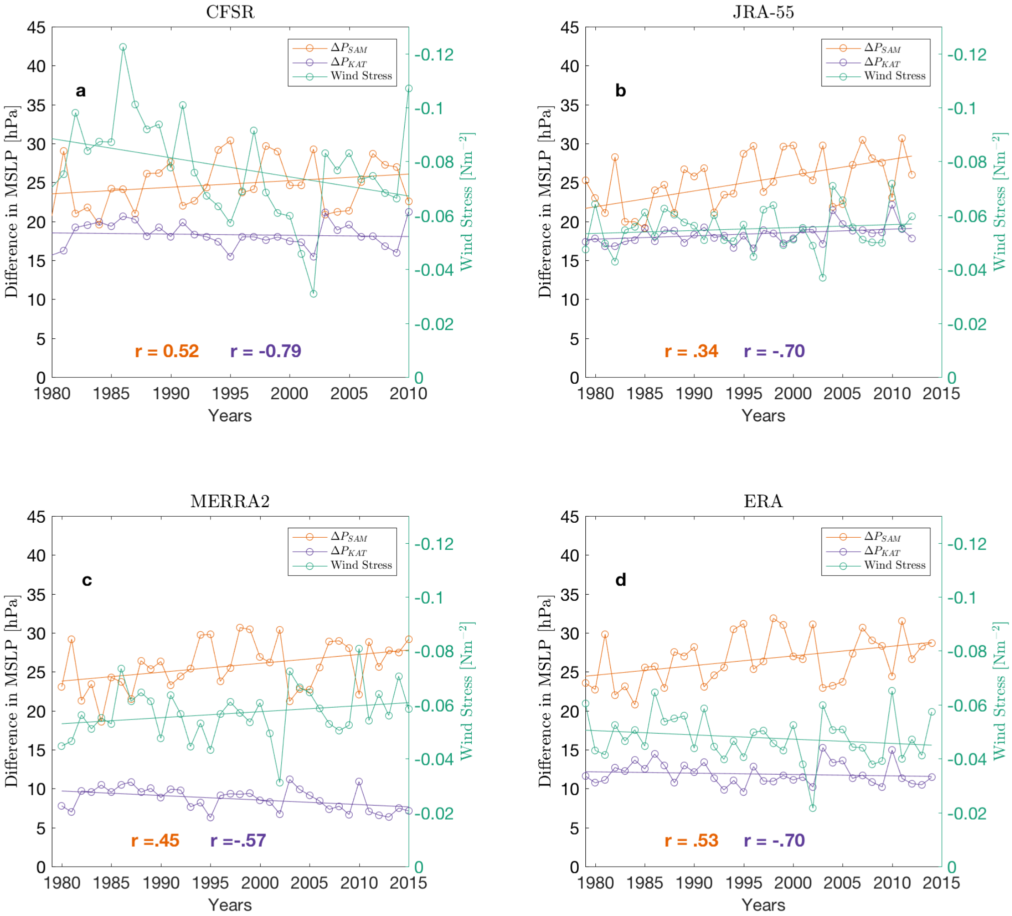

Figure 2.8: Multi-decadal trends in DJF for (a) 1980-2010 CFSR (Saha et al., 2010), (b) 1973-2012 JRA-55 (Kobayashi et al., 2015), (c) 1979-2015 MERRA2 (Gelaro et al., 2017), and (d) 1979-2014 ERA (Dee et al., 2011) reanalysis products. The DJF ΔP_{SAM} [hPa] (orange dots) is plotted with the superimposed DJF ΔP_{SAM} trend (orange line). The DJF ΔP_{Kat} [hPa] (purple dots) is plotted with the superimposed DJF ΔP_{Kat} trend (purple line). On the right y-axis, the DJF mean wind stress is plotted (green) $\mathrm{N\,m^{-2}}$ with the superimposed trend (green line). The correlations between the mean seasonal ΔP_{SAM} and ΔP_{Kat} with the along-slope wind stress are provided in their respective colors.

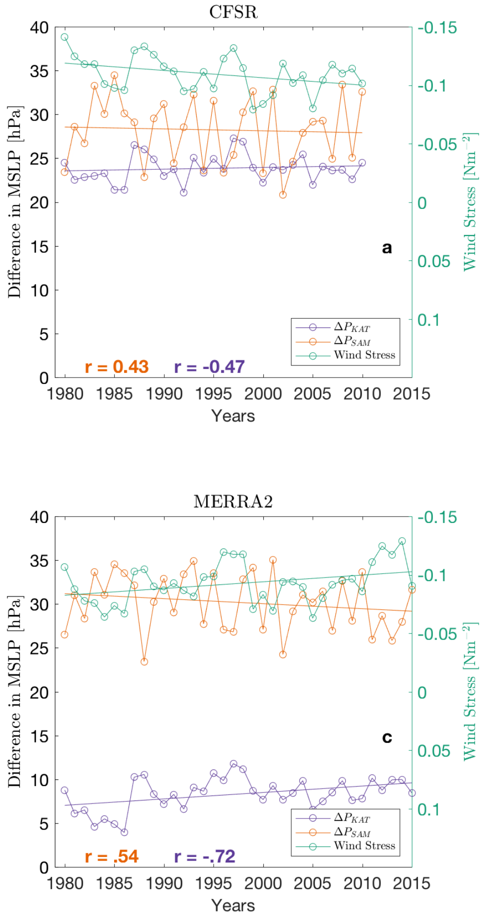

Figure 2.9: Multi-decadal trends in SON for (a) 1980-2010 CFSR (Saha et al., 2010), (b) 1973-2012 JRA-55 (Kobayashi et al., 2015), (c) 1979-2015 MERRA2 (Gelaro et al., 2017), and (d) 1979-2014 ERA (Dee et al., 2011) reanalysis products. The SON ΔP_{SAM} [hPa] (orange dots) is plotted with the superimposed SON ΔP_{SAM} trend (orange line). The SON ΔP_{Kat} [hPa] (purple dots) is plotted with the superimposed SON ΔP_{Kat} trend (purple line). On the right y-axis, the SON mean wind stress is plotted (green) $\mathrm{N\,m^{-2}}$ with the superimposed trend (green line). The correlations between the mean seasonal ΔP_{SAM} and ΔP_{Kat} with the along-slope wind stress are provided in their respective colors.

AABW, and variability in heat transport towards ice shelves.

Easterly winds modify the rate of Antarctic Bottom Water (AABW) formation and export (Jullion et al., 2010; Wang et al., 2012; Su, Stewart, and Thompson, 2014), a process that has global-scale impacts for ocean circulation (Marshall and Speer, 2012). Stronger easterly winds in the southern Weddell and Ross Seas (see Fig. 2.2) enhance export of dense shelf water simply by virtue of a stronger shoreward Ekman transport and deep offshore return flow (Stewart and Thompson, 2012; Stewart and Thompson, 2013), and/or by depressing the pycnocline at the shelf break and enhancing the overflow through the Filchner trough (Kida, 2011; McKee et al., 2011). The wind stress trends shown in Fig. 2.2 may also be expected to produce a stronger baroclinicity of the Weddell and Ross gyres (McKee et al., 2011). Export of dense water would be enhanced as an effect of stronger thermal wind forcing. A stronger gyre would promote a doming of isopycnals in the center of the gyre and a deepening of isopycnals at the gyre rim (Jullion et al., 2010).

The seasonal trends (Fig. 2.4), as well as the enhancement of the seasonal cycle in the strength of the easterly winds (Fig.2.6), project onto the mechanisms that form and export dense water from Antarctica. Weddell Sea Bottom Water (WSBW) and Weddell Sea Deep Water (WSDW) are precursors to AABW in the Weddell Sea (Orsi, Johnson, and Bullister, 1999). The export of these dense water masses from the Filchner Trough and the transport towards the Antarctic Peninsula is mediated by seasonal variations in the along-slope winds (Wang et al., 2012). Additionally, a change in wind stress seasonality may influence export of WSDW northward from the deep Weddell Gyre via the Orkney Passage by modulating the seasonal cycle in the gyre's baroclinicity (Meredith et al., 2008; Su, Stewart, and Thompson, 2014). AABW export reaches a peak outflow from the Weddell gyre in austral autumn and a minimum in austral spring (Gordon et al., 2010). Therefore, an increase (decrease) in the easterlies in austral autumn (spring) may lead to an increase (decrease) in AABW export.

Properties of AABW are closely tied to the seasonal circum-Antarctic wind forcing. In the Ross Sea, winter intensification of the winds shifts the Antarctic Slope Front poleward and suppresses High Salinity Shelf Water (HSSW) export (Gordon, Huber, and Busecke, 2015), a process that may have intensified as a result of the SON enhancement of the easterlies. This produces warm, fresh bottom water in contrast to the salty, cold waters of autumn and winter when there are generally weaker winds. The amplification of the seasonal trends in the wind stress may therefore act to enhance the seasonal variations in AABW properties.

Seasonal changes in wind forcing may also project onto oceanic heat transport toward the continent. The trend towards weaker austral summer and spring easterly wind stress adjacent to the Amundsen and Bellingshausen Seas (see Fig. 2.4(f,j)), where the ACC lies closest to the continent, may be enhancing the shoreward flux of CDW (Thoma et al., 2008), and contributing to the ongoing warming of these west Antarctic continental shelves (Schmidtko et al., 2014). Fig. 2.4(j) shows this substantial ($\sim$0.05$\mathrm{N/m^2}$) weakening of the easterlies in austral Spring. The ice shelf thinning seen in West Antarctica (Rignot et al., 2013) may be tied to the trends apparent in the wind stress.

Offshore of the Fimbul Ice Shelf, two wind-influenced mechanisms of shoreward heat transport have been identified that are tied to the easterly wind stress: Ekman transport of relatively warm summer surface water (Zhou et al., 2014), and deep intrusion of CDW (Nøst et al., 2011; Hattermann et al., 2014). Our calculated wind stress trends that show a reduction of the strength of the easterlies in austral summer will limit the available warm water at the ice shelf front during the summer, thus reducing melt. However, the same trend in the easterlies will enhance the intrusion of CDW, with more CDW intrusion expected in summer and autumn (Spence et al., 2014). Antarctica's floating ice shelves in may therefore be expected, on average, to exhibit reduced melt adjacent to the ice shelf face and enhanced melting close to their grounding lines, though with substantial variations associated with the spatially-inhomogeneous wind stress trends.

2.5 Conclusions

In this chapter, we quantified the multi-decadal change in the easterly surface wind forcing around Antarctica using ERA-Interim reanalysis data and compared our findings with three other reanalysis products that compare favorably with Antarctic meteorological measurements (Bracegirdle, 2013; Bromwich, Nicolas, and Monaghan, 2011). The emphasis in this study is on the alongshore component of the surface forcing, as this component is most relevant for cross-slope exchange of water masses *e.g.* Thompson et al., 2014. We find that despite the increase in SAM in recent decades, the easterlies have on average strengthened by $.0044\,\mathrm{N\,m^{-2}}$, or by around 7%, though this trend is not statistically significant. This corresponds to an anomalous shoreward Ekman transport of around 0.6 Sv around the $\sim$18,000km length of the Antarctic shelf break. The annual-mean wind stress trend differs substantially between reanalysis products, but an aggregation of these products similarly indicates little overall change in the annual-mean wind stress (see Table 2.4).

In contrast, the ERA-Interim wind stress exhibits substantial seasonal trends, in particular a widening of the gap between the weaker summer easterlies and the stronger winter easterlies (see Table 2.3). In DJF and MAM, this amounts to the easterly wind stress trend weakening by $.0055\,\mathrm{N\,m^{-2}}$ (12%) and $.0022\,\mathrm{N\,m^{-2}}$ (3%), equivalent to offshore Ekman transport anomalies of approximately 0.7 Sv and 0.3 Sv, respectively. In JJA and SON, the easterlies have strengthened by $.0112\,\mathrm{N\,m^{-2}}$ (15%) and $.0143\,\mathrm{N\,m^{-2}}$ (22%), equivalent to shoreward Ekman transport anomalies of 1.5 Sv and 1.9 Sv, respectively. There are substantial regional departures from these circumpolar-average trends, as shown in Figs. 2.3 and 2.4, with seasonal trends reaching $0.05\,\mathrm{N\,m^{-2}}$ along various stretches of the shelf break. Despite widely varying annual-mean trends, all reanalysis products examined here exhibit a qualitatively similar widening of the gap between the SON and DJF easterly wind stresses (see Figs. 2.6 and 2.7).

In §2.3.3 we investigated the extent to which the wind stress trends can be attributed to the trends in the SAM, quantified via ΔP_{SAM}, and to the pole-to-coast pressure gradient ΔP_{Kat} that drives the katabatic winds. On interannual timescales the easterly wind stress is correlated with both ΔP_{Kat} and ΔP_{SAM}, with the former explaining more of the variance than the latter ($\sim$50% vs. $\sim$25%) in both DJF and SON. The seasonal trends show a decrease in the strength of the easterlies accompanied by an increase in ΔP_{SAM} in DJF. In SON, the trends reveal an increase in the strength of the easterly wind stress accompanied by an increase in ΔP_{Kat}. This suggests a summer weakening of the easterlies due to the southward shift of the westerlies and spring intensification of the easterlies due to a stronger driving of the katabatic winds. However, while these were unambiguously the strongest pressure gradient and wind stress trends in ERA-Interim, only the summer SAM trend and winter strengthening of the easterlies were statistically significant at the 10% level. Further scrutiny of these relationships will therefore be required in order to establish their robustness.

We have examined the surface wind stress, rather than the wind speed. We made this choice because it is the momentum transfer from the atmosphere to the ocean that is most relevant to the near-Antarctic circulation, as outlined in §2.1 and §2.4. However, we are unable to distinguish directly if changes in the sea ice cover, which changes the surface roughness (Lüpkes and Birnbaum, 2005), might be contributing to the trends. In the Appendix, we show that the trends in the ERA-Interim 10m wind speed are qualitatively similar to the trends in the wind stress. The alongshore wind speed exhibits increases in seasonality that are qualitatively similar to the wind stress trends in all reanalysis products. Furthermore, in the Appendix we construct an independent approximation of the alongshore wind stress trends, derived from the wind speeds via a simple quadratic bulk formula, and find quantitatively similar trends as reported by the model. We therefore infer that the trends in the wind stress are primarily a result of changes in the winds, rather than changes in sea ice conditions. However, sea ice can efficiently redistribute momentum laterally, and further work will be required to determine how changes in sea ice properties are contributing to the trends in the momentum input to the ocean (Leppäranta, 2011).

Another caveat to this analysis is that reanalysis products are relatively poorly constrained close to Antarctica due to sparse measurements (see Saha et al., 2010; Rienecker et al., 2011; Dee et al., 2011; Kobayashi et al., 2015). This motivated a comparison of our results across four different products that have been evaluated using Antarctic meteorological measurements, with ERA-Interim exhibiting substantially smaller decadal-mean biases in MSLP and geopotential height than the other three (Bracegirdle and Marshall, 2012). In turn, ERA-Interim's low MSLP biases motivated our attribution of the diagnosed wind stress trends to annular meridional pressure gradients, specifically ΔP_{SAM} and ΔP_{Kat}, the latter being defined as an analogue of the SAM. Changes in the strength of the westerly wind belt and intensification of the katabatic winds could be more directly quantified, and may offer a less ambiguous attribution of the wind stress trends. In §2.3 we compared these reanalysis products over their full respective time spans, which may be expected to introduce slight differences between the trends derived from different products. In the Appendix in §2.6, we re-calculate the trends over a uniform period (1980–2010) and find qualitatively similar results, though the ERA-Interim and MERRA2 easterly wind strengthening in SON is no longer statistically significant over this shorter analysis period.

In §2.4, we discussed qualitatively how the calculated trends may impact specific aspects of the regional Antarctic circulation. Given the wide range of Antarctic ocean processes that are tied to the easterly winds, there may be a specific connection between these wind stress trends, the observed multi-decadal changes in water mass properties around the Antarctic margins (Schmidtko et al., 2014), and the ongoing warming and freshening of AABW (Purkey and Johnson, 2010). Further work is necessary to quantify the ocean's response to multi-decadal changes in the easterly wind belt.

2.6 Appendix

2.6.1 Analysis of the Seasonal Wind Trends

We focus on the seasonal easterly wind stress trends, rather than the wind speed trends, because the wind stress more directly impacts the ocean circulation. For comparison, we now repeat our seasonal trend analysis for the wind speed. We first provide in Fig. 2.10 seasonal plots of the zonal and meridional 10m winds in ERA-Interim.

For comparison, we also calculate the 10m wind trends from 1980–2010 CFSR (Saha et al., 2010) 1979–2015 MERRA (Rienecker et al., 2011) and 1973–2012 JRA-55 (Kobayashi et al., 2015), and 1979–2014 ERA-Interim (Dee et al., 2011). Fig. 2.11 shows the SON and DJF alongshore wind trends diagnosed from all four reanalysis products. These figures indicate that the wind stress trends are primarily due to changes in the winds, rather than, *e.g.*, changes in surface roughness associated with sea ice.

To quantify the influence of the wind speed trends on the wind stress trends we performed an independent estimate of the wind stress trends using a simple quadratic drag law,

$$\tau = \rho C_{\mathrm{d}} |u_{10}| u_{10}.$$

Here $\rho = 1.023\,\mathrm{kg\,m^{-3}}$ is a constant reference density of dry air, $C_{\mathrm{d}} = 2 \times 10^{-3}$ is a typical bulk drag coefficient for sea ice (Lüpkes and Birnbaum, 2005), and $\mathbf{u_{10}}$ is the 10 m wind horizontal velocity vector. In Fig. 2.12, we reproduce Fig. 2.6, but using the stress derived via the above drag law. The DJF and SON alongshore wind stress trends are both qualitatively and quantitatively similar between the two figures, indicating that the reported wind stress trends are primarily due to

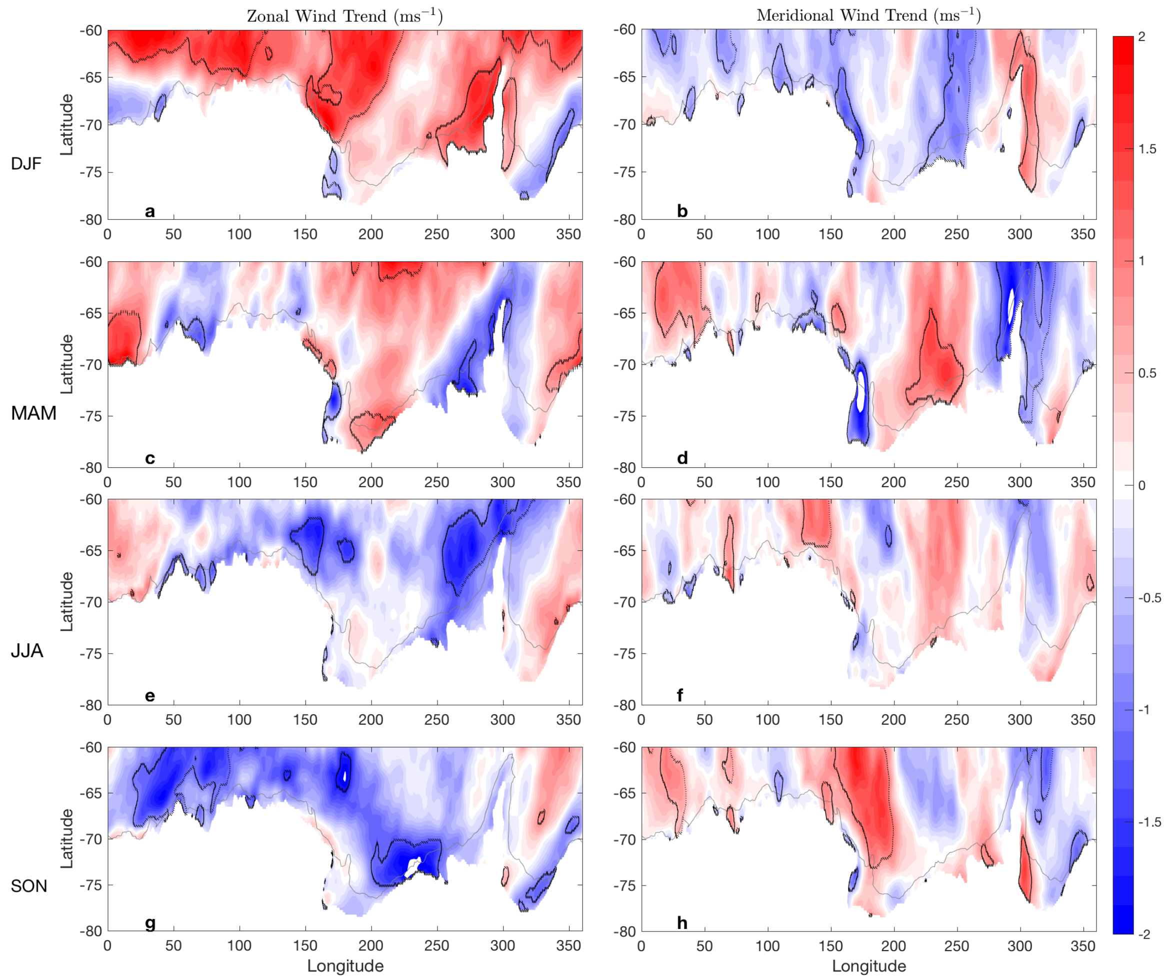

Figure 2.10: Multi-decadal trends in the seasonal-mean zonal and meridional 10m winds (in m/s), calculated from 1979–2015 ERA-Interim reanalysis data (Dee et al., 2011). Black contours envelop trends that are statistically significant at the 10% level. (a) DJF zonal wind trend, (b) DJF meridional wind trend, (c) MAM zonal wind trend, (d) MAM meridional wind trend, (e) JJA zonal wind trend, (f) JJA meridional wind trend, (g) SON zonal wind trend, and (h) SON meridional wind trend.

changes in the wind speed.

Figure 2.11: The multi-decadal trend in the DJF and SON along-slope 10m winds (in m/s), calculated from 1979-2015 MERRA2 (Rienecker et al., 2011) data, 1980-2010 CFSR Saha et al., 2010 data, 1973-2012 JRA-55 (Kobayashi et al., 2015) data, and 1979–2014 ERA-Interim reanalysis (Dee et al., 2011) data.

2.6.2 Comparison against the Antarctic Mesoscale Prediction System

To evaluate the impact of reanalysis resolution on representation of the near-coastal winds, we compare the ERA-Interim winds against the output of the Antarctic Mesoscale Prediction System (AMPS) forecast (Hines et al., 2011) over the period that AMPS data is available (2006–2015). Fig. 2.13(e) shows the difference between the mean 10m winds in ERA-Interim and AMPS. For

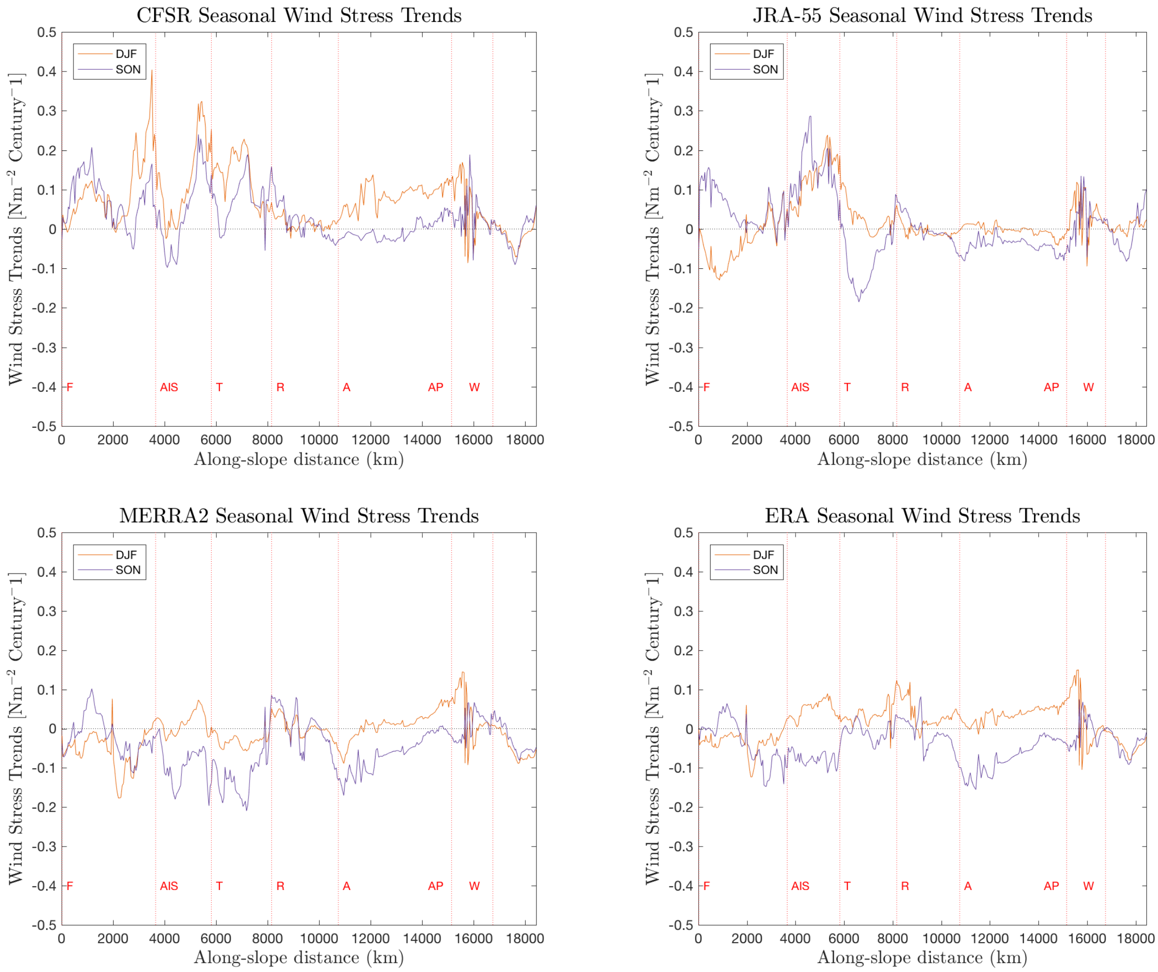

Figure 2.12: The multi-decadal trend in the DJF and SON along-slope wind stress (in N m^{-2} Century^{-1}) calculated from the respective 10m wind speeds, for 1979-2015 MERRA2 (Rienecker et al., 2011) data, 1980-2010 CFSR Saha et al., 2010 data, 1973-2012 JRA-55 (Kobayashi et al., 2015) data, and 1979–2014 ERA-Interim reanalysis (Dee et al., 2011) data.

this comparison, the AMPS wind velocity data was rotated and interpolated onto the same regular latitude/longitude grid as ERA Interim. A key difference is that the coastal winds in ERA-Interim are consistently slower than in AMPS, likely due to the higher resolution used in the latter. The AMPS mid-latitude westerly winds are also stronger than in ERA-Interim. The differences in the mean wind are of comparable magnitude to the diagnosed multi-decadal trends in ERA-Interim.

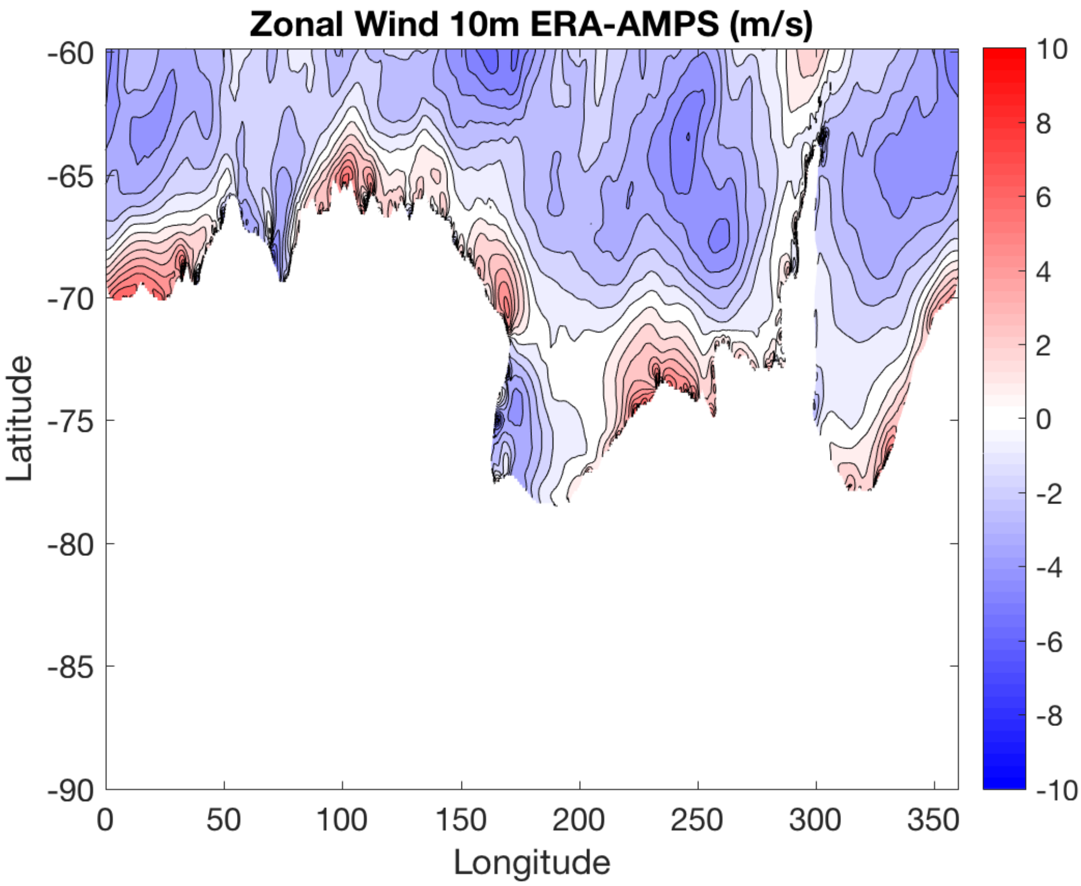

Figure 2.13: The difference in the 2006–2014 averaged 10m zonal wind between ERA-Interim (Dee et al., 2011) and AMPS. AMPS data has been provided by the Byrd Polar Research Center's Polar Meteorology Group at Ohio State University. Land points have been removed to highlight the ocean regions relevant to this study.

2.6.3 Calculation of Katabatic Index from Surface Pressure

The calculation of ΔP_{Kat} relies on the MSLP at 65°S and 85°S, and the South Pole at 85°S lies at a high elevation of 2700m. In order to investigate whether the results of ΔP_{Kat} are biased by the methods that reanalysis products reduce the surface pressure to MSLP, we calculated an independent estimate of the MSLP from the reported surface pressures in all products. We use the hypsometric equation to find the seasonal zonal MSLP at 85°S and 65°S as follows,

$$\mathrm{MSLP} = P_{\mathrm{surf}} \exp \frac{Zg_0}{R_d T_v}.$$

Here P_{surf} is the reanalysis-reported surface pressure, R_d is the universal gas constant, g_0 is gravity, Z is the height above sea level, and T_v is virtual temperature. In Figs. 2.14 and 2.15, we reproduce Figs. 2.8 and 2.9 using our independent estimate of ΔP_{Kat}. The time-mean values of ΔP_{Kat} shown in Figs. 2.14 and 2.15 differs from those shown in Figs. 2.8 and 2.9, typically by around 10 hPa, due to our relatively simplistic method of estimating MSLP. However, the interannual correlations and multi-decadal tends in ΔP_{Kat} are very similar. We therefore conclude that reanalysis-specific procedures for estimating MSLP do not influence our main results.

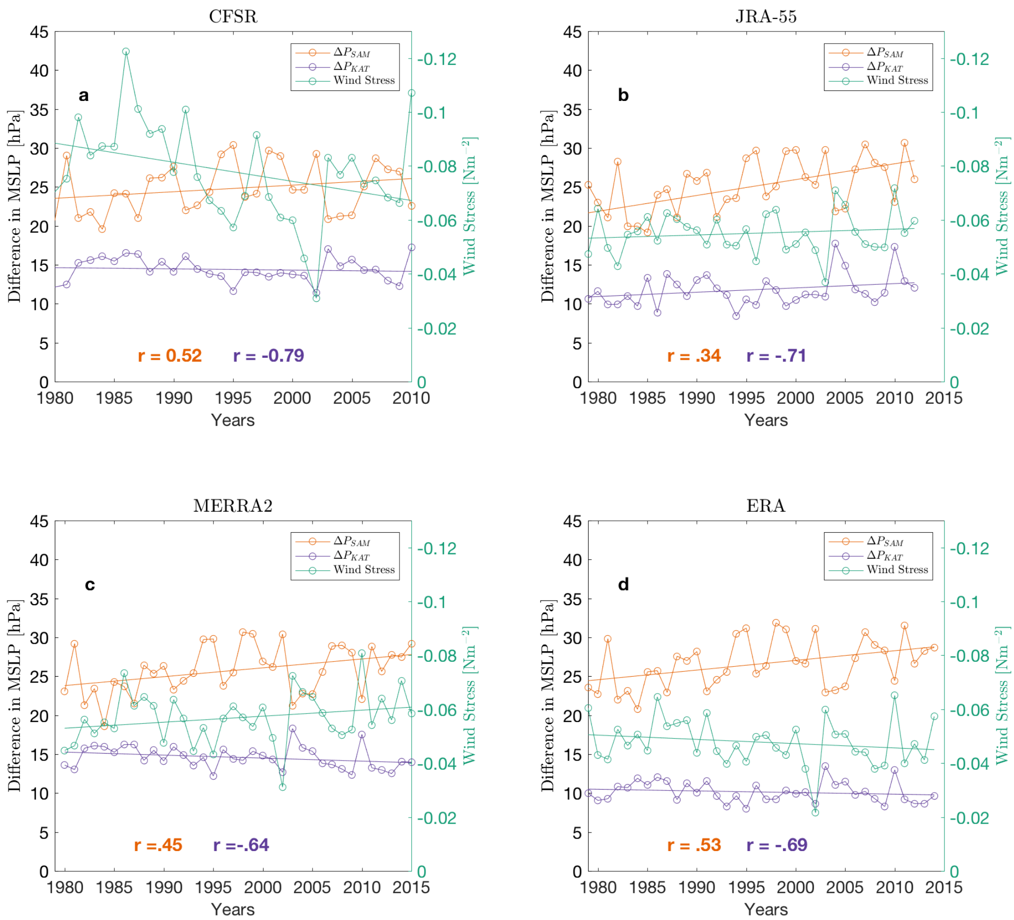

Figure 2.14: As in Fig. 2.8, but calculating the DJF ΔP_{Kat} using the hypsometric equation in order to calculate the MSLP at 85°S and 65°S from reanalysis surface pressure, 2m temperature, and geopotential height.

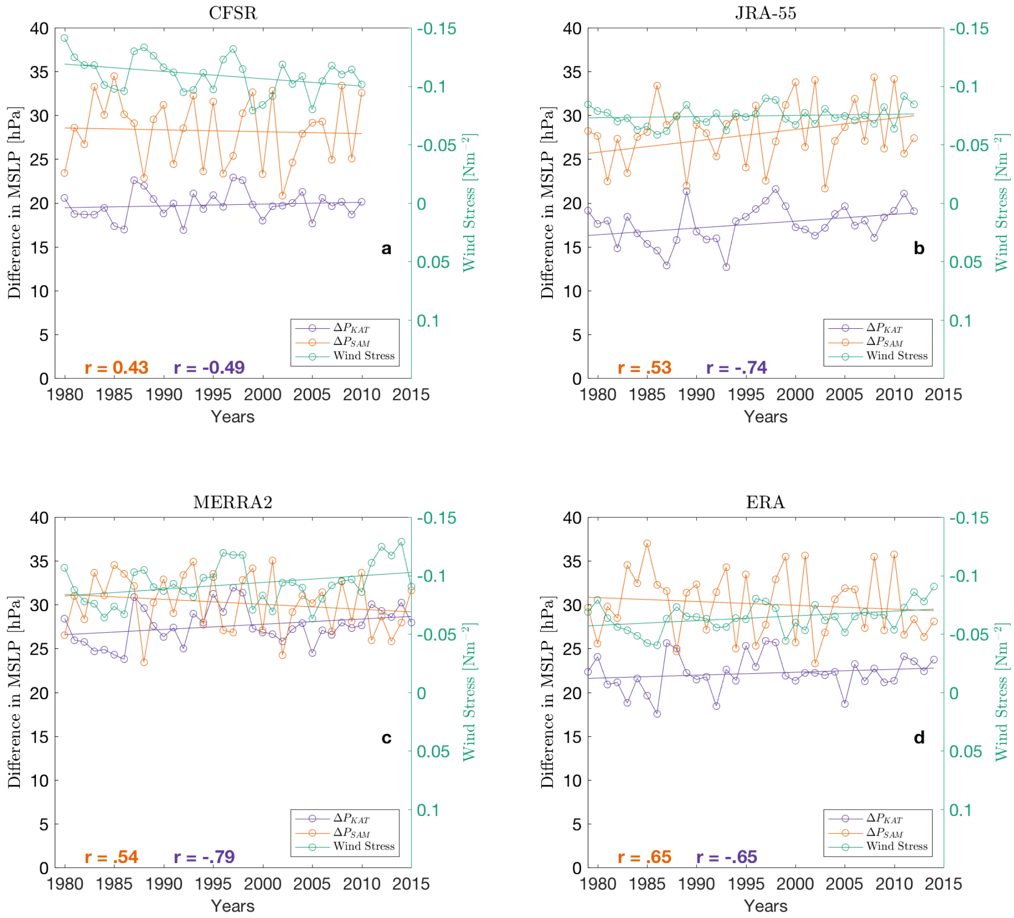

Figure 2.15: As in Fig. 2.9, but calculating the SON ΔP_{Kat} using the hypsometric equation in order to calculate the MSLP at 85°S and 65°S from reanalysis surface pressure, 2m temperature, and geopotential height.

2.6.4 Calculation of the interannual trends using a consistent 1980-2010 time period

In §2.3 we reported trends calculated over the full time span of each reanalysis product, which differ slightly from one another. In Table 2.6 we present a re-calculation of the trends and *p*-values reported in Table 2.4, but using a uniform time period of 1980–2010 across all reanalysis products. There is little change in the JRA55 and CFSR trends because their analysis periods differ little between Tables 2.4 and 2.6. In ERA-Interim and MERRA2 there are some more substantial changes. For example, while these products still report a strengthening of the easterly wind stress in SON over 1980–2010, these trends are no longer statistically significant.

Variable	ERA-Interim	MERRA2	CFSR	JRA-55
Mean Annual Wind Stress Trend [$\mathrm{N\,m^{-2}}$ Century^{-1}]	-.005$^{.80}$	-.029$^{.15}$	.058$^{\mathbf{.006}}$	-.007$^{.48}$
DJF Wind Stress Trend [$\mathrm{N\,m^{-2}}$ Century^{-1}]	.013$^{.45}$	-.020$^{.31}$	.069$^{\mathbf{.06}}$	-.003$^{.86}$
DJF ΔP_{SAM} [hPa Century^{-1}]	14.01$^{\mathbf{.02}}$	10.2$^{\mathbf{.10}}$	8.20$^{.20}$	16.6$^{\mathbf{.01}}$
DJF ΔP_{Kat} [hPa Century^{-1}]	-.320$^{.96}$	-2.75$^{.29}$	-1.48$^{.66}$	2.22$^{\mathbf{.004}}$
SON Wind Stress Trend [$\mathrm{N\,m^{-2}}$ Century^{-1}]	-.015$^{.44}$	-.012$^{.69}$	.061$^{\mathbf{.04}}$	-.012$^{.42}$
SON ΔP_{SAM} [hPa Century^{-1}] Trend	-2.27$^{.76}$	-1.44$^{.82}$	-2.10$^{.78}$	12.1$^{\mathbf{.09}}$
SON ΔP_{Kat} [hPa Century^{-1}] Trend	1.50$^{.68}$	7.20$^{\mathbf{.06}}$	1.85$^{.54}$	6.07$^{\mathbf{.03}}$

Table 2.6: Trends in the circumpolar-averaged alongshore wind stress and meridional pressure gradients with the corresponding statistical p-values in the superscript of each trend for years 1980-2010. P-values in bold are significant at 10%.

CHAPTER 3

Development of a Regional Model of the Weddell Sea

3.1 Background

In §2, we diagnose the trend in the near-Antarctic easterly wind stress. We deduce that the along-slope Antarctic wind stress has experienced an amplification in the seasonality of the along-slope wind stress. Changes to the near-Antarctic wind stress have significant implications for regional circulation; for instance, wind stress has been identified as an influence in AABW warming (Schmidtko et al., 2014) and freshening (Purkey and Johnson, 2010) seen in observations. As discussed in §1, the Weddell Sea has an important impact on the broader ocean and climate system (*e.g.* Gordon et al., 2009; Toggweiler, 2008; Toggweiler, Russell, and Carson, 2006). Although past modeling attempts referenced in §1 are successful in quantifying and describing the circulation of the Weddell (Timmermann, Beckmann, and Hellmer, 2002; Beckmann, Hellmer, and Timmermann, 1999; Hellmer et al., 2012; Hellmer et al., 2017), few studies focus on the role of small-scale, high frequency processes such as eddies and tides that exert influence over the rates of water mass exchange, mixing, and AABW formation (Stewart and Thompson, 2016; Newsom et al., 2016; Fer, Darelius, and Daae, 2016).

We develop a regional model of the Weddell Sea, with the goal to eventually refine the model to reach an eddy-resolving horizontal resolution of 1km ($\frac{1}{24}^{th}$ degree) (St-Laurent, Klinck, and Dinniman, 2013). At such a fine resolution, the model will have the capacity to capture important length and time-scales of the flows that describe mesoscale eddies and tides. In addition, mesoscale eddies have been identified as principle contributors to CDW transport across the shelf (Nøst et al., 2011) and to AABW export (Nakayama et al., 2014). A high-resolution regional model of the Weddell Sea will allow us to identify the roles of eddies and tides in cross-shelf heat transport and freshwater exchange, as well as to quantify and understand water masses involved in the closure of the meridional overturning circulation.

3.2 Model Framework

3.2.1 Goals for Weddell Sea Regional Model

Several key goals are prioritized in the development of the Weddell Sea regional model The major concern in model development is to ensure that the WSRM simulates the governing processes of near-Antarctic circulation. To satisfy this condition, the WSRM must simulate the thermodynamics and dynamics of sea ice to include sea ice velocity, thickness, and ocean-atmosphere heat and momentum transfer (Renner and Lytle, 2007). A representation of sea ice within the Weddell sea is necessary to capture salt fluxes to the ocean. Ice-ocean salt fluxes are fundamental to dense water production, which ultimately closes the meridional overturning circulation (*e.g.* Jacobs, 2004).

In addition to sea ice, the WSRM must simulate ice shelves and ice shelf cavity circulation. Over 50% of Antarctica's continental margins are covered by ice shelves (Fox, Paul, and Cooper, 1994). At the termination of ice shelves, continental ice sheets meet the ocean and the ice floats. The volumes of the ocean beneath the floating ice shelves are referred to as ice shelf cavities (Losch, 2008). Circulation within Antarctica's ice shelf cavities is crucial to the formation of many water masses and processes. Depending on the location along the Antarctic coast, either warm, salty Modified Circumpolar Deep Water (mCDW) or High Salinity Shelf Water (HSSW) from latent heat release and ice production floods the ice shelf cavities, which leads to basal melt of the ice shelves. The ensuing freshwater flux from the Antarctic margins is transported to the Southern Ocean, reaching transport values of 28 mSv (Hellmer, 2004). As meltwater rises from depth, refreezing occurs during the formation of Ice Shelf Water (ISW) due to the pressure dependence of freezing (Millero, 1978). ISW mixes with HSSW to form Weddell Sea Bottom Water (WSBW) and closes the MOC. The "ice pump" mechanisms (Lewis and Perkin, 1986) that describe ice shelf-ocean interaction are fundamental to modeling the near-Antarctic system.

Aside from simulating the ice-ocean state near Antarctica in terms of sea ice and shelf ice, we aim for the WSRM to span a sufficiently large portion of the Weddell gyre. This avoids spurious regional boundary effects that influence circulation around the southern and western continental shelves and slopes. Aside from boundary effects, seasonal modulation of the along-shore winds and sea surface temperature upstream influence ice shelf cavity properties and circulation at the FRIS (Graham et al., 2013). Given that the Antarctic Slope Front (ASF) flows east to west and is a nearly circumpolar current (Jacobs, 1991), advection of temperature and salt anomalies can influence the seasonal cycle of down-stream ice shelf properties.

Finally, the model must reach a statistically steady equilibrium with its boundary conditions to allow for quantification of water mass properties, circulation, and melt rate. By evaluating the month-to-month variability in important model diagnostics such as integrated salt, temperature, and melt rate, we can better understand when the model has reached a steady-state. In this chapter as well as in §4, data used for WSRM analysis will be averaged over the last full atmospheric forcing period (further discussed in §3.2.8).

3.2.2 Implementing MITgcm Framework in the WSRM

MITgcm framework is used to solve the hydrostatic, Boussinesq primitive equations on a latitude/longitude grid (Losch, 2008). The MITgcm uses depth ('z') coordinates with partial-cell topography (Adcroft, Hill, and Marshall, 1997). This approach is superior to the 'staircase' vertical grid approach and approaches the fidelity of terrain-following coordinates. The WSRM can thus have a vertical grid where pressure surfaces are horizontal to avoid "hydrostatic inconsistency". At the same time, the gridcells can be partially 'wet' to match topography.

MITgcm solves the classical form of the incompressible Boussinesq Navier Stokes equations. These equations govern the state of the ocean in time. The oceanic state depends upon velocity, tracers including temperature and salinity, normalized pressure, and density. We present the governing equations as follows:

$$\underbrace{\frac{D\vec{\mathbf{v}}_h}{Dt} + f\hat{\mathbf{k}} \times \vec{\mathbf{v}}_h + \frac{1}{\rho_c}\nabla_z p = \vec{\mathscr{F}},}_{\text{Horizontal Momentum}} \tag{3.1a}$$

$$\underbrace{\frac{Dw}{Dt} = -\frac{\partial p}{\partial z} - g,}_{\text{Vertical Momentum}} \tag{3.1b}$$

$$\underbrace{\nabla_z \cdot \vec{\mathbf{v}}_h + \frac{\partial w}{\partial z} = 0,}_{\text{Continuity}} \tag{3.1c}$$

$$\underbrace{\rho = \rho(\theta, S),}_{\text{Density}} \tag{3.1d}$$

$$\underbrace{\frac{D\theta}{Dt} = \mathscr{Q}_\theta}_{\text{Potential Temperature}} \quad , \tag{3.1e}$$

$$\underbrace{\frac{DS}{Dt} = \mathscr{Q}_s\,.}_{\text{Salinity}} \tag{3.1f}$$

In these equations above, z is the vertical coordinate, t is time, $\vec{\mathbf{v}} = (u, v, w) = \vec{\mathbf{v}}_h$ is the horizontal velocity vector, ρ is density, θ is potential temperature, and S is salinity. While MITgcm is capable of solving the non-hydrostatic form of these equations, the hydrostatic form of the vertical momentum equation is used where the left side of equation (3.1b) is set to zero.

$$\frac{D\vec{\mathbf{v}}_{\mathbf{h}}}{Dt} = \frac{\partial \vec{\mathbf{v}}_{\mathbf{h}}}{\partial t} + (\nabla \times \vec{\mathbf{v}}_{\mathbf{h}}) \times \vec{\mathbf{v}}_{\mathbf{h}} + \nabla \left[\frac{1}{2} (\vec{\mathbf{v}}_{\mathbf{h}} \cdot \vec{\mathbf{v}}_{\mathbf{h}}) \right] + w \frac{\partial \vec{\mathbf{v}}_{\mathbf{h}}}{\partial z}. \tag{3.2}$$

Note that the vector invariant form of equations (3.1a) written in equation (3.2) is used, which expresses the advection of momentum as the sum of the gradient of the kinetic energy and the vector cross product of the velocity and vorticity. The vector invariant equations are invariant under coordinate transformations and are applied uniformly in any orthogonal curvilinear coordinate system such as a spherical-polar grid used in our regional model configuration.

3.2.3 WSRM Domain Configuration

The spherical–polar WSRM grid extends from (83.5–64°S) in the latitudinal direction and from (-83.5–21°E) longitudinally. As noted in §3.2.1, this domain size allows for the simulation of the Weddell gyre and the region zonally upstream to the east, while excluding the ACC. The horizontal grid spacing scales with the cosine of the latitude.

The vertical grid has 139 levels in order to resolve the hydrographic structure of the water column as well as to resolve as many baroclinic modes as possible (Stewart et al., 2017). In the uppermost five vertical layers, the resolution is less than $\mathcal{O}$(10m). At this resolution, the shallow austral summer mixed layer can be resolved that reaches as shallow depths as 8m (Fahrbach, Rohardt, and Krause, 1992; Gill, 1973). Along the continental slope, the vertical resolution coarsens to $\mathcal{O}$(50m)-$\mathcal{O}$(100m). While coarse, this resolution can enable resolution of downslope flows of AABW when in conjunction with fine (O(1-2km)) horizontal resolution (Stewart and Thompson, 2015a). The resolution is $\mathcal{O}$(250m) down to the bottom of the model vertical grid at 5000m.

The vertical resolution within the FRIS is $\mathcal{O}$(25m) to resolve the density stratification and baroclinic flows throughout the cavity. Vertical resolution finer than $\mathcal{O}$(100m) is necessary to capture the sharpness of the pycnocline beneath the ice shelf and reduce spurious vertical mixing due to an unstable temperature distribution (Losch, 2008). The WSRM vertical resolution sufficiently resolves the cavity geometry as well as its impact on ocean circulation and shelf melt rate (De Rydt et al., 2014) as best as our computing power permits.

Model configuration parameters related to the model grid, pressure solver, and time-stepping are listed in table 3.1. WSRM simulations advance forward in time with staggered-baroclinic timestepping at a timestep of 480 seconds with thermodynamic variables are offset in time by a half timestep from the dynamic variables. The 7^{th}-order one-step method advection scheme is implemented for the advection of tracer and sea ice concentration and thickness. In terms of the pressure solver, although MITgcm is capable of solving the non-hydrostatic 3D equations, we employ MITgcm to solve for pressure by taking the divergence of the depth integral in equation (3.1a).

Listed in table 3.2 are important dissipation and momentum parameters used in the WSRM setup. Currently, lateral dissipation with grid-dependent biharmonic viscosity is parameterized in the WSRM. Biharmonic viscosity enhances the scale selectivity of the viscous operator; the viscosity acts on terms at the gridscale but not on larger scale motions. Leith viscosity may be added in the future when the grid is interpolated to a finer horizontal resolution. ‘Free-slip’ conditions are also applied in the model with zero lateral stress on the boundaries. However, dissipation is added in the vertical with a stress that is a quadratic function of the mean flow over topography. The K-Profile-Parameterization (KPP) scheme (Large, McWilliams, and Doney, 1994) is implemented to handle vertical mixing in open boundary layer and the interior of the WSRM. KPP unifies various processes involved in vertical mixing, including the expressions of non-local transport and diffu-

Table 3.1: Model Configuration: Grid, Pressure Solver, and time-stepping

Parameter	**Description**	**Value**
UsingSphericalPolarGrid	Spherical-Polar Grid(horizontal vectors delX, delY)	True
Nx	Number x-coordinate gridpoints	304
Ny	Number y-coordinate gridpoints	224
Nr	Number z-coordinate gridpoints	139
cg2dMaxIters	Upper limit on 2d con. grad iterations	1000
cg2dTargetResidual	2d con. grad target residual	1e-12
useSRCGsolver	Use conjugate gradient solver with single reduction	True
multidimAdvection	Multi-Dimensional Advection	True
tempstepping	Adams Bashworth time-stepping	False
staggerTimeStep	Staggered Baroclinic timestepping	True
eosType	Equation of State	JMD95P
readBinaryPrec	Precision Used for reading binary files	64
useSingleCpuIO	Only Master Process	true
deltaT	Time–Step	480s

sivity in the boundary layer. Both implicit diffusion and viscosity are implemented in accordance with KPP.

3.2.4 WSRM Shelf Ice and Topography

Antarctic ice sheet topography, ice cavity, and ocean bathymetry are interpolated to the WSRM grid from the RTOPO-1 dataset (Timmermann, 2010). RTOPO-1 improved upon the existing 1-minute BEDMAP 2004 topography around Antarctica by adding a high-resolution gridded BEDMAP topography for the ice shelves.

Sub-ice-shelf freezing and melting is parameterized in the WSRM with a modified three equation thermodynamic formulation from Jenkins, Hellmer, and Holland (2001) and adapted to MIT-

Table 3.2: Model Configuration: Dissipation , Momentum, and Tracer Parameters

Parameter	Description	Value
viscA4Grid	grid-dependent biharmonic viscosity	.05
viscAhGridMax	maximum grid-dependent lateral eddy viscosity	1
tracForcingOutAB	≈ 1, take T, S, p, Tr Forcing out of Adams-bash.	1
noslipsides	no slip sides on/off flag	False
noslipbottom	no slip sides on/off flag	False
useJamartWetPoints	coriolis wetpoints method flag	True
useJamartMomAdv	V.I, non-linear terms Jamart flag	True
implicitDiffusion	implicit diffusion	True
implicitViscosity	implicit viscosity	True
bottomDragQuadratic	vertical viscosity coefficient	2.1e-3
momDissip-In-AB	damping terms inside Adams-Bashforth scheme	False
temp/saltAdvScheme	temperature/salinity advection scheme	7
vectorInvariant Momentum	vector invariant momemtum	True

gcm from Losch (2008). MITgcm incorporates the 3-equation thermodynamic formulae to describe fluxes of heat, salt, and freshwater at the ice shelf-ocean interface. The equations to describe the freezing and melting at the ice-ocean boundary layer are shown as follows:

$$\underbrace{c_p \rho \gamma_T (T - T_b)}_{\text{Heat transfer from ocean to ice-ocean boundary layer}} + \underbrace{\rho_I c_{p,I} \kappa \frac{(T_S - T_b)}{h}}_{\text{Diffusive heat flux into ice}} = \underbrace{-Lq}_{\text{Latent heat of fusion}} , \tag{3.3a}$$

$$\underbrace{T_f = (0.0901 - 0.0575\, S_b)^\circ - 7.61 \times 10^{-4} \frac{\mathrm{K}}{\mathrm{dBar}}\, p_b,}_{\text{Freezing temperature}} \tag{3.3b}$$

$$\underbrace{\rho \gamma_S (S - S_b)}_{\text{Diffusive salt flux into ice-ocean boundary layer}} = \underbrace{-q\,(S_b - S_I)}_{\text{Change in salinity due to freezing/melting}} . \tag{3.3c}$$

Equation (3.3a) describes the heat balance at the ice-ocean boundary layer, equation (3.3b) represents the freezing temperature, and equation (3.3c) represents the diffusive heat flux into ice-ocean boundary layer. In these equations, C_p is the specific heat capacity of water, γ_T is the turbulent exchange coefficient of temperature, L is the latent heat of fusion, κ is the heat diffusivity through the ice shelf, and q is the freshwater flux due to melting.

Within the ice shelf cavities, the partial grid-cell treatment of topography in "z" coordinates ensures that the ice shelf cavities maintain an accurate topography (Losch, 2008). Exchange of basal ice shelf heat and freshwater exchange is parameters as a diffusive flux of temperature and salinity with a constant friction velocity and turbulent exchange (Jenkins and Bombosch, 1995).

Table 3.3: Ice Shelf Parameters

Parameter	**Description**	**Value**
SHELFICEHeatCapacity$_{C_p}$	specific heat capacity (Ice)	2000.0E+00
rhoShelfIce	constant(mean density) of ice shelf	917.0E+00
SHELFICEheatTransCoeff	transfer coefficient (exchange velocity) for Temp	1.0e-4
SHELFICEthetaSurface	(constant) surface temperature above the ice shelf	-20.0E+00

Ice shelf parameters are kept at default values provided in table §3.3. These parameter values have been incorporated into several ice-shelf cavity MITgcm configurations. For instance, Dansereau, Heimbach, and Losch (2014) uses the MITgcm configuration at $\frac{1}{32}$ ° to assess both the turbulent heat and salt transfer and the melt rate patterns at the base of Pine Island glacier. However, although the WSRM also uses constant values of frictional velocity and turbulent exchange, studies suggest that values of the turbulent transfer coefficients scale with lateral velocity of the flow speed in the boundary layer adjacent to the ice (Jourdain et al., 2017).

During the WSRM configuration process, topographical adjustments addressed the issue of anomalously high concentrations of sea ice in the WSRM, particularly in the southwest Weddell. To fix this issue, we removed isolated wet gridcells and 'inlets' along the coast of the model domain. These areas acted to "trap" ice and prevent ice advection away from the coast. A particular coastal "embayment" in the southwest Weddell Sea was also removed that had this ice trapping effect.

3.2.5 WSRM Initial Conditions

WSRM initial conditions are derived from the Southern Ocean State Estimate (SOSE). SOSE uses the adjoint-state method of ECCO2 to develop a $\frac{1}{6}^\circ$ eddy-permitting regional reanalysis product (Mazloff, Heimbach, and Wunsch, 2010). SOSE incorporates recent observational efforts including Argo floats, satellite altimetry, and microwave and infrared radiometer observed SST into its solution. In addition, SOSE outperforms the World Ocean Atlas 2001 climatological product in terms of accurately representing the dynamic/thermodynamic Southern Ocean state compared to observations (Mazloff, Heimbach, and Wunsch, 2010). Although we are currently setting the initial conditions with SOSE data, we have experimented with initializing the WSRM with other reanalysis datasets, such as ECCO2; however, WSRM analysis using ECCO2 provided similar results to SOSE in terms of the water mass properties and the sea ice state.

Due to a lack of observations under the ice shelf cavities of Antarctica, reanalysis products lack data in these regions. To circumvent this issue in our initial conditions, we initially experimented with extrapolating SOSE data under the ice shelves. However, this extrapolation led to excessive warm temperatures and consequentially, high FRIS melt rates at the start of each simulation. The anomalously high melt rates of $\approx$ 800Gt/yr never recovered to a level of low melt($\approx$100Gt) seen in observations today (Rignot et al., 2013). This extrapolation issue also arose consistently when experimenting with other reanalysis datasets such as ECCO2.

To bypass this issue of extrapolation under ice shelves, the temperature and salinity of the ice shelf cavity is relaxed to the surface freezing temperature and to a salinity of 34.45psu for 2 years and a relaxation timescale of 30 days. If this value of the relaxed salinity is too fresh ($\approx$34psu), an anomalously high FRIS melt rate ensues since warm CDW can easily access the FRIS cavity. On the other hand, a relaxation of the FRIS cavity that is too high ($\approx$34.9psu) prevents the flushing of the cavity with either HSSW or CDW. Therefore, the 34.45psu salinity relaxation condition is implemented for our control simulation to achieve a cavity stratification that allows for both HSSW and CDW intrusion without excessive melt.

3.2.6 WSRM Sea Ice Parameterization

The MITgcm dynamic-thermodynamic sea ice model prescribes the thermodynamic-dynamic sea ice state in the WSRM. This sea ice model is a variant of the viscous-plastic (VP) dynamic sea ice model (Jinlun and Hibler, 1997). The momentum equation for the sea ice state is given by:

$$m\frac{D\vec{\mathbf{u}}}{Dt} = -mf\vec{k}\times\vec{u} + \tau_{air} + \tau_{ocean} - m\nabla\phi(0) + \vec{\mathbf{F}}. \tag{3.4}$$

In equation (3.4), $m = m_i + m_s$ is the ice and snow mass per unit area, $\vec{\mathbf{u}} = u\vec{\mathbf{i}} + v\vec{\mathbf{j}}$ is the ice velocity vector, $\vec{\tau}_{air}$ and $\vec{\tau}_{ocean}$ are the wind-ice and ocean-ice stresses, respectively, $\nabla\phi(0)$ is the gradient of the sea surface height, $\phi(0) = g\eta + p_a/\rho_0 + mg/\rho_0$ is the sea surface height potential, and $\vec{\mathbf{F}} = \nabla\cdot\sigma$ is the divergence of the internal ice stress tensor σ_{ij}.

The sea ice model is tightly coupled to the MITgcm ocean model. At every forward timestep, heat, freshwater, and surface fluxes are computed from the ocean model and modified by the sea ice model (Losch et al., 2010). In terms of sea ice dynamics, sea ice motion is dictated by ice-ocean, ice-atmosphere, internal stress, and the hydrostatic pressure gradient. The sea ice internal stresses are calculated from a variant of the viscous-plastic (VP) constitutive law of Jinlun and Hibler (1997), while sea ice momentum in equation (3.4) and the solution via line successive over-relaxation (LSOR) is described in Zhang and Hibler (1997). For the thermodynamic sea ice component, upward conductive heat flux through the ice is parameterized assuming a constant sea ice conductivity that depends on ice thickness and assumes a linear temperature gradient through the ice (Semtner, 1976). Snow on top of sea ice modifies the heat flux as well as the sea ice albedo (Losch et al., 2010).

The 7th order one step method is chosen for WSRM advection of ice thickness, snow thickness, and ice salinity in the WSRM to be consistent with the tracer advection scheme (see table 3.1). "Free-slip" sea ice boundary conditions are prescribed to mimic the sea ice state setup in the llc4320 ECCO2 sea ice setup (Rocha et al., 2016).

In terms of the various sea ice parameters, the WSRM sea-ice model parameters are chosen to comply with values provided in literature and from observations as best as possible. For instance, the sea ice drag coefficient is modified to a value of .002 based on observations from Andreas (1995). If ambiguous, sea ice parameters are chosen based on similar model sea ice state setups

Table 3.4: Sea Ice Parameters

Parameter	Description	Value
SEAICEdryICEAlb	winter albedo	0.8783
SEAICEwetIceAlb	summer albedo	0.7869
SEAICEwetSnowAlb	wet snow albedo	0.8216
SEAICEdrySnowAlb	dry snow albedo	0.9482
SEAICEdrag	air-ice drag coefficient	.002
HO	demarcation ice thickness	.1
SEAICEnoslip	no slip conditions	false
SEAICEareareg	min. concentration to regularize ice thickness	.15
SEAICEhicereg	min. ice thickness for regulation	.1

including the sea ice model parameters of SOSE and ECCO2 llc4320 (Rocha et al., 2016) (see Table §3.4). The availability of the SOSE and the ECCO2 llc4320 (Rocha et al., 2016) sea ice input parameters simplified the sea ice model set-up.

MITgcm parameterizes frazil in a separate package from sea ice. Frazil forms in the Weddell Sea region as an effect of melting on the base of the FRIS cavity. In reality, as meltwater rises from the base of the ice shelf towards the surface water, it is supercooled as the freezing point rises with decreasing pressure. At the same time, a phase change occurs due to the pressure decrease, and disc-shaped frazil crystals form (Jenkins and Bombosch, 1995). MITgcm accounts for the formation of frazil ice by collecting negative heat below the freezing point at depth and immediately bringing it to the surface. This mechanism by which MITgcm accounts for frazil led to an enormous negative heat anomaly in a small amount of gridcells at the base of the ice shelf. Unfortunately, the frazil package is poorly designed for the FRIS region, and more broadly, for any water beneath an ice shelf. Consequently, we removed the frazil package from our model setup. Consequently, temperature anomalies below the local freezing temperature may be mixed into ambient waters in neighboring gridcells before reaching the surface.

3.2.7 WSRM Boundary Conditions

Open boundaries are prescribed at the WSRM northern and eastern boundaries where the Weddell Sea circulation is not blocked by topography. Boundary fields are prescribed from a repeating, year-long monthly climatology from SOSE. The boundary contains a sponge layer that extends approximately 200km into the model interior, with an inner relaxation timescale of 10 days and an outer relaxation scale of half a day. The forced ocean fields include temperature, salinity, zonal, and meridional velocity. Aside from the ocean state, sea ice fields are forced at the boundary in terms of sea ice thickness, area, salinity, and the zonal and meridional velocities. We validate the sea ice state against NSIDC satellite data, which we discuss in §3.4.

At the model's eastern boundary, we modify the open boundary condition to account for missing SOSE data in areas that are predominately ice-shelf covered. Specifically, the boundary salinity and temperature are set to 34.45psu and the local surface freezing temperature, respectively, along the eastern boundary where the ocean depth is less than 400m. In addition, the minimum salinity is set to 34.15psu at both the northern and eastern boundaries to account for anomalously fresh salinity at the boundaries. As give in table 3.2, no-flux conditions are prescribed at the closed boundaries, where the velocity at the wall of the boundary is not slowed by friction.

Ten tidal phases and amplitudes, the M_2, S_2, N_2, K_2, K_1, O_1, P_1, Q_1, M_f, and M_m tides, are prescribed at the boundaries and derived from the Circum-Antarctic Tidal Solution (CATS) 2008b (Padman et al., 2002). The CATS solution is a regional dynamic model of the Southern Ocean, optimized from a forward model solution that is forced at the boundaries with the global tidal TPX07.1 'inverse' model. The inverse model implements data assimilation, allowing CATS to accurately predict tidal phases and relative amplitudes. CATS has been validated against Synthetic Aperture Radar (SAR) interferograms from the front of the Ronne and Filchner ice shelves, and the error between the differential height signal in the DSIs and the CATs model was around 10 cm (Padman et al., 2002). Future improvements to CATS require improved understanding of ice-shelf grounding lines and ice shelf cavity water column water thicknesses. In the southeastern

Table 3.5: Boundary Condition Parameters

Parameter	Description	Value
useOBCStides	use tides on open boundaries	True
useOrlanskiNorth	use orlanski boundary conditions	False
useOBCSsponge	use sponge layer on open boundaries	True
useOBCSbalance	barotropic inflow/outflow for mass cons.	True
OBCSbalanceFacN	barotropic inflow/outflow on N. bound.	0
OBCSbalanceFacE	barotropic inflow/outflow on E. bound.	1
spongethickness	thickness of sponge layer	20
UrelaxOBCSinner	relax. time scale at innermost sponge layer point of a meridional OB	864000
UrelaxOBCSbound	relax. time scale at outermost sponge layer point of a meridional OB	43200
VrelaxOBCSinner	relax. time scale at innermost sponge layer point of a zonal OB	864000
VrelaxOBCSouter	relax. time scale at outermost sponge layer point of a zonal OB	43200

Weddell Sea, the tidal critical latitude and critical slope are co-located, leading to turbulent mixing (Fer, Darelius, and Daae, 2016). Observations suggest that the semidiurnal tide is trapped along the slope near the critical latitude and dissipates its energy in the $\mathscr{O}$(100m) thick benthic layer $\mathscr{O}$(10km) across the slope. This turbulence may have effects on the warm inflow onto the shelf and the dense outflow of bottom waters.

3.2.8 WSRM Atmospheric Forcing

The atmospheric WSRM state is forced from a 9-year repeating daily-averaged atmospheric forcing dataset that includes 10m zonal and meridional winds, 2m atmospheric temperature, pressure, longwave and shortwave radiation, precipitation, and humidity. MITgcm uses bulk formulae to convert the atmospheric fields to surface fluxes by calculating air-ice and air-ocean fluxes of heat, freshwater, and momentum at every timestep. We list key external forcing parameters in table 3.6. We choose to derive the atmospheric forcing from the Antarctic Mesoscale Prediction System (AMPS) (Powers et al., 2003b). The AMPS data is available in a 3-hourly output and spans the years 2007–2015, increasing in resolution from 20 to 10 km over the time period. Originally, we tried to incorporate the full 3-hourly 9-year AMPS dataset in the WSRM surface forcing. However, due to the high synoptic variability of the AMPS data, the model developed numerical instabilities. Using the full 3-hourly forcing would have severely reduced the allowable timestep.

AMPS was chosen over other reanalysis products as it provides a tool to generate fine-scale, consistent regional-scale fields using the high-resolution regional Polar Weather Research and Forecasting Model (WRF) (Deb et al., 2016). In general, high spatial variability and complex orography create difficulties in the ability of global reanalysis tools and climate models to capture large Antarctic regional variability in temperature, wind and precipitation. However, AMPS data has been shown to be comparable to observations over West Antarctica (Deb et al., 2016) and Ice Station Weddell (Tastula, Vihma, and Andreas, 2012). For experimentation purposes, WSRM simulations were performed forced with ERA-Interim data as an alternative surface forcing dataset to AMPS. However, these experiments did not produce discernibly different results in terms of FRIS water mass properties, melt rate, and circulation.

3.3 WSRM Simulation Procedure

The WSRM is currently running at $\frac{1}{3}$ $^\circ$ resolution and at a forward timestep of 480 seconds. As mentioned in §3.1, we aim to eventually refine the model to an eddy-permitting $\mathscr{O}$1km resolution. Model runs are initialized with a 2-year period described in §3.2.7 where the FRIS ice shelf cavity is restored on a 30-day timescale to the local surface freezing temperature and to a salinity of 34.45psu. Shown in fig. 3.1 is a 3-D visualization of the WSRM domain, including the FRIS. Note that the domain faces southward towards the ice shelf cavity for ease of viewing the FRIS cavity.

In the following sections, the water mass properties, circulation, the basal melt rate of the WSRM are analyzed before validation against observations. WSRM diagnostics are averaged over

Table 3.6: External Forcing Parameters

Parameter	Description	Value
exfalbedo	albedo for computing radiative fluxes	.15
exfscale bulkCdn	scaling of neutral drag coefficient	1.015
UseRelativeWind	subtract [U/V]VEL or [U/VICE from U/V]WIND before computing [U/V]STRESS	True
repeatPeriod	cycle through inputs at the same period	283996800s
apressurestartdate1	start time (YYYYMMDD)	20070101
apressureperiod	interval between records	86400
aqhstartdate1	start time (YYYYMMDD)	20070101
aqhperiod	interval between records	86400
vwindstartdate1	start Time (YYYYMMDD)	20070101
vwindperiod	interval between records	86400
uwindstartdate	start Time (YYYYMMDD)	
uwindperiod	interval between records	86400
precipstartdate	start Time (YYYYMMDD)	
precipperiod	interval between records	86400
swdownstartdate1	start Time (YYYYMMDD)	
swdownperiod	interval between records	86400
atempstartdate1	start Time (YYYYMMDD)	
atempperiod	interval between records	86400

the last full 9-year cycle (years 19–27) that corresponds to a complete atmospheric forcing cycle in the WSRM (see §3.2.8).

3.3.1 Circulation

The barotropic streamfunction over the WSRM domain is plotted in fig. 3.2. Fig. 3.2 shows that circulation in the WSRM follows bathymetric contours and stays largely out of the FRIS cavity. A

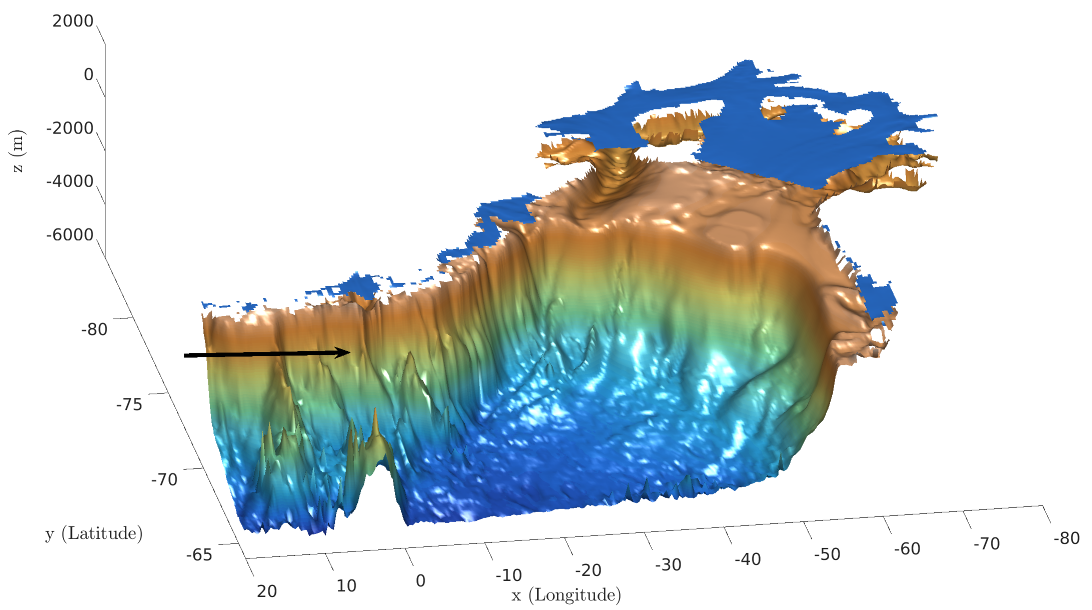

Figure 3.1: Visualization of the WSRM domain, which includes the adjacent FRIS. Bathymetry is plotted and colored by depth. Ice shelf elevation is overlaid in blue over open ocean gridcells. The black arrow denotes the pathway of the ASF.

closer analysis of the barotropic stream function within the FRIS cavity is shown in fig. 3.3. Our model circulation follows pathways described by Nicholls et al. (2009) and Darelius et al. (2014) that are seen in observations. The ASC splits around the Brunt Ice Shelf and forms a southward flow, while the initial current continues to flow westward (Darelius et al., 2014). As HSSW comes into contact with surrounding ice, it is supercooled at depth and is transformed into ISW. Some of this ISW exits the FD on the eastern flank, while water that is too dense flows cyclonically within the cavity. Overall, the circulation in the WSRM presented in fig. 3.2 suggests that the WSRM is capable of simulating the large-scale processes necessary for dense water production and deepwater formation.

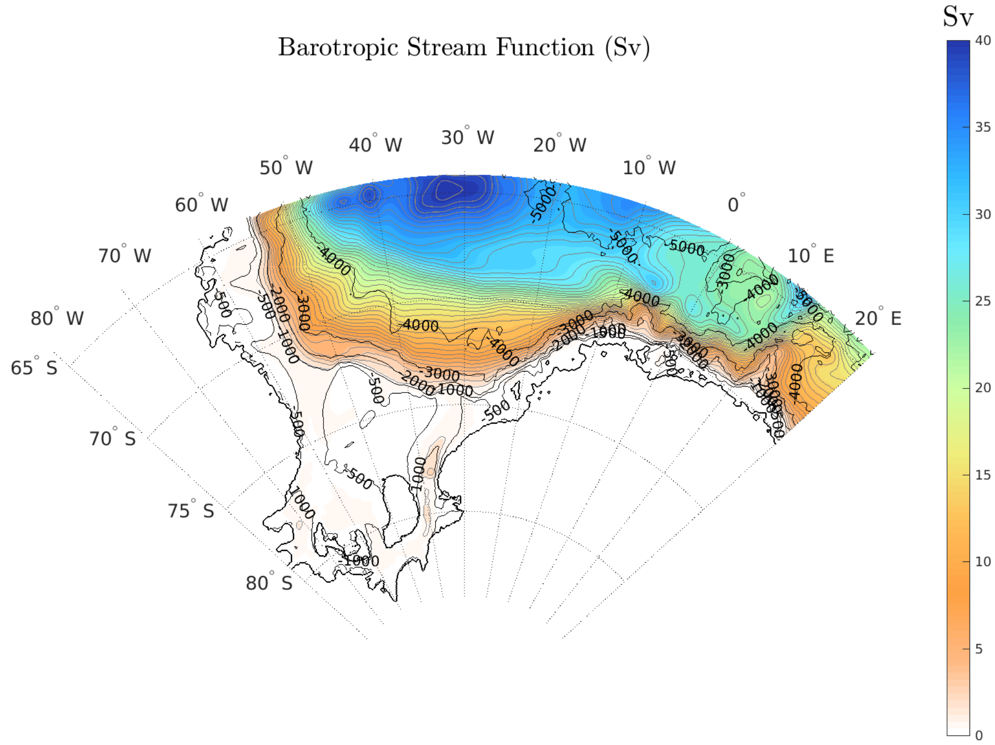

Figure 3.2: Barotropic streamfunction (Sv) in the WSRM control simulation. Values are averaged over the last 9-year complete atmospheric forcing period in the reference simulation (years 19–27). Overlaid contours in gray refer to streamlines spaced at .5 Sv. Contours in black refer to bathymetry and are spaced at 1000m.

3.3.2 Shelf Ice Melt Rate

The time-series of the integrated FRIS melt in the WSRM reference simulation is given in fig. 3.5. For the first two years, as the FRIS cavity is restored to the surface freezing temperature, the FRIS cavity exists in a relatively "high" melt regime. After the two-year relaxation period, the model adjusts to a stable melt rate of $\approx$ 100 Gt/yr as shown in fig. 3.5. The WSRM integrated melt rate is comparable to observational estimates of 155Gt/yr (Rignot et al., 2013). Although mCDW has access to the FRIS cavity and minor re-circulation pathways are evident in the Filchner Trough region in fig. 3.3, cold mid-depth FRIS cavity temperatures persist in the cavity shown in fig. 3.6

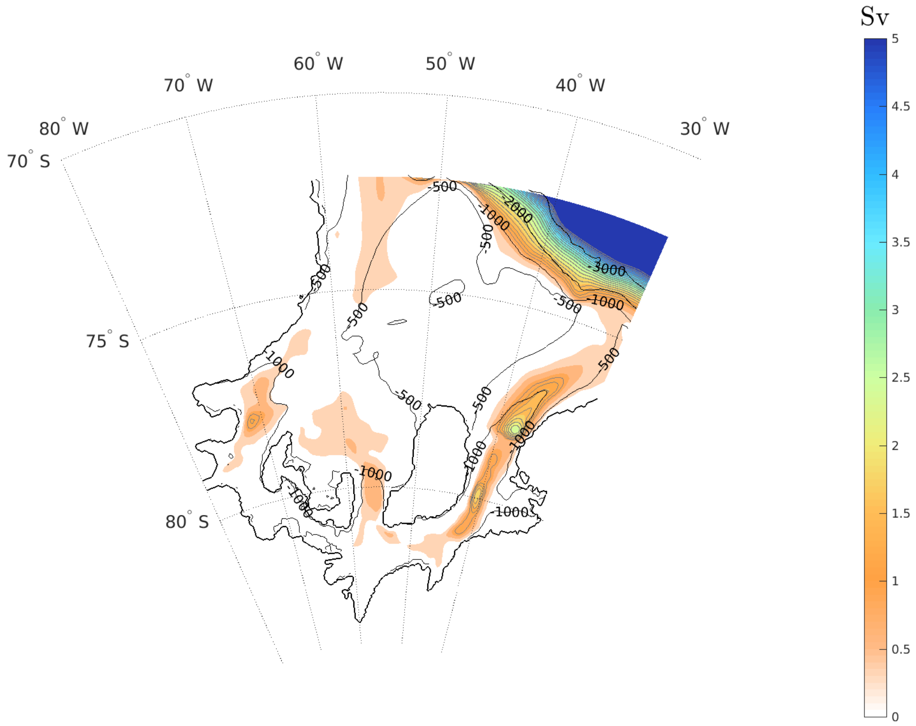

Figure 3.3: Barotropic streamfunction (Sv) of the FRIS cavity in the WSRM control simulation. Values are averaged over the last 9-year complete atmospheric forcing period in the reference simulation (years 19–27). Overlaid contours in gray refer to streamlines spaced at .2 Sv. Contours in black refer to bathymetry and are spaced at 1000m.

without anomalously high melt rates.

The initial cavity stratification, which is a function of the 2-year restoring period prevents mCDW from flooding the FRIS cavity. Dense ISW formation within the cavity within the Filchner Trough region (Foldvik et al., 2004) has been shown to prevent the inflow of warmer offshore water masses (Hellmer, 2004; Hellmer et al., 2012). We plot a map of the melt rate over the model shelf ice in fig. 3.4. Note that the melt is focused in the back-end of the FRIS cavity, which is consistent with observed patterns of melt concentrated towards grounding lines of major ice streams (Moholdt, Padman, and Fricker, 2014).

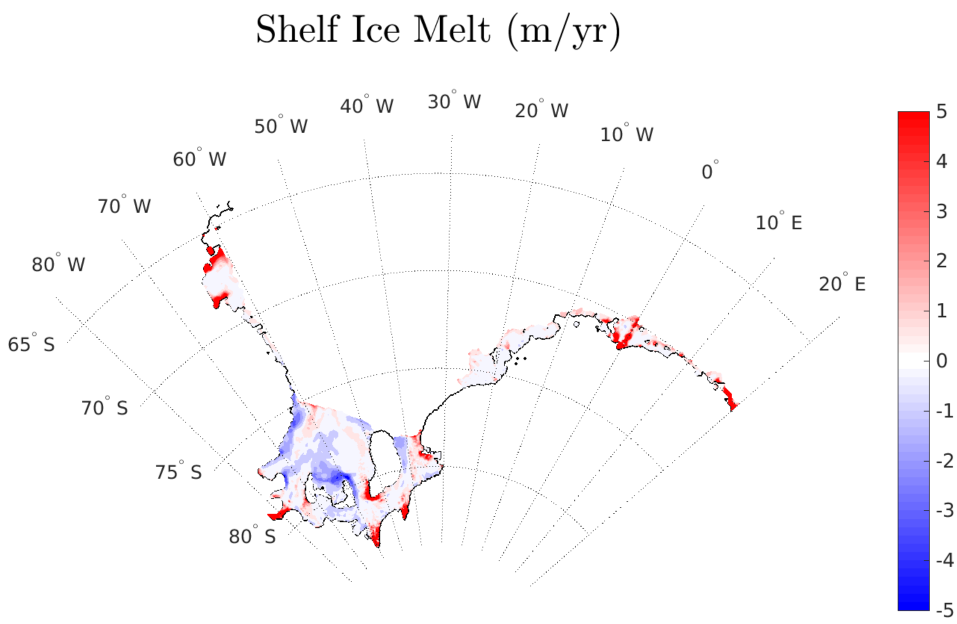

Figure 3.4: Shelf Ice Melt (m/yr) in the WSRM control simulation. Values are averaged over the last 9-year complete atmospheric forcing period (years 19–27).

3.3.3 Water Mass Properties

Water mass properties within the WSRM are shown in a temperature/salinity (T/S) plot in fig. 3.7. Plotted are water mass properties are seasonally averaged over JJA in order to capture the strongest signal of HSSW (Gordon, Huber, and Busecke, 2015). Compared to observations from Nicholls et al. (2009), the T/S plot in fig. 3.7 shows that the WSRM control simulation represents all major water masses of the Weddell. However, although a minor amount of HSSW exists at values near 34.7psu as seen in Nicholls et al. (2009), the WSRM HSSW is biased fresh compared to observations. This fresh anomaly in the WSRM may be a bi-product of a lower-resolution simulation. Finer horizontal resolution would allow ice to respond to more localized atmospheric and oceanic forcing and resolve smaller-scale polynyas and cracks in the ice (Newsom et al., 2016). Another possibility for the fresh HSSW anomaly is that meridional winds derived from AMPS may be under-resolved, especially in regions along the coast with steep orography (Bintanja et al., 2014). In addition to representing the Weddell water masses in fig. 3.7, the T/S plot displays the observed

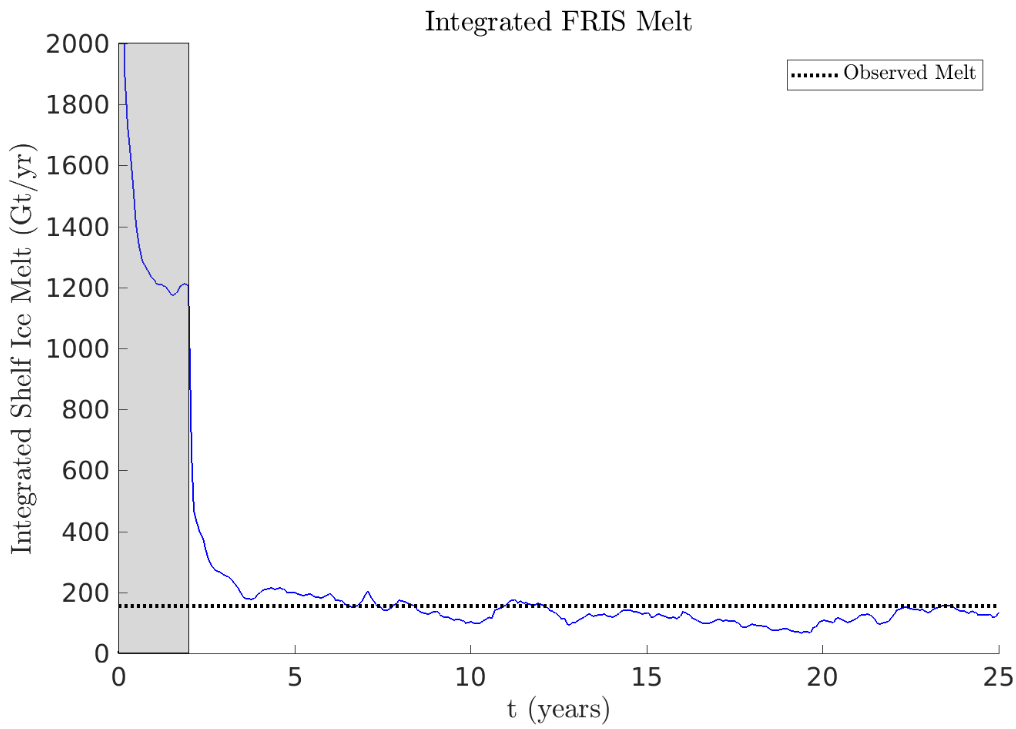

Figure 3.5: Integrated shelf ice melt (Gt/yr) from the control WSRM simulation. The dotted black line represents the 155 Gt/yr observed FRIS melt rate (Rignot et al., 2013). The shaded gray region marks the 2-year restoring period of FRIS cavity initial conditions to a salinity of 34.45psu and to the surface freezing temperature.

gade line (Gade, 1979) which depicts ice-ocean heat exchange in the cavity.

3.4 WSRM Validation

In this section, the control WSRM simulation is validated against available data from observations. Relatively few observations are available within the Weddell and the FRIS cavity due to Antarctica's vastness, remoteness, and year-round ice cover; however, improvements to observational efforts, including the employment of bore-holes to drill into ice shelves (Kobs et al., 2014), are continuously being developed. We make use of available Conductivity Temperature Depth (CTD) measurements, open-water SSH satellite estimates, and satellite Antarctic ice concentration data from satellite observations for validation purposes.

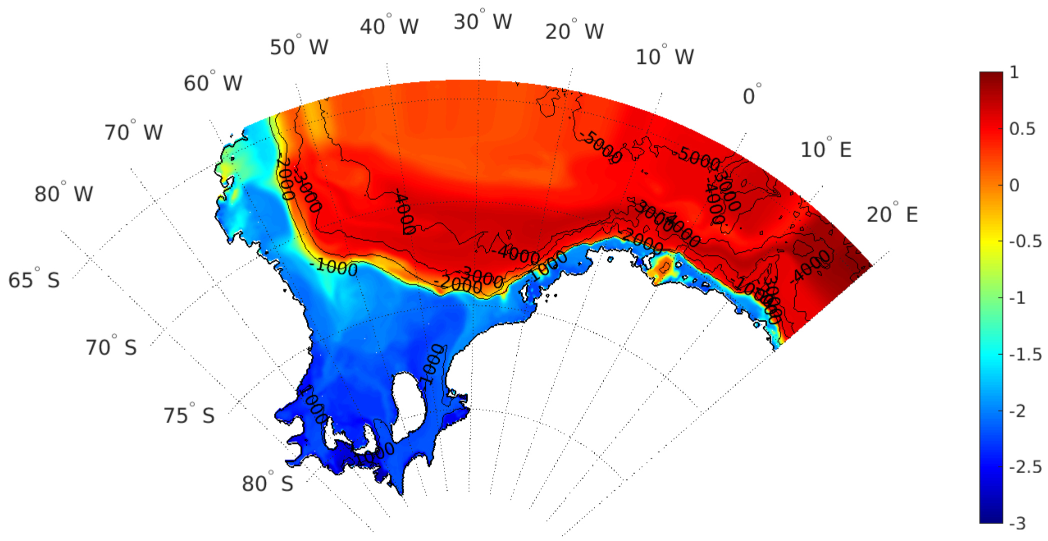

Figure 3.6: Potential Temperature (°C), plotted at a 500m depth seaward of 1000m and at mid-depth poleward of the 1000m contour. Overlaid black contours represent bathymetry and are spaced at 1000m. Plotted values represent averages from the last 9-year complete atmospheric forcing period (years 19–27).

3.4.1 WOCE CTD Sections

Two sections of the World Ocean Circulation Experiment (WOCE) (Schlitzer, 2002) contain CTD sections roughly along the northern and eastern regional WSRM boundaries. The locations of the A12 and SR4 ship tracks are shown for reference in the Supporting Information in fig. 6.2. We incorporate the mean A12 and SR4 repeat WOCE-section data into the WSRM validation. Along these paths, individual CTD profiles sample temperature, salinity, and pressure data. The first of the WOCE sections to which we compare our WSRM results is the SR4 track. The WOCE SR4 track lies approximately along the ~64°S latitude line and spans the width of the Weddell gyre, which roughly coincides with the WSRM northern boundary. To compare the WSRM diagnostics with the observations from SR4, we interpolate the observed data onto the WSRM vertical grid. WSRM data is then interpolated onto the respective "stations" of the SR4 data in an attempt to reproduce the exact locations of the CTD transect as closely as possible. Data from SR4 that lies

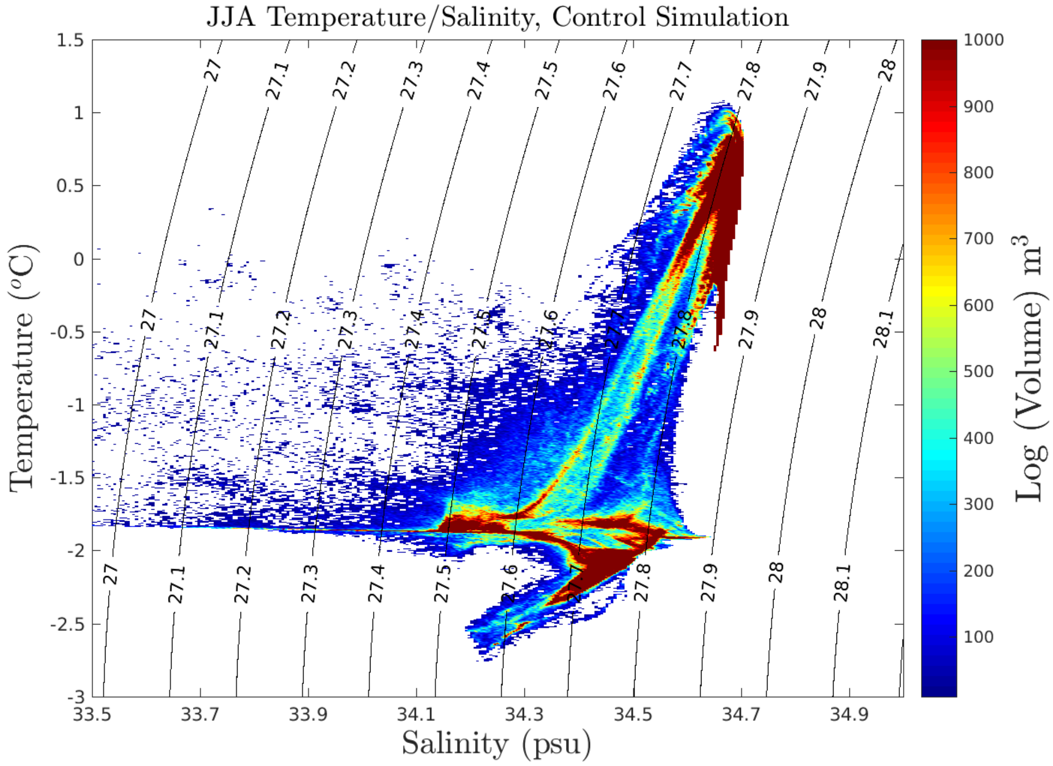

Figure 3.7: Winter (JJA) Temperature/Salinity properties of the control WSRM simulation. Data is taken from the full model domain and averaged over the last nine years of a complete atmospheric forcing cycle (years 19–27). Values are binned by volume (log scale). Potential density is contoured and spaced at values of .1kgm^3.

on or north of the model northern boundary is neglected to avoid spurious interference from the WSRM boundary conditions.

Monthly mean temperature and salinity from the reference WSRM simulation are interpolated to the SR4 section locations and plotted in the left-hand panels fig. 3.8. The mean WSRM temperature and salinity cross-sections at SR4 locations show the presence of cold, fresher surface water (AASW) and warmer, saltier underlying water (CDW). The bottom panels of fig. 3.8 reveal the difference between the individual CTD profiles and the WSRM results along the SR4 track. The anomalies show a weaker pycnocline in the WSRM compared to observations, with warm anomalies at 100-200m. We hypothesize that the ASF in the WSRM is weaker than in observations,

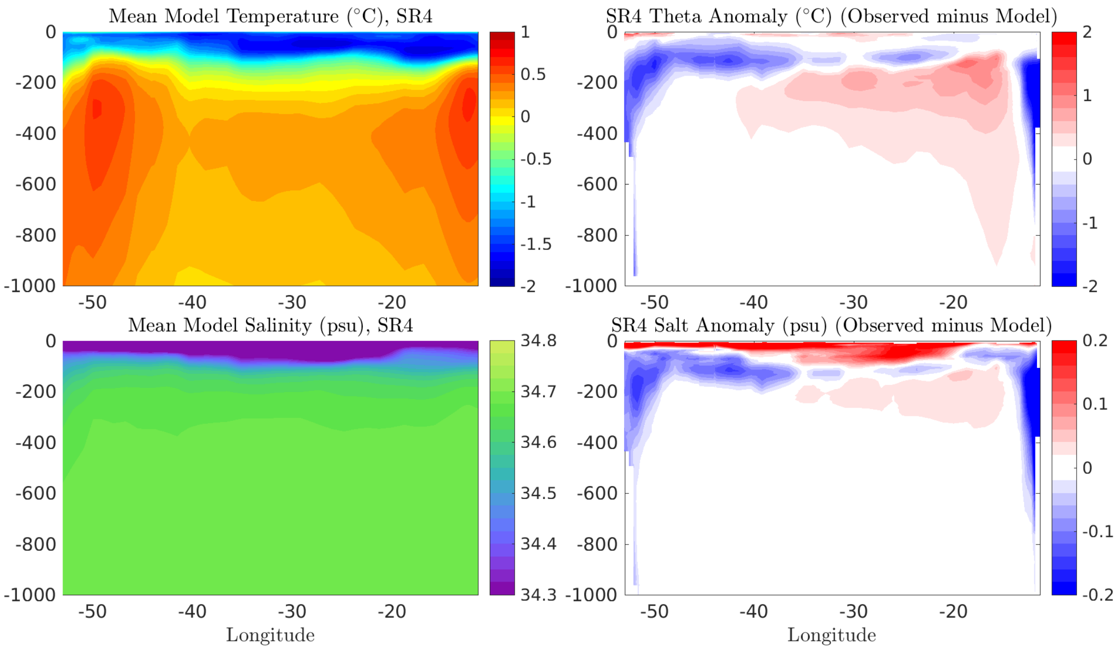

Figure 3.8: Mean WSRM temperature (°C), temperature anomaly (°C), mean WSRM salinity (psu), and salinity anomaly (psu) at the SR4 hydrographic track. Model data is extracted from the control WSRM simulation and averaged over the last 9-year full WSRM atmospheric forcing period (years 19–27). Anomaly values are calculated from observed data minus WSRM data. The location of the SR4 section is shown for reference in the Supporting Information in fig. 6.2.

which may allow greater access of warm CDW at shallower depths (Jacobs, 1991).

In addition to validation from the SR4 track, we validate the WSRM at the A12 WOCE section. The A12 WOCE section lies roughly along the (∼0°) longitude line and spans from Cape Town to the Antarctic shelf (Schlitzer, 2002). To validate the WSRM results, the same approach to the interpolation of WSRM and observational data is performed as done with the SR4 section. The mean WSRM temperature and salinity at the A12 transect is given in the left panels of fig. 3.9. Fig. 3.8 shows the simulated ASF in the WSRM and the pycnocline that tilts down towards the shelf, which is a barrier between cold AASW and warmer, saltier CDW beneath (Jacobs, 1991).

WSRM temperature and salinity properties are compared directly to observations at the WOCE A12 CTD track in the right panels of fig. 3.9. A warm bias in the in the WSRM upper ocean

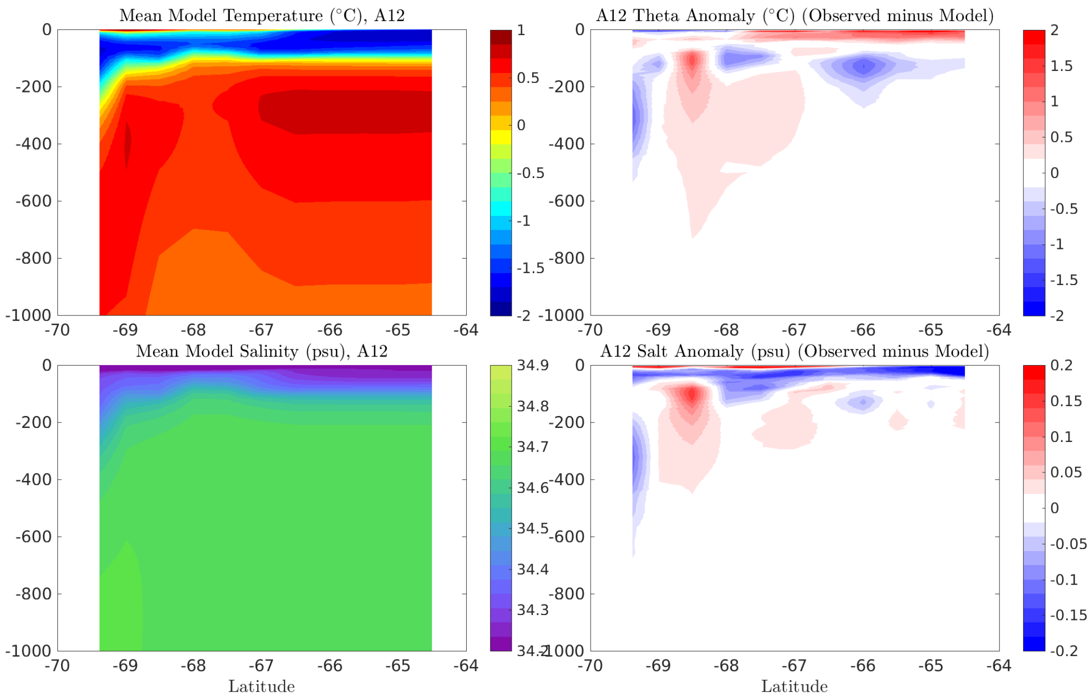

Figure 3.9: Mean WSRM temperature (°C), temperature anomaly (°C), mean WSRM salinity (psu), and salinity anomaly (psu) at the A12 hydrographic track. Model data is extracted from the control WSRM simulation and averaged over the last 9-year full WSRM atmospheric forcing period. Anomaly values are calculated from observed data minus WSRM data. The location of the A12 section is shown for reference in the Supporting Information in fig. 6.2.

temperatures along the shelf suggests that the model pycnocline is too warm and shallow, indicating a weak ASF (Thompson et al., 2018). Higher resolution may ameliorate these errors by nature of sharper temperature and salinity gradients (Legg et al., 2009).

3.4.2 Cross-slope 17°W Section

In addition to the A12 and SR4 WOCE sections, we validate the seasonal upstream FRIS conditions with a monthly hydrography at Kapp Norvegia (KN). This hydrography at KN is a cross-section along 17°W compiled by Hattermann (2018); the location of the KN section is shown for reference in the Supporting Information in fig. 6.2. The observed data at the KN track is taken from available CTD data between 10°W and 25°W as well as data from elephant seals in the Marine Mammals

Exploring the Oceans Pole to Pole (MEOP). Although KN is located upstream of the FRIS, seasonal fresh water fluxes related to ice loss and gain along the shelf as well as the strength of the ASF upstream dictate downstream FRIS properties (Graham et al., 2013). Therefore, this 17°W monthly climatology provides a fundamental validation of the WSRM seasonal depth variability of the pycnocline at the shelf break.

In the left panels of fig. 3.10, the mean WSRM temperature is plotted at 17°W in MAM (fall) and SON (spring), respectively. Here we see the signature of the ASF with a pycnocline that extends down from 400-600m along the shelf. The variation in the depth and strength of the ASF throughout the year corresponds to shifts in wind and buoyancy forcing (Thompson et al., 2018). The anomaly in temperature during MAM and SON is given in the right panels of fig. 3.10. The anomalies in the temperature between model and observations arise mostly from the depth of the pycnocline at the shelf. The observations show a stronger pycnocline during both MAM and SON, corresponding to deeper, colder temperatures towards the shelf.

The mean WSRM salinity at KN during MAM and SON shows has a similar pattern to the temperature field in fig. 3.11. Saltier water near the surface stretches downward towards the shelf, corresponding to the cold surface water in fig. 3.10. The anomalies in the WSRM properties when compared to the KN observations suggest that the simulated pycnocline in the WSRM is weaker than in observations. To ameliorate the anomalies in the temperature and salinity fields, further experimentation can be done in altering the depth of ASF stratification set at the eastern and northern boundaries, described in §3.2.7. Overall, however, the seasonal profiles at the 17°W transect compare favorably with the observed data.

3.4.3 Sea Ice Area

We validate the WSRM sea ice state during both the austral fall (MAM) and spring (SON) seasons. Data from the National Snow and Ice data Center (NSIDC) is used for validation of the sea ice state. The NSIDC provides remote sensing sea ice area data from NASA's Earth Observing System Satellite Program that spans from 1978–2007. In order to provide a direct comparison of the sea ice data against model output, we interpolate the spherical-polar gridded monthly sea ice satellite

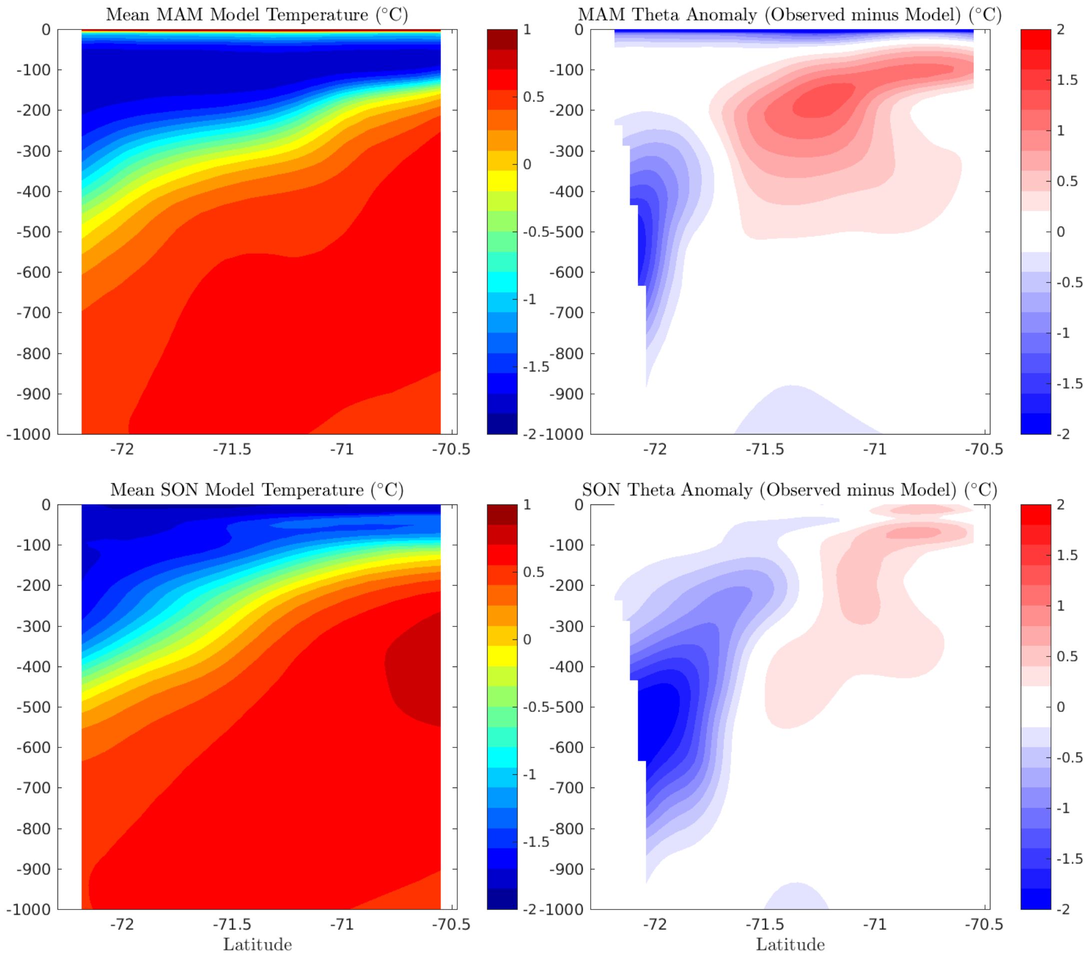

Figure 3.10: Mean WSRM temperature (°C) and temperature anomaly (°C) (observed-model) in MAM and SON at Kapp Norvegia (KN), 17W. The location of the KN transect is given in the Supporting Information in fig. 6.2. WSRM data used for validation is averaged over the last 9-year full WSRM atmospheric forcing period from the control simulation. Anomaly values are calculated from observed data minus WSRM data.

data onto our model grid and seasonally averaged. WSRM data extracted from the last 9-year full atmospheric forcing period of the reference simulation is seasonally averaged before compared to the NSIDC data.

Figs. 3.12 and 3.13 reveal the WSRM mean sea ice area coverage during MAM (autumn) and SON (spring) seasons. The MAM sea ice state in fig. 3.12 reveals that the southwest portion of the

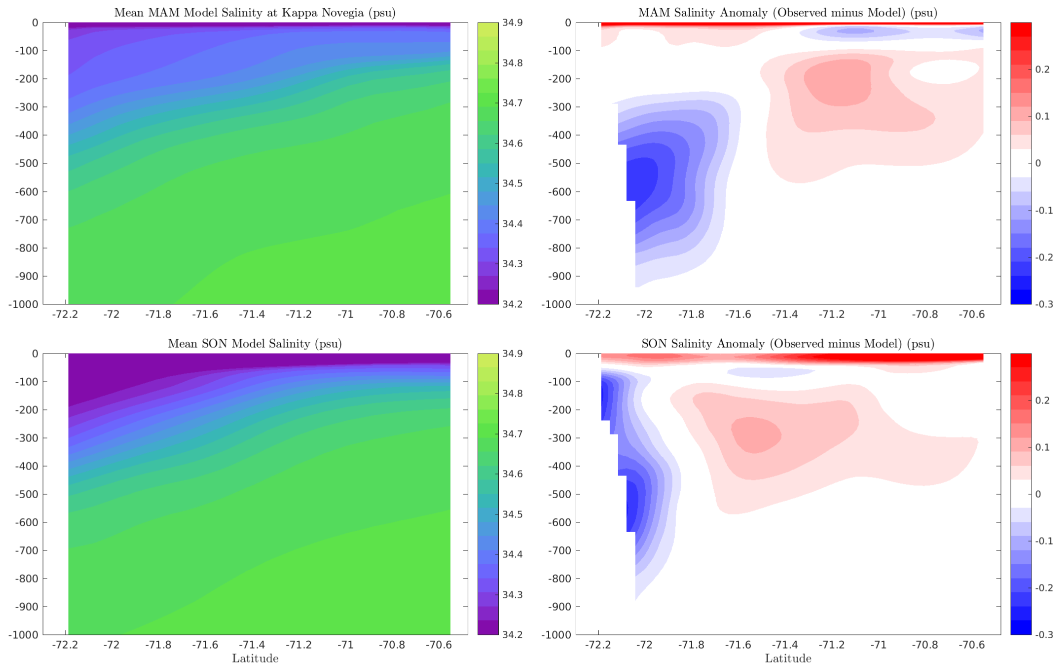

Figure 3.11: Mean WSRM salinity (psu) and salinity anomaly (psu) in MAM and SON at Kapp Norvegia (KN), 17W. The location of the KN transect is given in the Supporting Information in fig. 6.2. WSRM data from the control simulation is seasonally averaged over the last 9-year full WSRM atmospheric forcing period (years 19–27). Anomaly values are calculated from observed data minus WSRM data.

domain is predominately ice-covered but breaks in the sea ice exist the eastern model domain. In contrast, the spring (SON) sea ice state in fig. 3.13 reveals a mostly ice-covered ocean. The highest sea ice covered area lies in the southwest Weddell, while the ice pack is thinner near the eastern boundary.

The WSRM MAM and SON sea ice area anomalies are given in Figs. 3.12 and 3.13. The anomalies show that in both MAM and SON, the WSRM and the NSIDC data show largely consistent patterns of sea ice coverage. During MAM, both the WSRM and the observations have the densest sea ice area in the southwestern portion of the WSRM domain. However, a positive sea ice area anomaly exists in the in the eastern portion of the domain upstream of the FRIS. The plot showing the anomaly of the sea ice area extent in fig. 3.12 suggests an overestimation in the

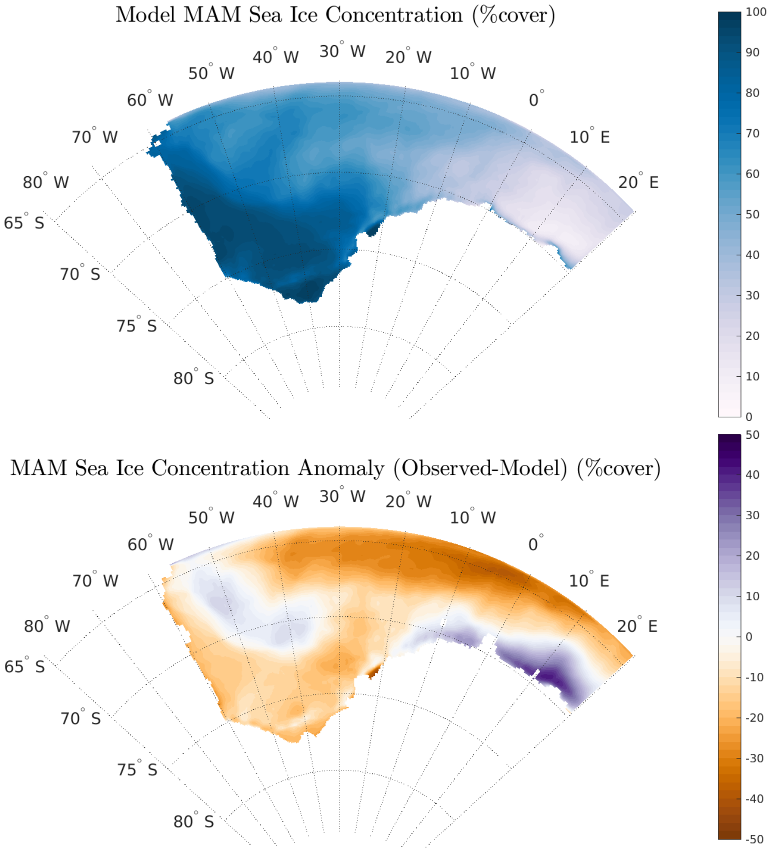

Figure 3.12: WSRM MAM Sea Ice Concentration (percent %, top) and MAM Sea Ice Concentration (percent %, bottom) compared to NSIDC data from 1978-2007. Values are seasonally averaged over the last 9-year complete WSRM atmospheric forcing period (years 19–27). Anomaly values are calculated from observed data minus WSRM data.

SOSE sea ice coverage at the boundaries. The SON sea ice anomaly in fig. 3.13 reveals a higher concentration of sea ice coverage in the WSRM compared to observations over most of the WSRM domain. This anomaly may be driven by an overestimation of the sea ice area at the boundaries. In addition, weaker offshore winds in the WSRM compared to reality may prevent ice advection away from the coast in the southwest portion of the domain.

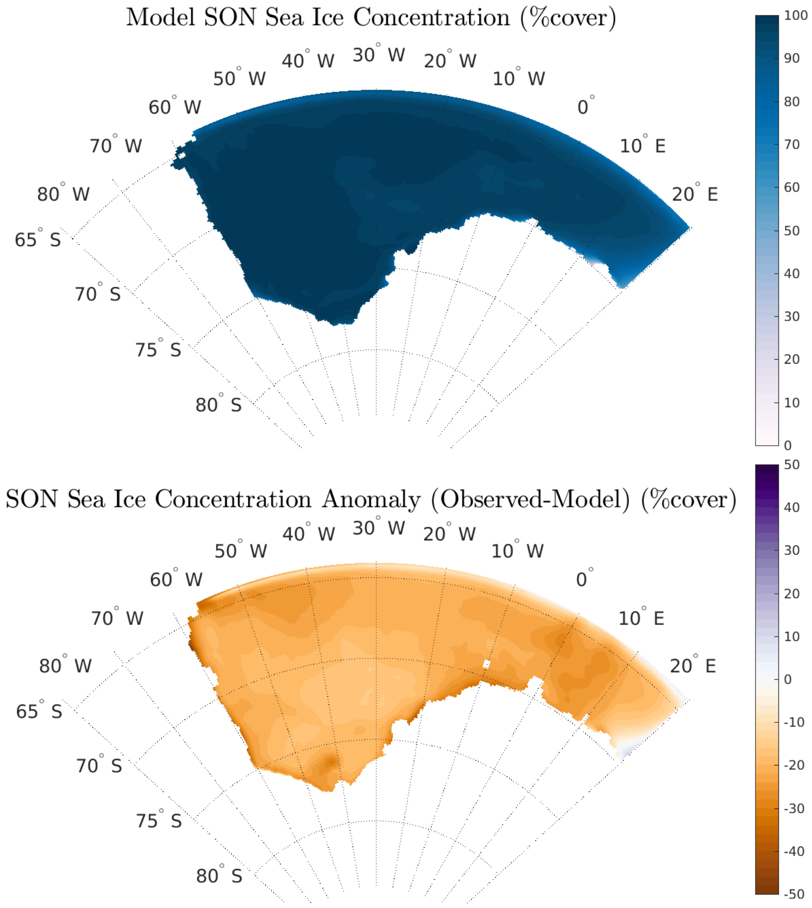

Figure 3.13: WSRM SON sea ice concentration (percent %, top) and SON sea ice concentration anomaly (percent %, bottom) validated against NSIDC data spanning 1978–2007. Values are seasonally averaged from the last 9-year complete WSRM atmospheric forcing period (years 19–27). Anomaly values are calculated from observed data minus WSRM data.

3.4.4 SSH

Southern Ocean dynamic ocean topography from the CryoSat-2 satellite (Armitage et al., 2018) is used for the purpose of validating the dynamic SSH in the WSRM. The CryoSat-2 data provides 6 years of data, spanning 2011–2016. Given that the AMPS data used in WSRM atmospheric forcing spans the years 2007–2015, we compare the CryoSat-2 SSH to the model output from the last five years of the last full cycle of AMPS surface forcing in the WSRM. The mean dynamic WSRM SSH is plotted in fig. 3.14 for reference. In this figure, contours of dynamic SSH follow streamlines from fig. 3.2. SSH is generally higher towards the coast, which we expect given that the easterly ASF leads to Ekman transport to the south towards the Antarctic continent.

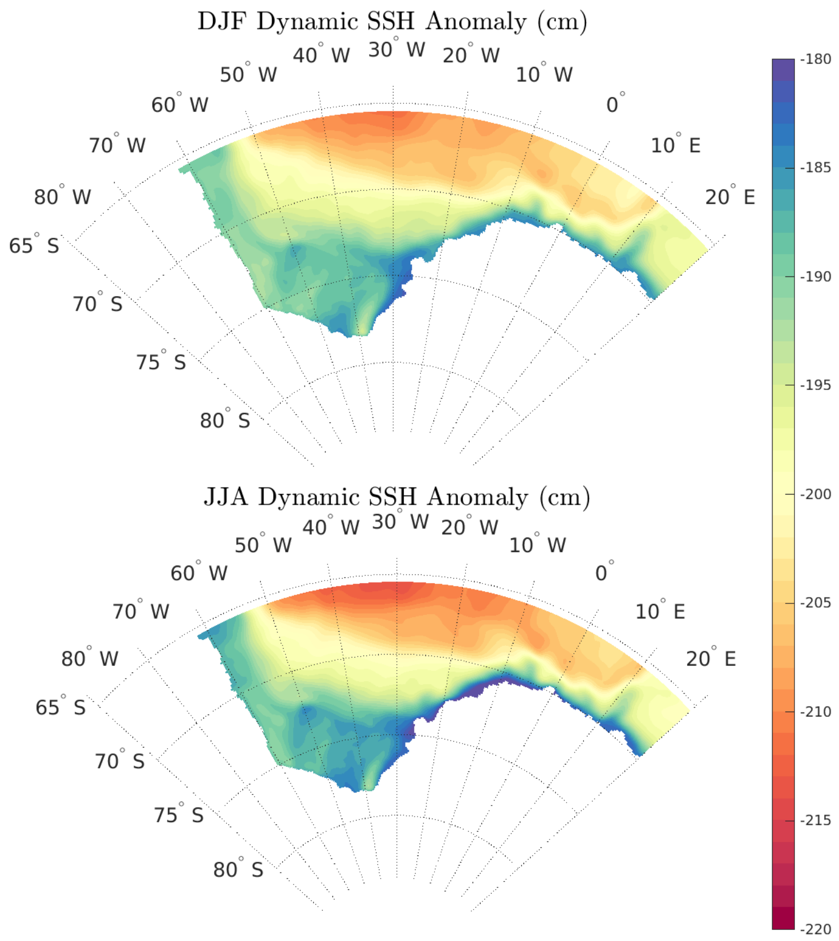

Figure 3.14: Mean WSRM DJF (top panel) and JJA (bottom) Dynamic SSH. Model data is extracted from the control WSRM simulation. Values are seasonally-averaged from the last 5-year WSRM atmospheric forcing period that matches the time period of the CryoSat-2 data.

The DJF and JJA model anomalies in the SSH in fig. 3.15 show the similarity between the WSRM and observational data, with differences in SSH of a few centimeters. In general, the SSH in the WSRM gyre is biased low, implying the WSRM has a stronger than observed gyre circulation. One location where a more pronounced anomaly exists is upstream of the FRIS, where observations have relatively lower dynamic SSH than in the WSRM. Anomalies may arise with

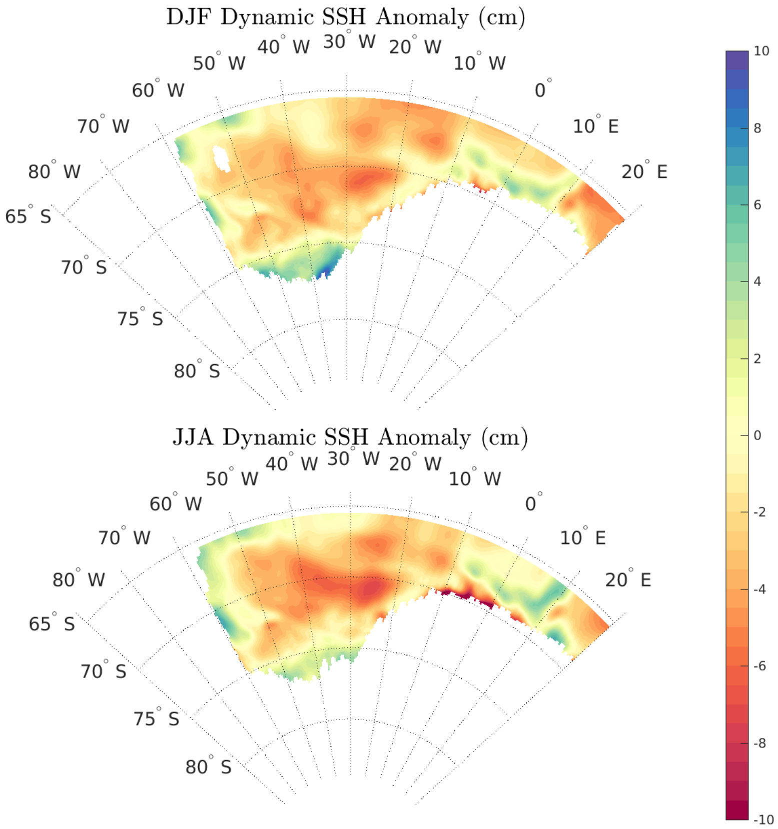

Figure 3.15: DJF (top panel) and JJA (bottom panel) Dynamic SSH Anomalies (cm), validated against CryoSat-2 data (Armitage et al., 2018). WSRM data is extracted from the control WSRM simulation. Values are averaged over the last 5-year WSRM atmospheric forcing period that matches with the CryoSat-2 data. Anomaly values are calculated from observed data minus WSRM data.

the hydrostatic pressure approximation in MITgcm where a simple pressure loading term accounts for snow and ice in the calculation of surface pressure. Overall, the SSH anomalies hint that the overall gyre circulation in the WSRM is comparable to the gyre strength in observations.

3.5 Conclusion

In this section, we describe the development of a comprehensive regional model of the Weddell Sea that includes the FRIS. The model is currently running at $\frac{1}{3}^{rd}$ degree resolution, but we plan to refine the model to an eventual resolution of $\mathscr{O}(1km)$ to resolve small-scale, high-frequency flow involved in processes such as bottom water formation and heat transport towards Antarctic ice shelves. In this chapter, the diagnostics of the control simulation of the WSRM are analyzed to understand patterns of melt rate, circulation, and water mass properties within the domain. In addition, we validate the WSRM water mass properties and sea ice state against available observations. In the next chapter, we will focus on the FRIS cavity and employ the WSRM to explore the sensitivity of FRIS cavity circulation to idealized climactic changes.

CHAPTER 4

Bi-Stability of FRIS Cavity Circulation

4.1 Motivation

The Filchner Ronne Ice Shelf (FRIS) in the southern Weddell Sea has a significant role in near-Antarctic circulation. The FRIS is Antarctica's largest floating glacier by volume (Moholdt, Padman, and Fricker, 2014), encompassing an area of roughly 450,000km^2 (Fox, Paul, and Cooper, 1994). Currently, only few remnants of CDW have been observed to cross the ASF barrier and reach the mouth of the FRIS (Darelius, Fer, and Nicholls, 2016; Nicholls et al., 2009). Several studies have explored the mechanisms that control warm water inflow onto the FRIS shelf and into the cavity. One such mechanism is from ASF instability (Klinck and Dinniman, 2010), which could disrupt the position and strength of the dynamical barrier between the shelf and underlying CDW. Other identified mechanisms include thermocline responses to wind stress and surface hydrographic properties (Hattermann et al., 2014), tidal fluctuations (Wang et al., 2013), mesoscale eddies (Stewart and Thompson, 2013), and interaction of the flow with bottom topography and troughs that cross-cut the shelf break (Daae et al., 2017; Klinck and Dinniman, 2010; St-Laurent, Klinck, and Dinniman, 2013).

Ocean models forced with atmospheric states derived from future climate projections show that CDW intrusions into the FRIS are enhanced during the coming century, leading to rapid melting of the FRIS (Hellmer et al., 2012; Hellmer et al., 2017). In these scenarios, warm water inflow travels into the Filchner Trough, which reaches 600m depth at the shelf break to 1600m at the grounding line of the FRIS (Moholdt, Padman, and Fricker, 2014). Hellmer et al. (2012) demonstrates that future climate warming may alter surface stress under ice at the continental shelf break near the Filchner Trough. This occurs as warmer atmospheric temperatures lead to less sensible heat loss and increased long-wave radiation uptake near Antarctica. Sea ice concentration is thereby reduced, and the surface stress under sea ice increases. Changes to surface stress, in turn, modify mass properties and circulation within the FRIS cavity, leading to a state of irreversible melting. The results of Hellmer et al. (2017) suggest the existence of a bi-stable FRIS cavity regime as well as the existence of a "tipping point" in atmospheric temperature, corresponding to a future shift from the current low-melt FRIS cavity state to a high-melt regime.

As discussed in §3.2.5, the WSRM initial conditions require a 2-year restoring of FRIS cavity salinity and temperature properties in order to prevent excessive CDW inflow and melt at the start of simulations. Experimentation with the WSRM initial conditions suggested that pre-existing stratification in the FRIS cavity determines whether the FRIS cavity enters a warm (high melt) state or a cold (low melt) state. As discussed in §3, the WSRM control simulation sets the initial salinity within the FRIS cavity to 34.45psu during the 2-year restoring period. With a lower initial cavity salinity (34psu), which we discuss further in this chapter, the FRIS cavity remains in a state of persistent CDW intrusion and high melt. We explore the capacity of local atmospheric conditions to initiate a "switch" between warm and cold steady states of the FRIS cavity.

Our goal is to perturb the WSRM in order to understand the relationship between changes to surface forcing and consequential shifts in the properties and circulation within the FRIS cavity. Motivated by the calculated trends in §2, we focus primarily on impacts to changes in the near-Antarctic wind forcing. Past modeling efforts have studied potential impacts to Antarctica's changing wind forcing with idealized simulations (*e.g.* Stewart and Thompson, 2012; Zhou et al., 2014; Wang et al., 2012; Daae et al., 2017). Zhou et al. (2014) attributes the seasonal deepening of the Antarctic Surface Water (AASW) layer in summer and fall near the ice shelf front in the EWS to stronger easterly winds. The downwelling depth of the AASW is enhanced with stronger winds, leading to more Ekman onshore transport beneath the ice shelves. In addition, Daae et al. (2017) claims that strong easterly winds deepen the pycnocline, which enhances the barotropic flow and are predicted to prevent southward eddy transport of warm CDW to flow onto the shelf. Near-Antarctic wind forcing has an important role in modulating the processes that co-occur in the region. The impacts to surface forcing perturbations are analyzed in terms of FRIS cavity circulation, melt rate, and FRIS cavity water mass properties.

4.2 Sensitivity of the FRIS Cavity to Pre-Existing Cavity Conditions

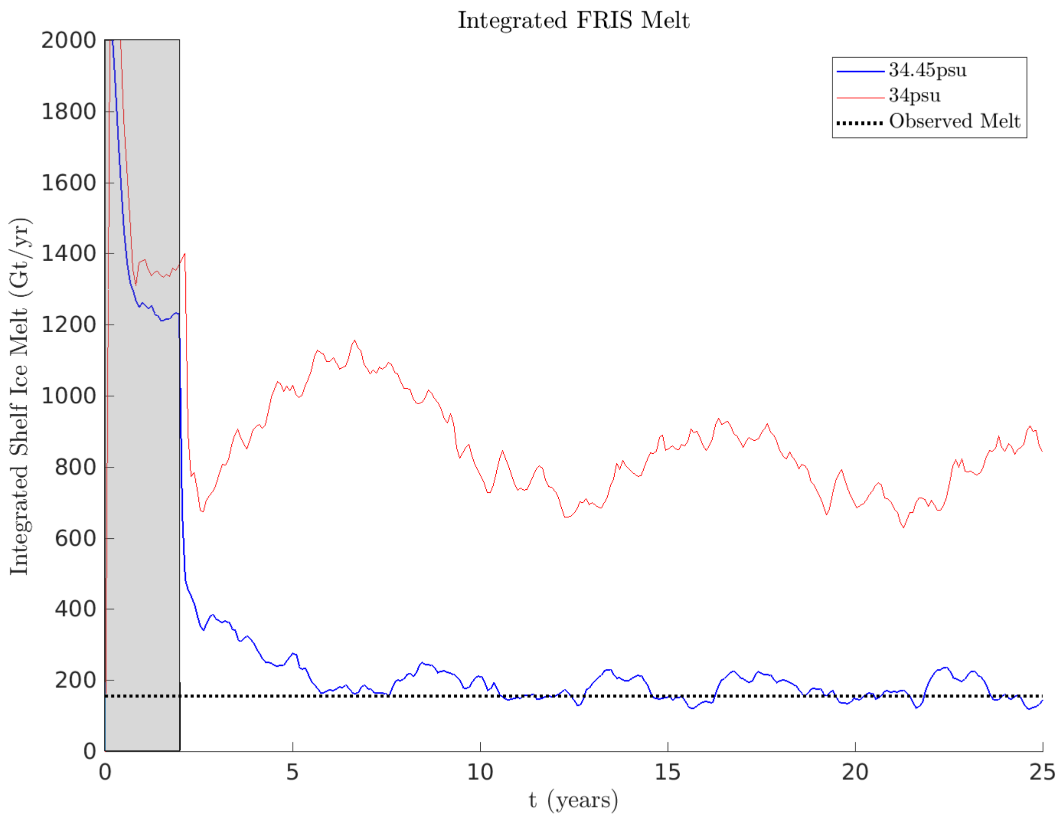

Figure 4.1: Time series of integrated shelf ice melt (Gt/yr) for the 34.45psu (blue) and 34psu (red) Initialization experiments. Shaded region corresponds to the 2-year restoring period of FRIS cavity properties to the surface freezing temperature and a salinity of 34psu or 34.45psu. The black horizontal dotted line corresponds to observed melt rate from Rignot et al. (2013).

As described in the WSRM initial conditions from §3.2.5, the WSRM FRIS cavity properties are restored on a 30-day timescale to the surface freezing temperature and to a specified salinity. This was done to avoid excessive melt at the start of WSRM simulations. Our experimental design includes two experiments with FRIS cavity restoring of the salinity to 34psu and 34.45psu, respectively. All other aspects regarding experimental setup are consistent with the description of the WSRM in §3. In addition to the 34psu and 34.45psu restoring experiments, an additional experiment was performed with a 34.9psu cavity restoring. However, the resultant density of the cavity proved too high to allow for HSSW or CDW inflow into the cavity. Therefore, we omit this case from our current analysis. A further discussion of this run is described in the Supporting Information in fig. 6.

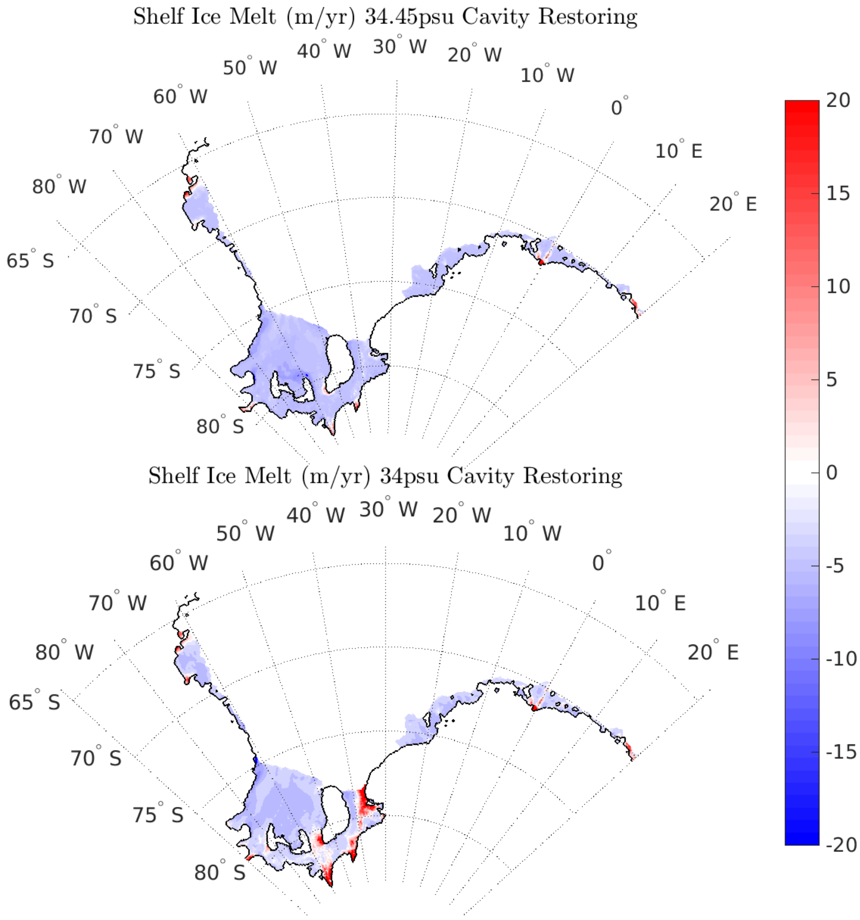

Figure 4.2: Shelf ice melt map (m/yr) for the 34.45psu (top panel) and 34psu (bottom panel) FRIS cavity restoring experiments. Values represent the monthly mean averages from the last 9-year full WSRM atmospheric forcing period in the simulations.

WSRM simulations with a FRIS cavity restoring salinity of 34psu and 34.45psu exhibit distinct FRIS cavity water mass properties, circulation patterns, and basal melt rates. First, we discuss the melt rates for the two experiments. Fig. 4.1 demonstrates that the 34psu restoring experiment maintains a basal melt rate of $\approx$ 800 Gt/yr. This melt rate never recovers to the lower melt rate of the 34.45psu cavity restoring, even after 25 years. In order to visualize the location of basal shelf ice melt, the ice shelf melt in m/yr is given in fig. 4.2 for the 34.45psu (top panel) experiment and the 34psu (bottom panel) restoring experiments. In both cases, the basal ice shelf melt is most prominent towards the back of the FRIS cavity. However, the amount of melt in the 34psu experiment is much higher while covering a larger ice shelf area than in the 34.45psu restoring experiment.

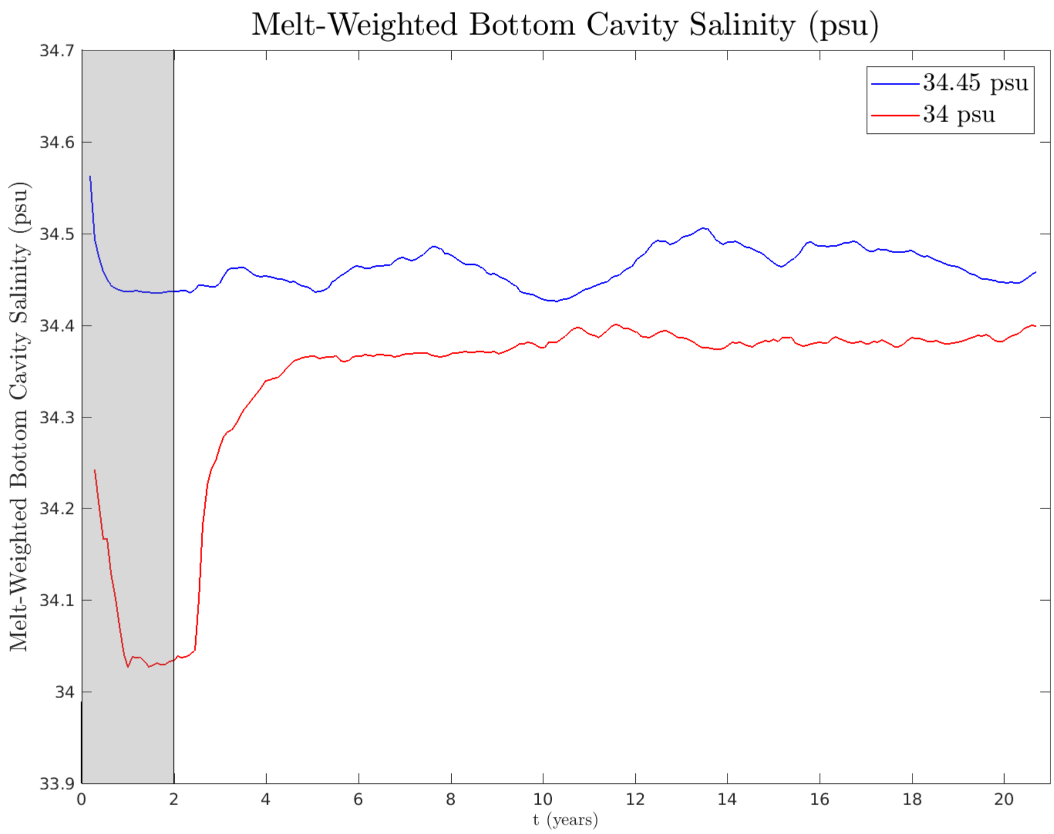

Figure 4.3: Time series of mean bottom cavity salinity (psu) for the 34.45psu (blue) and 34psu (red) initial FRIS cavity restoring experiments. The shaded region denotes the two-year restoring period of FRIS cavity properties at the start of each run. Bottom salinity values are taken from gridcells with positive melt rate and melt-weighted against the total freshwater flux in each gridcell (see equation (4.1a)).

After deducing that the 34psu and 34.45psu FRIS cavity restoring experiments exhibit distinct melt rates, we discuss the FRIS cavity properties. For clarity, we highlight the precise region of FRIS cavity analysis in fig. 6.7. Time-series plots of melt-weighted cavity salinity and temperature

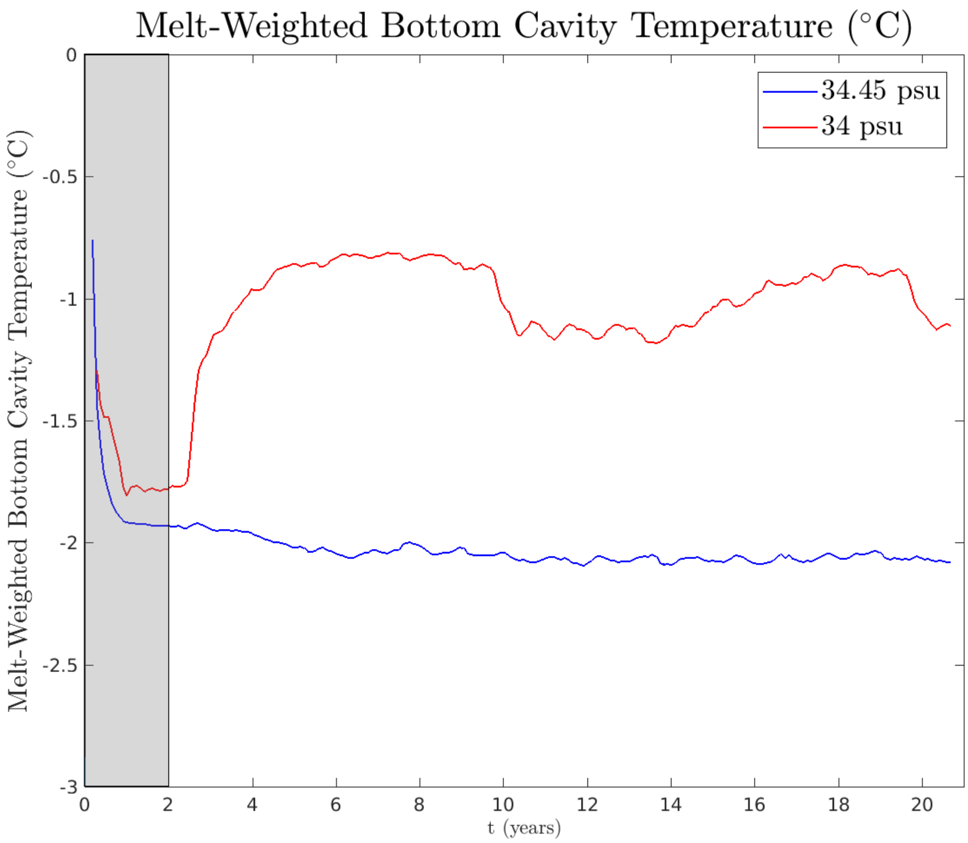

Figure 4.4: Time series of mean bottom cavity temperature (°C) for the 34.45psu (blue) and 34psu (red) initial FRIS cavity restoring experiments. The shaded region denotes the two-year restoring period of FRIS cavity properties at the start of each run. Bottom temperature values are taken from gridcells with positive melt rate and melt-weighted against the total freshwater flux in each gridcell (see equation (4.1b)).

are shown in figs. 4.4 and 4.3, respectively. Given the difference in the melt rates in the 34psu and 34.45psu restoring experiments, we assume that water mass properties of gridcells at the bottom of the FRIS cavity with the highest levels of freshwater flux are most important for this analysis. Therefore, we plot melt-weighted bottom temperature and salinity properties in the FRIS cavity from model gridcells that exhibit positive melt rates. These values have been weighted according to the total respective freshwater flux within each respective gridcell. The expressions that derive melt-weighted FRIS cavity salinity and temperature values are given as follows:

$$S_{cavity} \equiv \frac{\displaystyle\int_{\overline{F_{melt}}^t>0} \overline{S_{bottom}}^t \overline{F_{melt}}^t dA}{\displaystyle\int_{\overline{F_{melt}}^t>0} \overline{F_{melt}}^t dA}, \tag{4.1a}$$

$$T_{cavity} \equiv \frac{\displaystyle\int_{\overline{F_{melt}}^t>0} \overline{T_{bottom}}^t \overline{F_{melt}}^t dA}{\displaystyle\int_{\overline{F_{melt}}^t>0} \overline{F_{melt}}^t dA}. \tag{4.1b}$$

In these equations, we define $\overline{S_{bottom}}^t$ as the monthly-averaged bottom cavity salinity, $\overline{T_{bottom}}^t$ as the monthly-averaged bottom cavity temperature, $\overline{F_{melt}}^t$ as the monthly-averaged freshwater flux, and A as the area of the cavity. S_{cavity} and T_{cavity} are the calculated melt-weighted bottom temperature and salinity.

Figs. 4.4 and 4.3 reveal that the two restoring experiments have distinct FRIS cavity properties. These properties appear to cycle in a manner corresponding to variability in the prescribed 9-year atmospheric forcing. As expected from fig. 4.1, the 34psu restoring experiment exhibits a warmer, fresher FRIS cavity state while the 34.45psu case has colder and saltier water mass properties. In addition to these time-series plots, fig. 4.5 shows the T/S properties within the FRIS cavity from the 34psu FRIS cavity restoring simulation (bottom panel) and the 34.45psu FRIS cavity restoring simulation (top panel). In the 34psu restoring experiment, the FRIS cavity temperature and salinity properties suggest the persistence of a fresh FRIS cavity, lacking the necessary HSSW signal for AABW production. The warmest water within the FRIS cavity in the 34.45psu restoring experiment is ≈ -1°C, while the 34psu restoring experiment has warmer, ≈-.5°C temperatures. This suggests that the FRIS cavity in the 34psu restoring experiment receives higher CDW-inflow, leading to the correspondingly high rates of meltwater production as given in fig. 4.1. In addition to these plots that analyze FRIS cavity water mass properties fig. 4.6 shows the 9-year averaged bottom temperature in the two restoring experiments. The FRIS cavity in the 34psu restoring experiment is much warmer, especially in the Filchner Trough (FT) region, compared to the 34.45psu experiment.

In addition to the water mass property analysis, fig. 4.7 shows the barotropic stream function for the 34psu (bottom panel) and the 34.45psu (top panel) restoring experiments. In the 34psu ex-

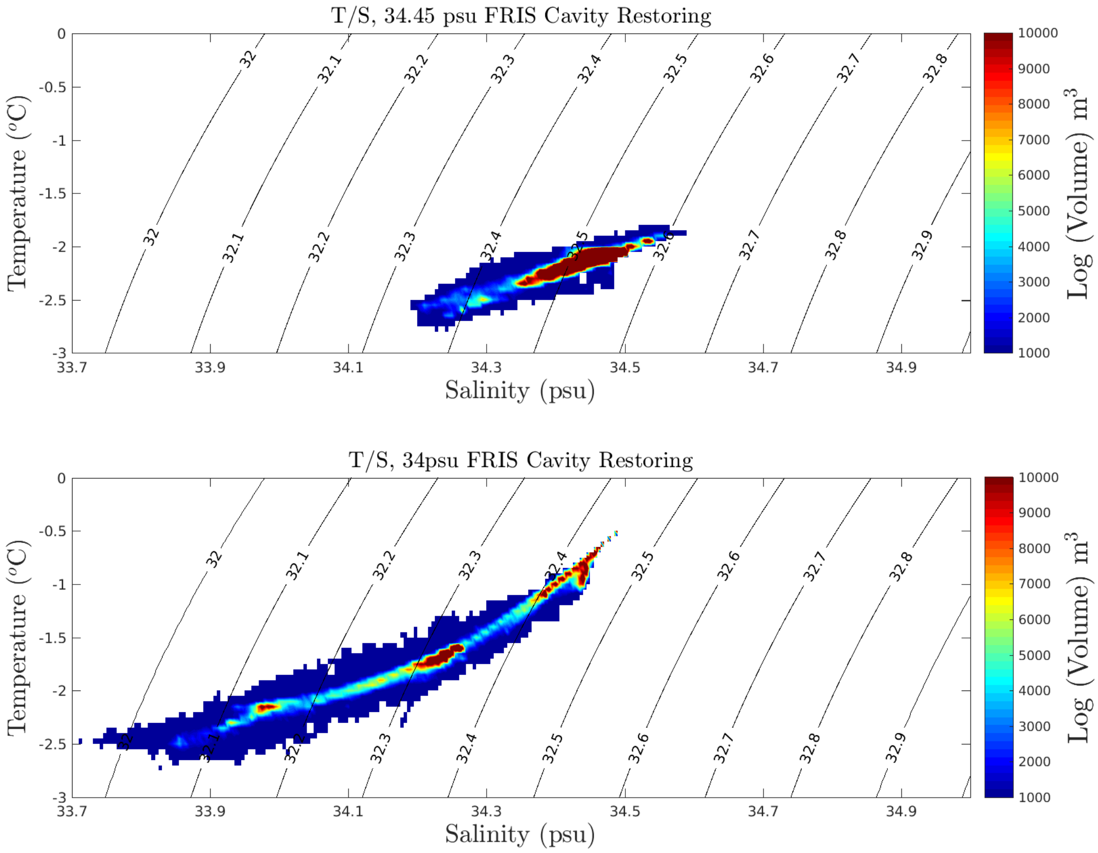

Figure 4.5: Temperature/Salinity properties within the FRIS cavity for both the 34.45psu (top panel) and 34psu (bottom panel) initial FRIS cavity restoring experiments. Values represent monthly mean averages over the last 9-year full WSRM atmospheric forcing period within the defined FRIS cavity region highlighted in the Supporting Information in fig. 6.7. Overlaid black contours spaced at .1kgm^3 refer to potential density, which is referenced to 1000m depth.

periment, the time-averaged, depth-integrated flow has persistent pathways of re-circulation within the FRIS cavity. Modified CDW (mCDW) appears to enter and recirculate especially within the FT region. The region of significant mCDW re-circulation corresponds with regions of high of basal ice shelf melt shown in fig. 4.2 as well as areas of warmer temperatures in fig. 4.6.

Overall, our analysis suggests the existence of a bi-stable FRIS cavity regime. The initial density of the FRIS cavity determines whether the cavity enters into a warm or a cold state. A

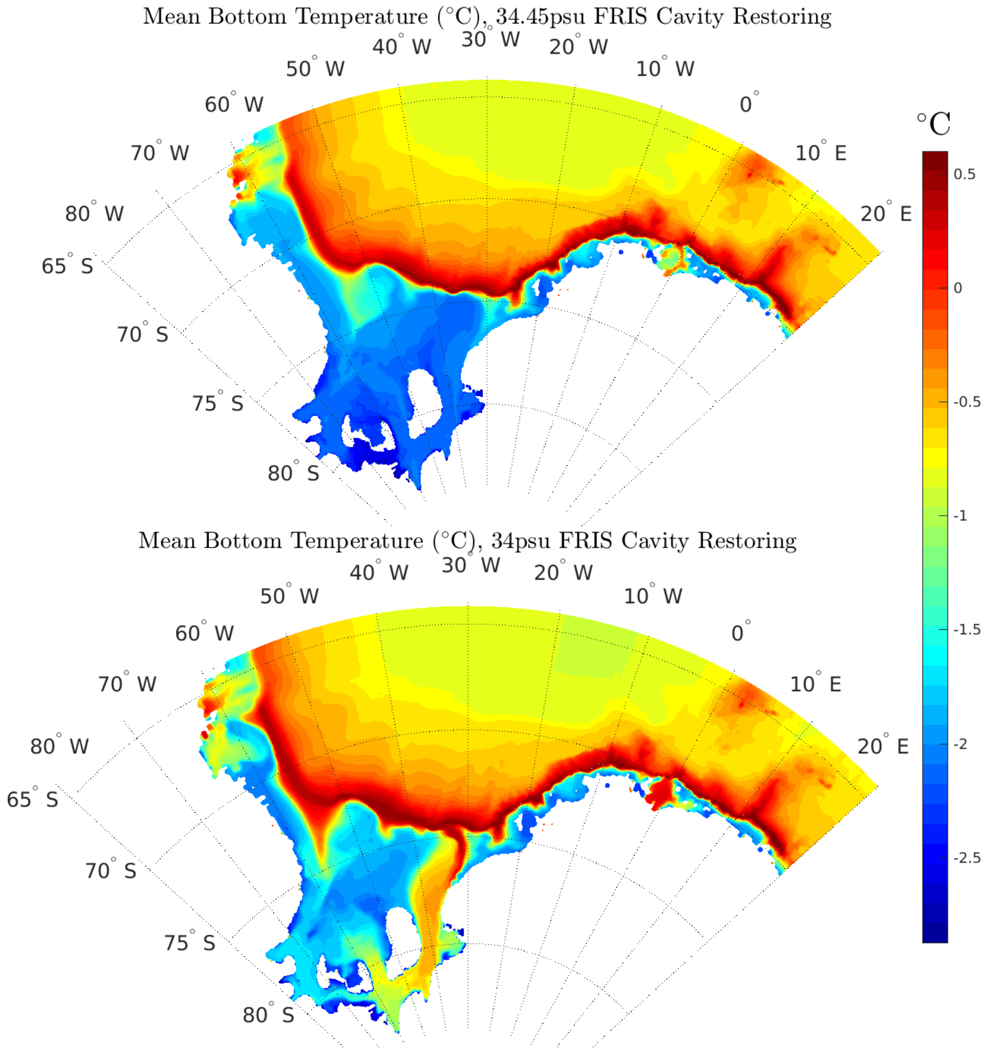

Figure 4.6: Mean bottom temperature (°C) for the 34.45psu (top panel) and 34psu (bottom panel) FRIS cavity restoring experiments. Values represent averages from over the last 9-year full WSRM atmospheric forcing period.

cold, dense initial cavity may buffer against intrusions of CDW and prevent high rates of melt.

4.3 Sensitivity to Surface Forcing Perturbations

We have established that pre-existing FRIS cavity conditions are fundamental in determining the steady-state circulation, melt rate, and water mass properties within the cavity. Next, we move to

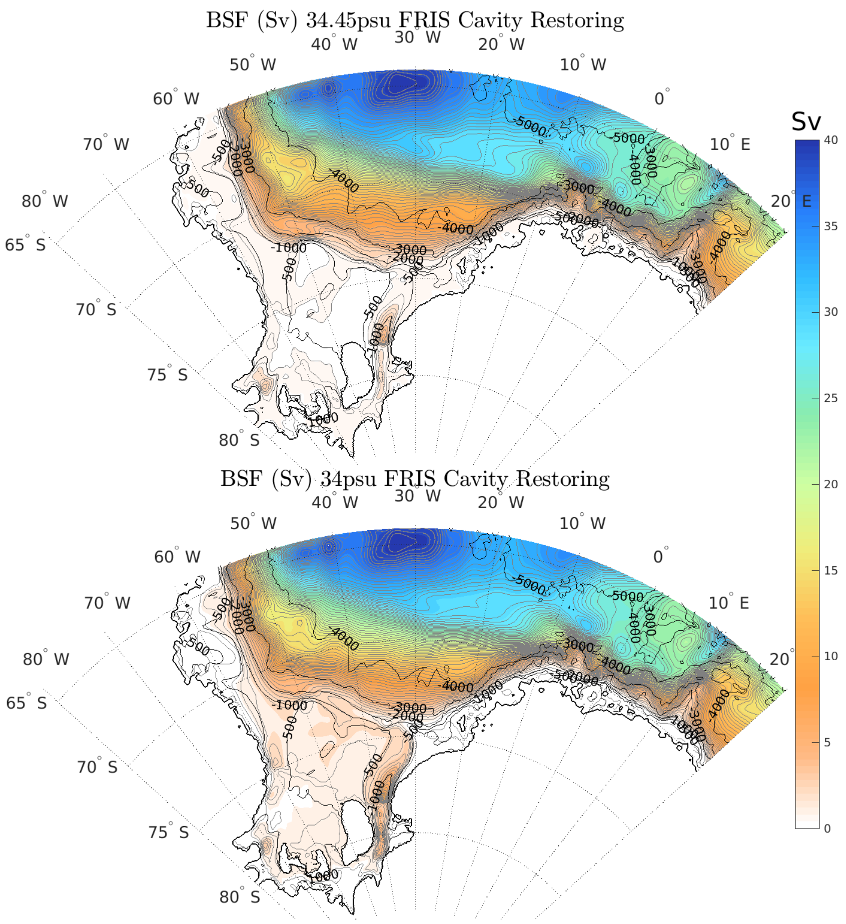

Figure 4.7: Barotropic stream function (Sv) for the 34.45psu (top panel) and 34psu (bottom panel) initial FRIS cavity restoring experiments. Values are averaged over the last 9-year full WSRM atmospheric forcing period. Gray contours are streamlines spaced at .5 Sv, while overlaid black contours refer to bathymetric depth.

understand the relationship between the warm, high-melt and cold, low-melt steady state regimes of the FRIS cavity. Specifically, we explore the potential to transition between these two states. As outlined in §4.1, Hellmer et al. (2017) demonstrates that future atmospheric forcing scenarios influence the ice-ocean interactions within the Weddell and lead to a warm, high melt FRIS cavity state. The high melt regime persists even with a return to 20^{th} century forcing. We explore the possibility that the FRIS cavity has the capacity to switch between established "high" and "low" FRIS melt states with a series of atmospheric forcing perturbation experiments.

Various surface forcing variables are perturbed to discern whether the warm and cold FRIS cavity states remain self-contained or whether one state can be reached from the other. Atmospheric forcing in the model is prescribed as a daily-averaged 9-year repeating forcing derived from AMPS (see §3.2.8). We perturb the forcing of three atmospheric variables: 2-meter temperature, 10-meter meridional wind, and 10-meter zonal wind. We chose to perturb the atmospheric winds and temperature due to their potential impacts on ocean circulation in a changing climate (*e.g.* Hellmer et al., 2012); however, future experiments will test a more varied series of atmospheric forcing parameters. In fig. 4.8, we provide initial results of FRIS integrated shelf ice melt given various atmospheric forcing perturbations in table 4.1. Experiments are initialized from the steady-state WSRM warm or cold FRIS cavity simulations after each had been run for 18 years.

Table 4.1: Experimental Atmospheric Forcing Perturbations

Initial FRIS Cavity State	Perturbation
Cold, low-melt	Zonal Winds -20 %
Cold, low-melt	Zonal Winds -50 %
Cold, low-melt	Zonal Winds 0 %
Cold, low-melt	Meridional Winds -50%
Warm, high-melt	Atmospheric Temperature -5°C
Warm, high-melt	Atmospheric Temperature -30°C
Warm, low-melt	Meridional Winds +20%

We apply various perturbations to the atmospheric forcing in simulations initialized from the 18-year cold FRIS cavity steady-state of the 34.45psu restoring experiment. These experiments include perturbing the zonal winds by (1) reducing the strength by 50%, (2) reducing the strength by 20%, and (3) turning the zonal wind strength to zero. Given the significance of the near-Antarctic easterly winds to processes discussed in §2, we expected these perturbations to substantially impact warm water inflow into the FRIS cavity. In particular, we predicted that a reduction in the strength of the easterly winds would reduce the strength of the ASF and increase the corresponding heat transfer towards the ice shelves. Contrary to these expectations, this change to the zonal wind strength did not impact the FRIS cavity melt rate after 20 years of simulation time. We then experimented with the meridional winds by reducing their strength by 50%. In this experiment, the FRIS cavity state shifts rapidly to a high melt regime reached after $\approx$ 15 years. This suggests that the meridional winds are key in controlling heat transport into the FRIS cavity.

Surface forcing perturbation experiments are then performed with initial conditions prescribed from the 18-year steady-state 34psu restoring experiment. As shown in fig. 4.8, experiments started from the initial warm FRIS cavity state have higher variability in the integrated melt rate during the 9-year repeating forcing period than those started from the initial cold cavity state. To test the sensitivity of the warm FRIS cavity, we first decreased the atmospheric temperature from the daily averaged value by (1) -5°C and (2) -30°C. Given substantial cold anomalies to the atmospheric state, we expected FRIS melt rate to decrease. Surprisingly, this change in the atmospheric temperature did not allow the FRIS to enter a low melt, cold state. Given that the strength of the offshore winds in the cold initial FRIS cavity experiments proved crucial in altering the FRIS cavity state, we then chose to increase the strength of the meridional winds by 20%. In this experiment, the FRIS begins to gradually return to a state of low melt that is seen in the control "cold-start" experiment after $\approx$ 35 years. Overall, the results of the perturbations to the meridional winds in the cold and warm initial FRIS experiments demonstrate the potential for a transition between high and low-melt FRIS cavity states.

4.4 Sensitivity to Offshore Wind Perturbations

The results shown in in §4.3 imply that changes to the strength of the meridional winds allow for a switch from a "warm-to-cold" and from a "cold-to-warm" FRIS cavity state. Given these transitions, we perform an array of meridional wind perturbation experiments to establish the range over which the FRIS is bi-stable, for which both warm and cold FRIS cavity states can occur when forced with identical offshore wind perturbations. These experiments are initialized from the 18-year steady state fields of either the 34.45psu (cold initial state) or the 34psu (warm initial state) FRIS cavity restoring simulations. The experiments are run until a new-steady state in the FRIS cavity is reached for a minimum of nine years, corresponding to the length of the WSRM atmo-

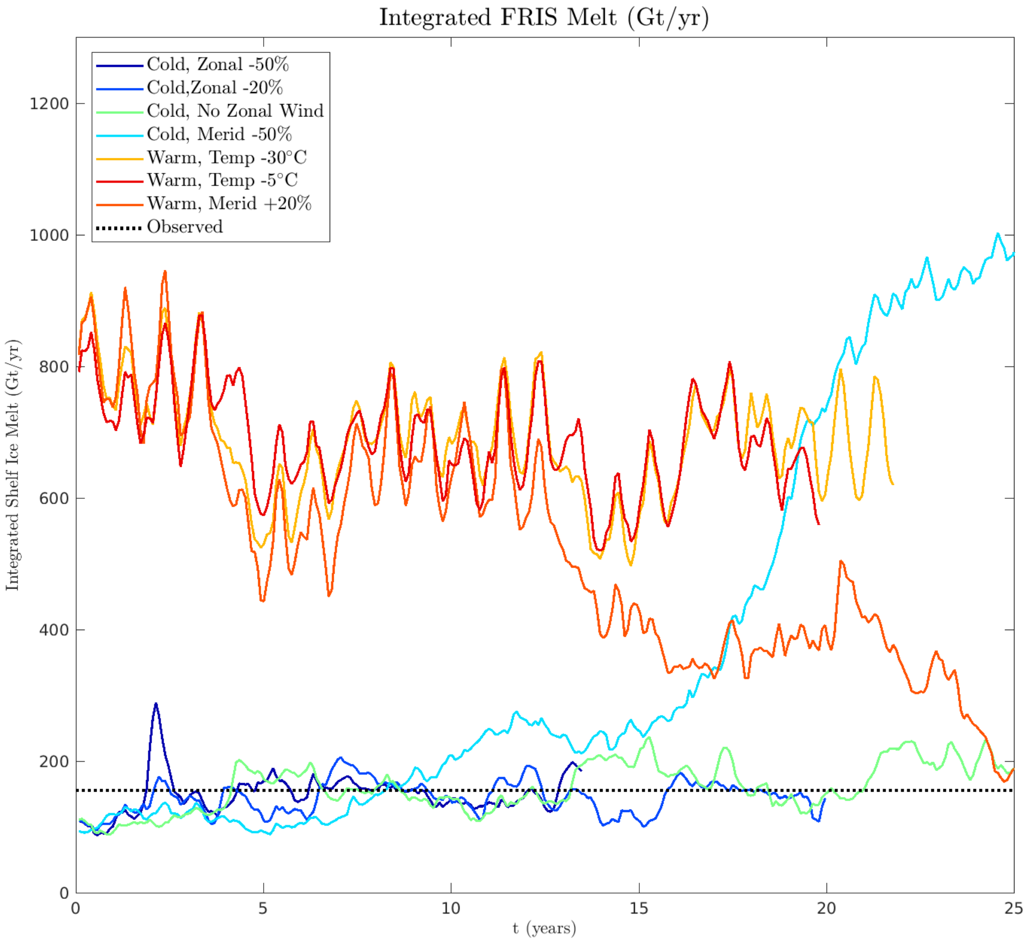

Figure 4.8: Integrated Monthly Shelf Ice Melt (Gt) time series for surface forcing perturbation experiments with an initial warm or cold initial FRIS cavity state. The dotted black lined refers to the observed FRIS melt rate (Rignot et al., 2013).

spheric forcing repeat-cycle. The perturbation scheme is performed with the following expression:

$$V_{pert} = \chi V_{wind}, \tag{4.2}$$

with V_{pert} being the offshore wind strength, V_{wind} being the daily-averaged offshore wind speed, and χ being the wind perturbation. Equation 4.2 allows for a simple experimental design that will test the FRIS cavity sensitivity to changes in the offshore wind strength. Based on the results in §4.3, perturbations of a few tens of percent resulted in drastic melt rate changes. Therefore, we choose the experimental values of χ to range from .5 (-50%) to 1.2 (+20%), corresponding from a 50% decrease to a 20% increase to the offshore wind strength. χ is plotted versus the resulting full 9-year mean offshore wind speed field in fig. 4.9. This figure offers a quantification of the mean offshore wind stress in each respective perturbation while also confirming that the applied perturbations are consistent.

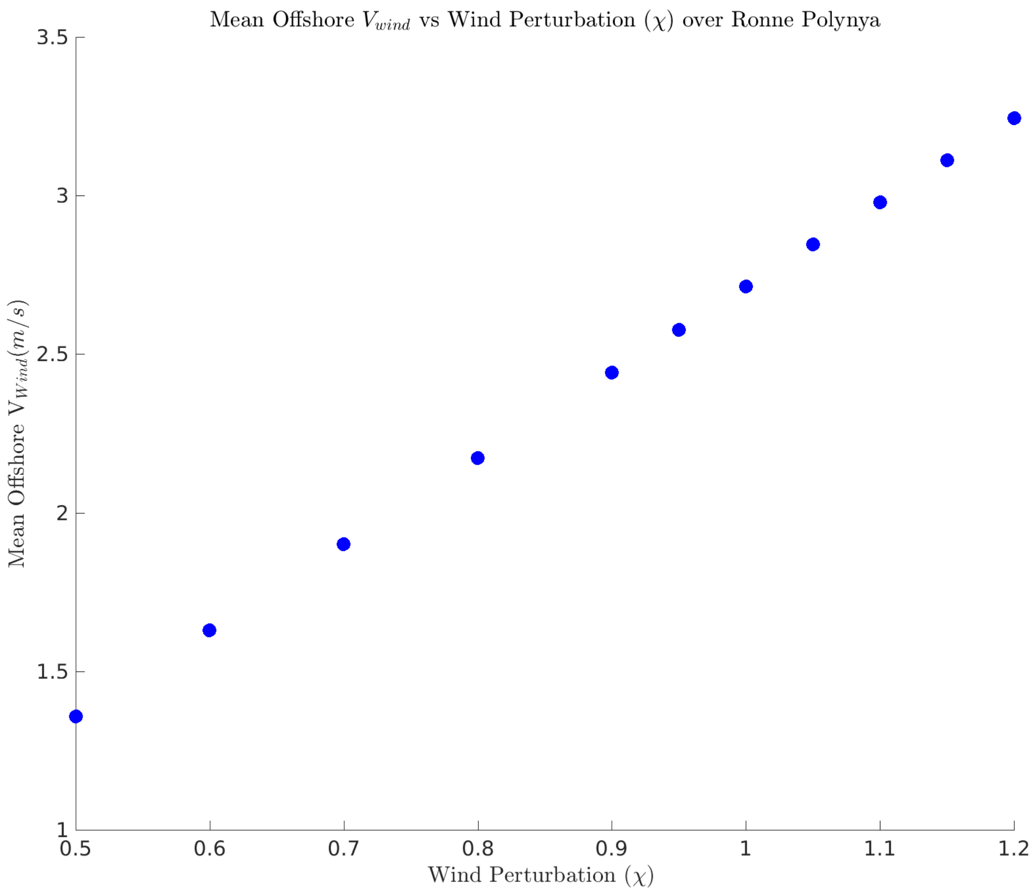

Figure 4.9: Mean Offshore Wind speed (m/s) versus offshore wind perturbation, χ, for each respective experiment. The offshore wind speed is averaged over the full 9-year WSRM atmospheric forcing period over the Ronne Polynya region highlighted in fig. 6.8.

As shown in the 34psu and 34.45psu FRIS cavity restoring experiments in figs. 4.5, 4.7, and 4.1, we diagnose the respective warm or cold FRIS cavity state with regards to FRIS cavity melt, bottom temperature, and bottom salinity. We use these properties to demonstrate that a range of wind perturbations allows both warm and cold FRIS cavity states to co-exist. In the following sections, we analyze these respective properties averaged over the last full 9-year surface forcing cycle in each steady-state offshore wind perturbation experiment.

4.4.1 Sensitivity to FRIS Cavity Melt Rate, Bottom Temperature, and Bottom Salinity

Integrated shelf ice melt rates are plotted against the wind perturbations (χ) for each offshore wind experiment. We plot the averaged integrated shelf ice melt rate for each experiment in fig. 4.10. In this figure, blue dots correspond to experiments started from an initial cold FRIS cavity, and red dots correspond to warm initial FRIS cavity experiments. Red and blue lines are drawn between the initial warm and cold experiments to connect the pattern in the melt rate as the offshore wind strength is changed. Control offshore wind strength experiments are shown with black squares, and black arrows show the direction of the melt rate as χ is decreased and increased from the control wind strength.

As the wind strength is both increased and decreased in fig. 4.10, a transition in the melt rate occurs for both the initial warm and cold case experiments. As χ is increased to a value of +15% (1.15), both the warm and cold initial FRIS cavities approach a similar low-melt value of $\approx$ 200 Gt/yr. Likewise, as χ is decreased to a reduction of the wind strength of -40% (.6), both the warm and cold initial FRIS cavities approach a similar high-melt rate of $\approx$ 1000 Gt/yr. Between χ values of .7–1.1, the FRIS cavity is bi-stable with both high ($\approx$ 600-800Gt/yr) and low ($\approx$ 150Gt/yr) melt rates. In this range of χ, the final steady-state that is reached in the experiments is determined by the initial FRIS cavity state; in other words, one FRIS cavity state cannot be reached from the other.

After analyzing the sensitivity to melt rate, we investigate whether a similar transition between warm and cold cavity states exists in terms of FRIS cavity water mass properties. The two key variables that we examine are the melt-weighted FRIS bottom cavity temperature and salinity, defined in equations 4.1b and 4.1a, respectfully. Temperature and salinity values are sampled from the bottom of the FRIS cavity in gridcells where the most meltwater is found; therefore, we assume that they are most significant in determining whether the cavity exists in the warm or

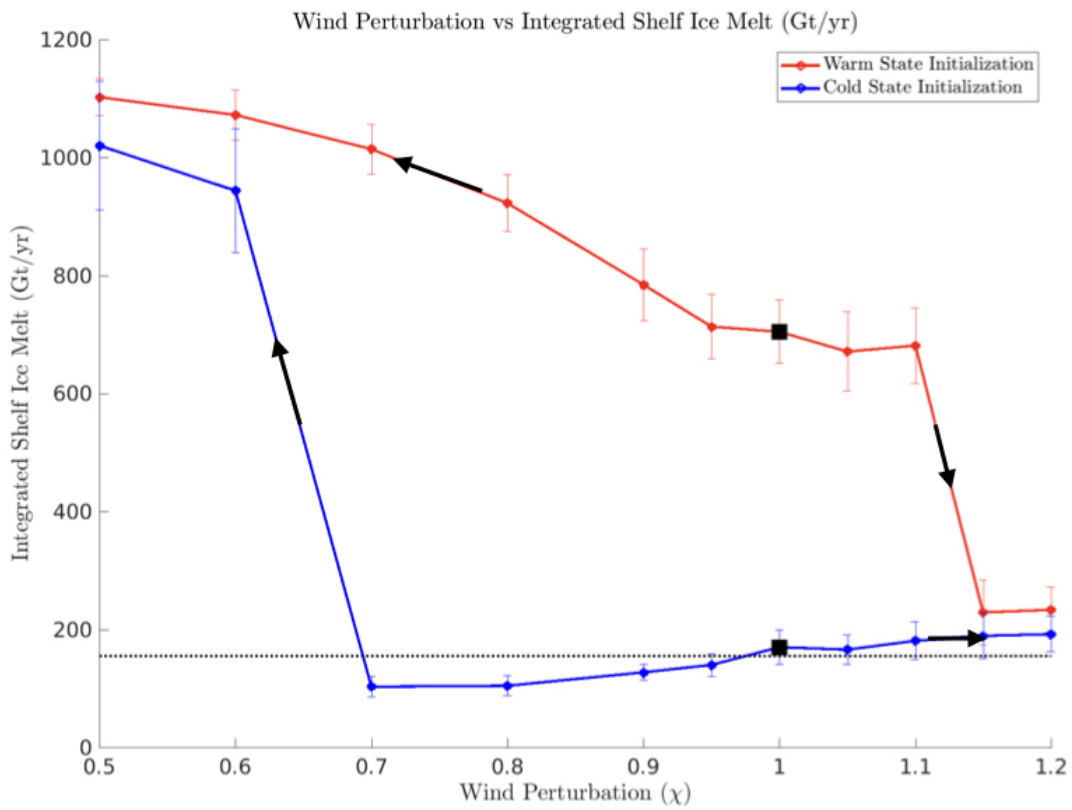

Figure 4.10: Wind perturbation versus integrated shelf ice melt (Gt/yr). Values represent the average in the monthly mean shelf ice melt from the last 9-year full WSRM atmospheric forcing period and from the FRIS cavity region of the WSRM domain shown in the Supporting Information fig. 6.7. Experiments are initialized from either a warm (red dots) or cold (blue dots) initial FRIS cavity state. The dotted black line represents observed melt rate from Rignot et al. (2013), and error bars refer to errors of one standard deviation from the monthly averaged integrated melt.

cold steady-state. Based on time-series plots of melt rate and cavity properties in figs. 4.1, 4.3, and 4.4, which compare the 34psu and 34.45psu cavity restoring experiments, we conclude that different water masses may have access to the cavity in the warm versus the cold regimes. This motivates the analysis in figs. 4.11 and 4.12, which give the 9-year averaged FRIS bottom cavity temperature and salinity, respectfully, against the value of χ for each cold and warm initial FRIS cavity experiment. Similar to fig. 4.10, blue dots correspond to experiments with an initial cold FRIS cavity, and red dots correspond to warm initial FRIS cavity experiments. Red and blue lines are drawn between experiments to connect the pattern in the melt rate as the offshore wind strength is changed. Black squares represent control offshore wind simulations, and black arrows show the direction of the melt rate as χ is decreased and increased from the control wind strength.

As in the integrated melt, the FRIS cavity has bi-stable properties with regards bottom temperature and salinity within a range of offshore perturbations. In the warm experiments, as χ reaches a value of 1.15, the properties approach the values of the cold experiment, with a sharp decrease in cavity temperature and a corresponding increase in cavity salinity; however, the initial warm cavity experiments do not quite reach the bottom salinity vales of the initial cold cavity simulations. Future experimentation with longer simulation times. Meanwhile, in the initial cold cavity experiments, as the value of χ is reduced to .6, the bottom cavity freshens and warms, overlapping with the properties seen in the initial warm FRIS cavity state.

We visualize the shift in FRIS cavity properties with changes to the strength of the offshore wind by overlaying temperature and salinity properties from both warm and cold FRIS initial FRIS cavity perturbation experiments. The initial warm FRIS cavity experiments are overlaid in fig. 4.13, while the initial cold FRIS cavity experiments are overlaid in fig. 4.14. Fig. 4.13 demonstrates a transition from a fresh, warmer cavity to a colder, saltier cavity with increasing offshore wind strength. The warm signature from enhanced mCDW inflow is reduced with stronger offshore winds to a maximum value of $\approx$ -.5°C. Likewise, fig. 4.14 shows a transition from a cold, relatively salty FRIS cavity to a warmer, fresher FRIS cavity as the offshore wind strength is decreased.

4.5 Developing a Conceptual Model of FRIS Bi-Stability

The results of the WSRM offshore wind perturbations experimentally determine the range of offshore wind strength over which the FRIS is bi-stable, for which both cold and warm FRIS cavity steady-states can occur. Motivated by our analysis of integrated melt rate and melt-weighted bottom salinity and temperature in figs. 4.10, 4.12, 4.11, we posit that FRIS cavity bi-stability results from different water masses invading the cavity in the warm versus the cold cavity states. In particular, we posit that the cold FRIS cavity state is HSSW-controlled, meaning that HSSW is flooding the cavity. On the other hand, the FRIS cavity warm state is driven by CDW cavity invasion. This

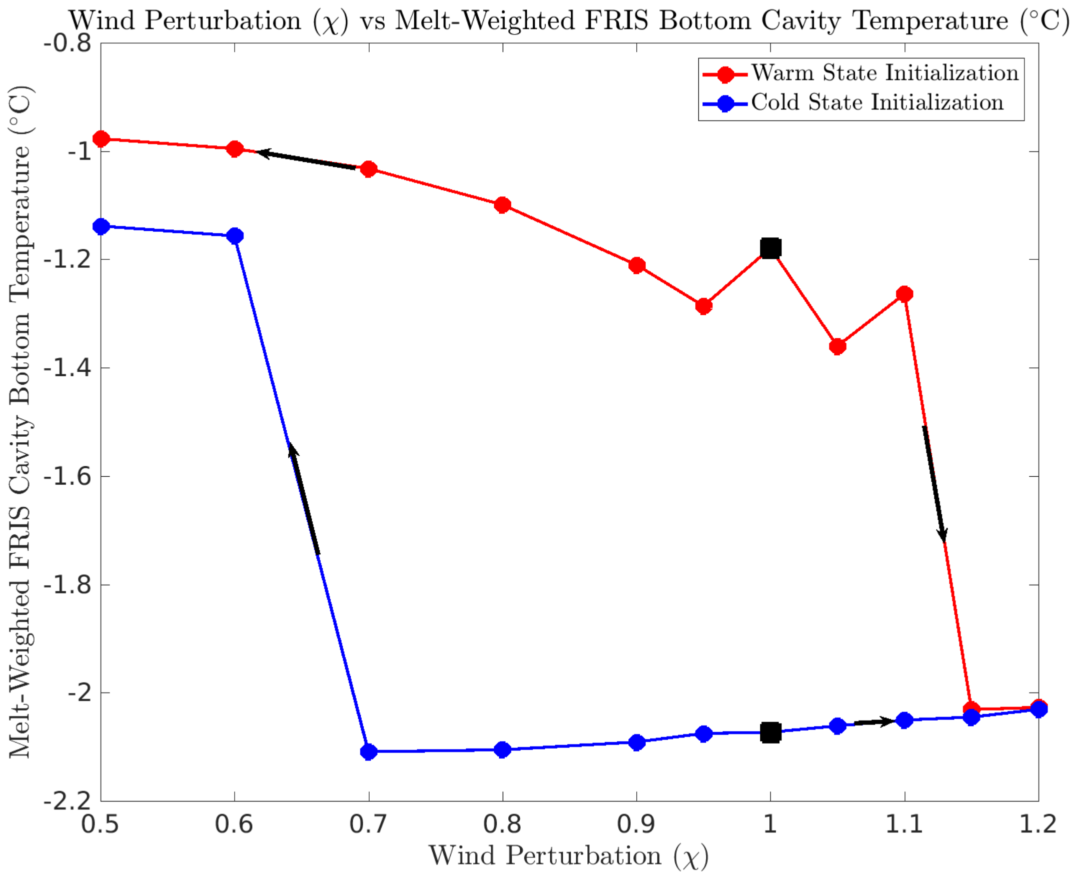

Figure 4.11: Wind perturbation versus melt-weighted FRIS cavity temperature (°C). Values represent the 9-year monthly mean average over the last complete WSRM atmospheric forcing period. Experiments are initialized from either a warm (red dots) or cold (blue dots) initial FRIS cavity state. Data is extracted from the FRIS cavity region of the WSRM domain shown in the Supporting Information in fig. 6.7. The plotted bottom temperature values are normalized by weighting the temperature values in gridcells with positive melt against the total freshwater flux within each respective gridcell (see equation (4.1b). Black squares represent control runs from either cold or warm initial FRIS cavity state.

concept is illustrated in a schematic in fig. 4.15. At the surface near-Antarctica, cold AASW lies above warmer, saltier CDW; CDW that crosses onto the shelf leads to basal meltwater production. Meanwhile, offshore winds advect ice away from the coast and create latent heat polynyas (Smith, Muench, and Pease, 1990). Within the polynya, latent heat release and further ice production take

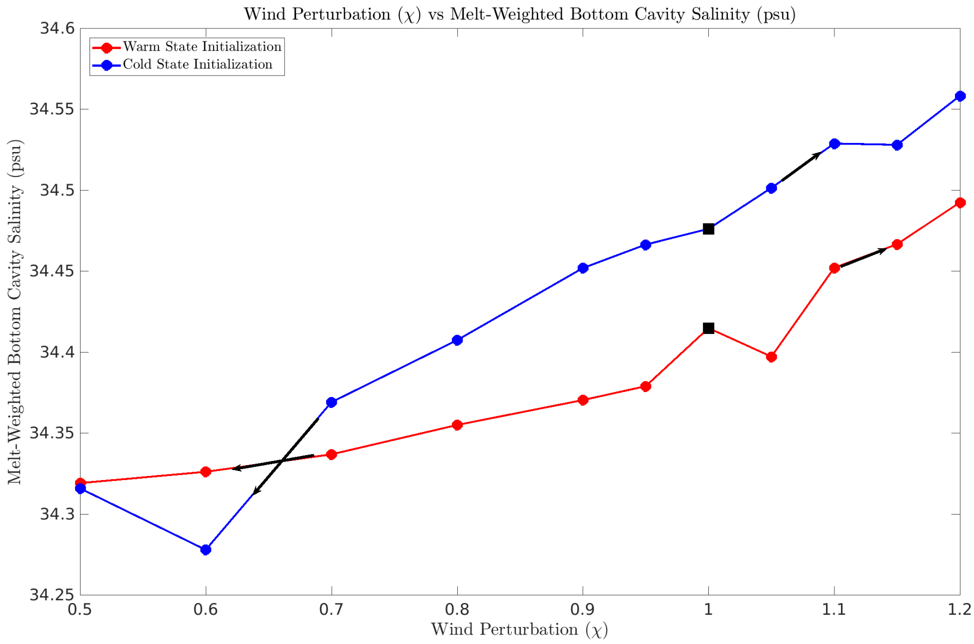

Figure 4.12: Wind perturbation versus melt-weighted FRIS cavity salinity (psu). Values represent monthly mean averages over the last 9-year full WSRM atmospheric forcing period. Experiments are initialized from either a warm (red) or cold (blue) initial FRIS cavity state. Data is extracted from the FRIS cavity region of the WSRM domain shown in the Supporting Information in fig. 6.7. Plotted bottom salinity values are normalized by weighting the salinity values in gridcells with positive melt against the total freshwater flux within each respective gridcell. Black squares represent the control runs from either cold or warm initial FRIS cavity states.

place, releasing brine and forming HSSW (Nicholls et al., 2009). HSSW recirculates within the ice shelf cavity and transforms into cold, dense ISW that can escape to the ocean abyss (Foldvik and Østerhus, 2001). In addition to the schematic in fig. 4.15, a cross-section of the WSRM potential temperature in fig. 4.16 provides a visualization of Weddell Sea water masses at the ice-shelf ocean interface. The plotted cross-section is located at 40°W, within our defined Ronne Polynya region in fig. 6.8.

The conceptual model developed in this chapter postulates that the density at the mouth of the ice shelf cavity determines the resultant properties of the FRIS cavity. The following expressions

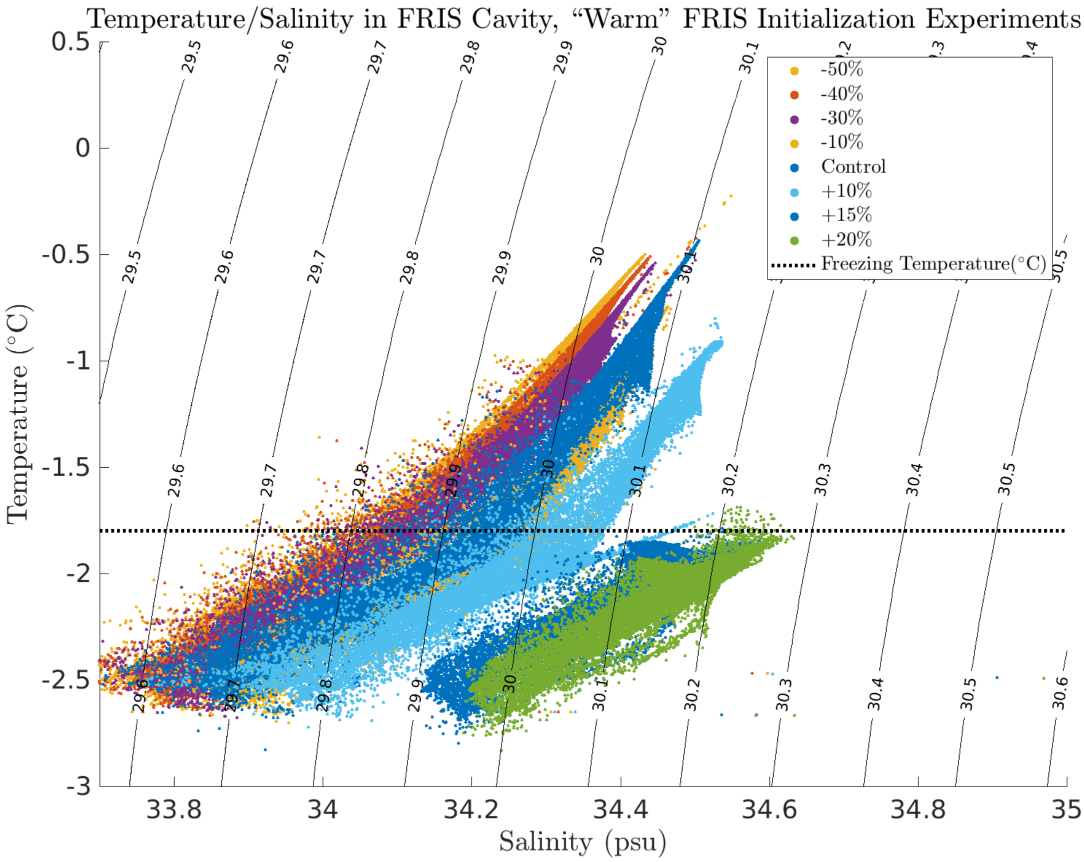

Figure 4.13: Temperature/Salinity plot of warm initial FRIS cavity experiments, colored by respective perturbation. Values are sub-sampled from every 10^{th} data point within the FRIS cavity region shown in fig. 6.7. Property values represent the monthly mean averages from the last 9-year full WSRM atmospheric forcing period of each respective simulation. Overlaid black contours refer to potential density referenced to 500m. The horizontal dotted black line refers to the surface freezing temperature.

stipulate that (1) the FRIS cavity exists in a warm, CDW-controlled state when the density of CDW is greater than that of HSSW, and (2) the FRIS cavity is in a cold, HSSW-controlled state when the density of HSSW is greater than that of CDW:

$$\theta_{Cavity} = \left\{ \begin{array}{l} \theta_{CDW} : \sigma_{CDW} > \sigma_{HSSW}, \\ \theta_{HSSW} : \sigma_{CDW} < \sigma_{HSSW}, \end{array} \right\}$$

If $\sigma_{HSSW} < \sigma_{CDW}$, the FRIS cavity exists in a high-melt, warm state. Given a high-melt state, the

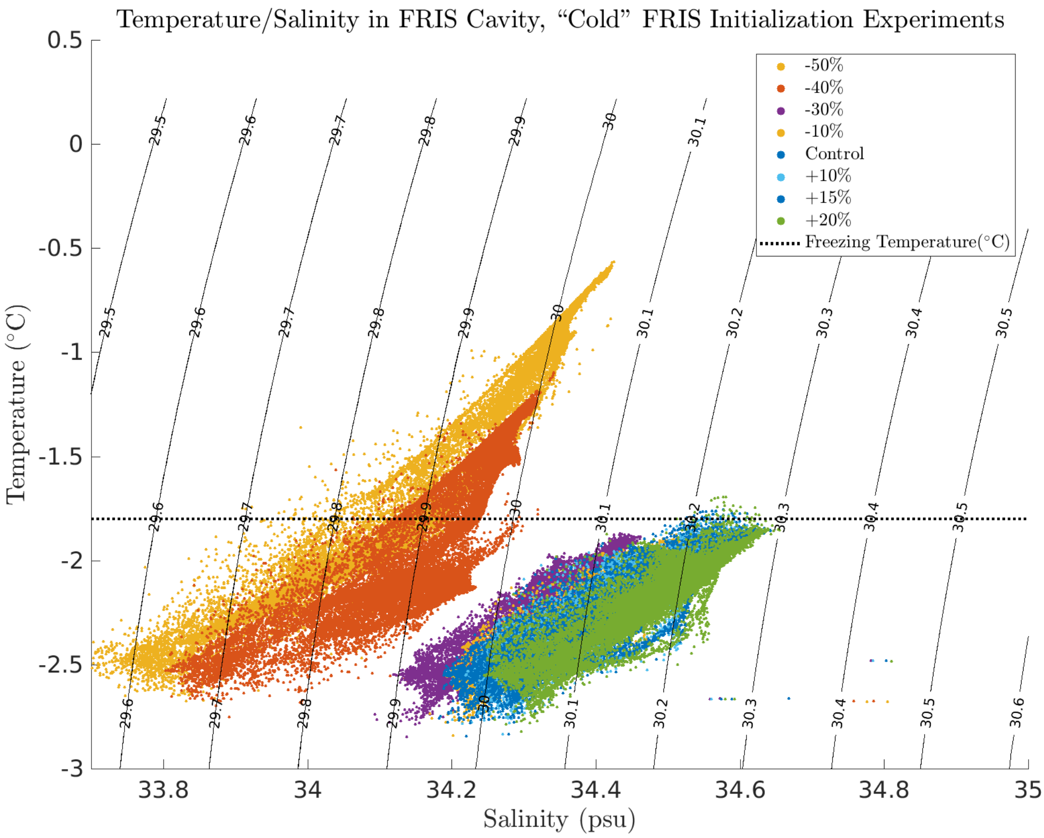

Figure 4.14: Temperature/Salinity plot of cold initial FRIS cavity experiments, colored by respective perturbation. Values are sub-sampled from every 10^{th} data point within the FRIS cavity region of the WSRM domain shown in the Supporting Information in fig. 6.7 and averaged over the last 9-year full WSRM atmospheric forcing period. Overlaid black contours refer to potential density, which is referenced to 500m. The dotted horizontal black line refers to the surface freezing temperature.

abundance of freshwater further freshens HSSW, leading to a positive feedback. In contrast, if $\sigma_{HSSW} > \sigma_{CDW}$, meltwater production does not lighten HSSW to the point that CDW is the denser water mass. Instead, HSSW continues to flood the cavity. An opposite positive feedback exists from smaller rates of basal melt and freshwater production, increasing the density of HSSW.

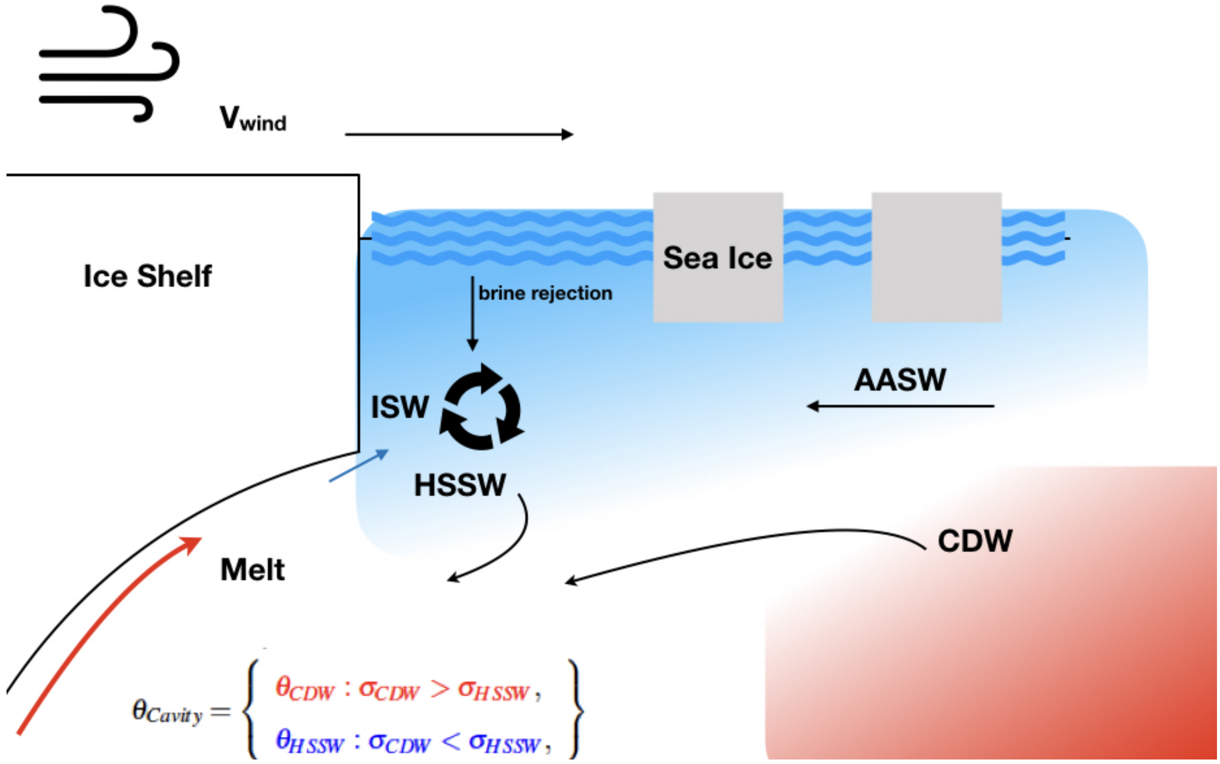

Figure 4.15: Schematic of the ice-shelf ocean interface that highlights the key water masses and mechanisms involved in our conceptual model. In the upper water column, AASW circulates around Antarctica. At the coastline, offshore winds blow sea ice offshore, allowing for latent heat polynya formation. Brine rejection leads to HSSW formation, which recirculates within the cavity to form ISW, the dense water mass that flows downslope to the deep ocean. In addition, below AASW exists warmer and saltier CDW, which flows onto the shelf to access to the ice shelf cavity and create basal melt. Our conceptual model postulates that the FRIS cavity is in a warm or cold state depending on whether HSSW or CDW floods the cavity.

4.5.1 Defining the Salinity of HSSW

While HSSW formation occurs at the mouth of the FRIS by brine rejection (Nicholls et al., 2009), it is cooled and diluted from basal melt as it flows downward to the base of the cavity (Nicholls et al., 2001; Nicholls et al., 2009). We postulate that the resultant salinity of HSSW comes from the ambient salinity of AASW, which is increased by salt input by brine rejection; the salinity

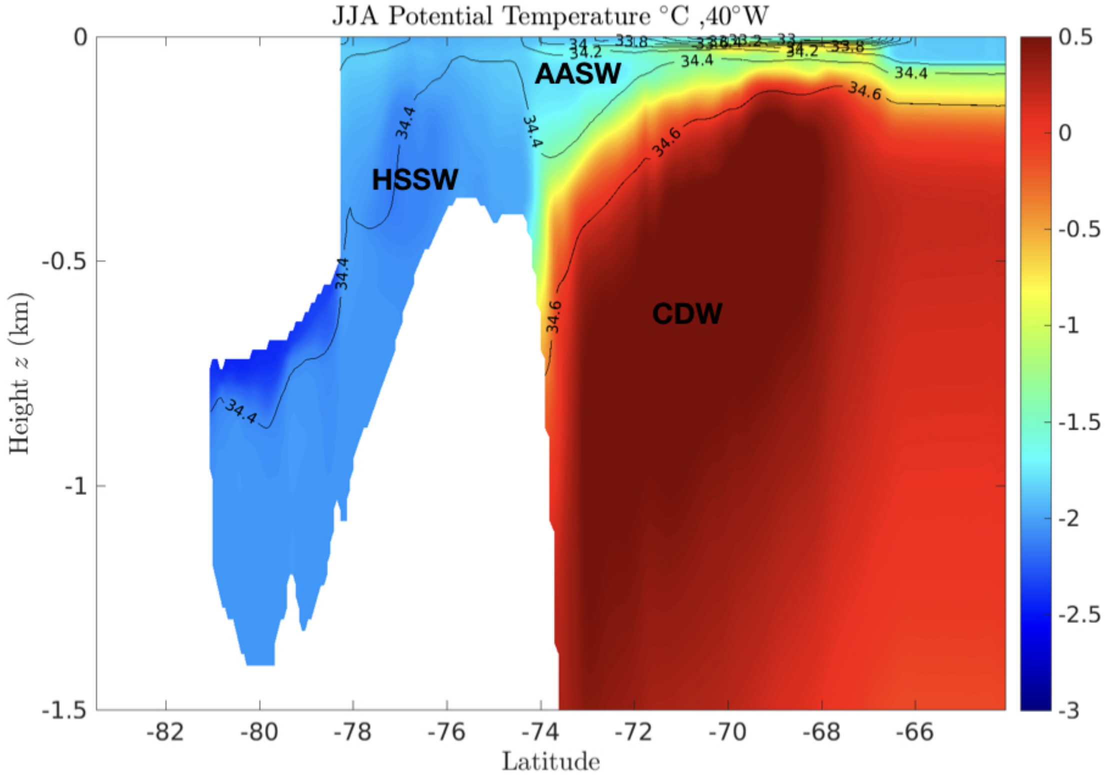

Figure 4.16: Cross-section of WSRM potential temperature at 40°W. Values are averaged over a complete 9-year atmospheric forcing period from the control offshore wind simulation with a cold initial FRIS state. Salinity contours are overlaid in black and spaced at .2psu. This cross-section at the ice-shelf ocean interface highlights key water masses of HSSW, AASW, and CDW involved in our conceptual model of FRIS cavity bi-stability.

of HSSW is then decreased by freshwater emerging from the base of the cavity. Therefore, we define the salinity of HSSW, S_{HSSW}, as the sum of the contributions of AASW salinity, the salt flux due to polynya formation, and the negative salt flux contribution from freshwater. The resultant expression for S_{HSSW} is given as:

$$S_{HSSW} = S_{AASW} + \Delta S_{polynya} - \Delta S_{melt}. \tag{4.3}$$

In equation (4.3), $\Delta S_{polynya}$ refers to the salt input from polynya formation and -ΔS_{melt} represents a modification due to negative salt flux from freshwater production. HSSW has various source waters (Nicholls et al., 2009); we make the assumption that the salinity of HSSW depends upon the transport of AASW crossing onto the Ronne Ice Shelf. Therefore, the ultimate value of S_{HSSW} depends on this transport, ψ. Consequently, this value is fundamental in our calculation of S_{HSSW}. We estimate the value of ψ with the expression:

$$\psi \equiv \frac{HL_xL_y}{T}. \tag{4.4}$$

The length of the FRIS cavity, L_x, is estimated to be $\approx$ 1000km and a water column depth at the ice shelf face, H, is estimated to be $\approx$ 500m. Furthermore, the offshore distance of the polynya, L_y, is assumed to be $\approx$ 50km. We choose the time period, T, over which to evaluate the transport as the length (time) of the winter season (JJA), which is $\approx 10^7$s. By substituting our values for H, L_y, L_x, and T in equation (4.4), we arrive at $\psi \equiv 2.2$ Sv, which is comparable to the value of cross-shelf transport estimated from observations (Nicholls and Fedak, 2008)]. The value of ψ, as discussed in §4.5.3, is fitted to give us the experimentally given values of S_{HSSW}. Future work will aim to predict the transport explicitly by diagnosing the variation in the water mass transformation among experiments.

As expressed in equation (4.3), we define the total salt flux from latent heat polynya ice production as $\Delta S_{polynya}$. In the Weddell, latent heat polynyas occur primarily adjacent the Ronne Ice Shelf during wintertime, when offshore winds are strongest (Comiso and Gordon, 1998). The growth rate of ice is a function of the exposure, in time and temperature, of ice to the atmosphere (Petrich and Eicken, 2017). As stronger offshore winds will drive more ice away from the coast, increased ice production occurs in the newly ice-free region, further increasing the salt flux to the ocean. Therefore, the salt flux from polynya formation in the Southwest Weddell can be expressed as:

$$\Sigma_{polynya} \equiv \Sigma_{polynya_o} + C_{polynya} V_a, \tag{4.5}$$

where $\Sigma_{polynya}$ is the integrated salt flux, $\Sigma_{polynya_o}$ is the initial integrated salt flux, and V_a is the offshore wind speed. $C_{polynya}$ is the constant that represents the rate of change of salt flux given changes to wind speed. In free ice drift, when neglecting the Coriolis force and in absence of other forces in the sea-ice momentum balance, the air-ice and air-ocean drag are equivalent. Therefore, we expect the sea ice velocities to be proportional to the offshore wind speeds. We define $\Delta S_{polynya}$, the salt flux from polynya formation in equation (4.3) from $\Sigma_{polynya}$ as follows:

$$\Delta S_{polynya} \equiv \frac{\Sigma_{polynya}}{\rho_{ref}\Psi}. \tag{4.6}$$

We now define the negative salt flux input from freshwater that contributes to the total salinity of HSSW in equation (4.3). We make the assumption that the integrated freshwater flux varies linearly as a function of the cavity temperature. This is consistent with the governing ice-ocean heat fluxes from equations (3.3a)–(3.3c) in §3, which define the ice-ocean heat flux as a linear function of the temperature of the water adjacent to the shelf ice. Therefore, we express the total freshwater flux as a constant, C_{melt}, multiplied by the difference between the cavity temperature and the freezing temperature:

$$\Sigma_{melt} \equiv \Sigma_{melt_o} + C_{melt}\left(\theta_{cavity} - \theta_f\right). \tag{4.7}$$

In this equation, Σ_{melt} represents the integrated salt flux from freshwater production, Σ_{melt_o} represents an initial salt flux from freshwater production, θ_{cavity} represents the temperature of the cavity, and θ_f represents the freezing temperature. Salt fluxes from freshwater production were calculated by multiplying the integrated freshwater flux by a reference salinity, S_{ref}.

Since the temperature anomaly from freezing at the ice shelf base drives meltwater production, θ_f is defined with reference to the melt-weighted ice-shelf draft depth:

$$z^{\star}_{(Ice-Shelf)} \equiv \frac{\int_{\overline{F_{melt)}}^{t}>0} z_{(Ice-Shelf)}\overline{F_{melt}}^{t}}{\int_{\overline{F_{melt}}^{t}>0} \overline{F_{melt}}^{t}\, dA}. \tag{4.8}$$

In equation (4.8), we define $z_{(Ice-Shelf)}$ as the depth of the ice shelf draft, $\overline{F_{melt}}^{t}$ as the nine-year averaged integrated freshwater flux, and A as the area of the FRIS cavity. θ_f is calculated from the linear equation of state as follows:

$$\theta_f \equiv= (0.0901 - 0.0575 S_{z^{\star}_{(ice-shelf)}})^{\circ} - 7.61\times 10^{-4}\frac{\mathrm{K}}{\mathrm{dBar}}\, p_{z^{\star}_{(ice-shelf)}}, \tag{4.9}$$

where $S_{z^{\star}_{(Ice-Shelf)}}$ and $p_{z^{\star}_{(Ice-Shelf)}}$ are defined as the salinity and pressure values in gridcells at the ice-ocean interface at $z^{\star}_{(Ice-Shelf)}$. To express the freshwater flux Σ_{melt} as a salt contribution in g/kg

to the salinity of HSSW in equation (4.3), Σ_{melt} is then divided by ρ and ψ:

$$\Delta S_{melt} \equiv \frac{\Sigma_{melt}}{\rho_{ref}\psi}. \tag{4.10}$$

4.5.2 Testing Conceptual Model Assumptions

In this section, we support our conceptual model principles using experimentally determined model diagnostics.

4.5.2.1 Salt flux from Ronne Polynya

The relationship between offshore wind strength and sea ice speed is tested within the Ronne Polynya region, which is highlighted for reference in the Supporting Information in fig. 6.8. The results are shown in fig. 4.17, where averaged offshore sea ice speed is plotted against the averaged offshore wind speed over the last complete 9-year WSRM atmospheric forcing period. As we would expect, the magnitude of the offshore sea ice and wind speeds are correlated with one another in a consistent manner as stipulated by the governing sea-ice momentum bulk formulae.

The Ronne Polynya salt flux is compared to the mean offshore wind speed in each perturbation experiment. Given that sea ice speed increases with stronger offshore winds in fig. 4.17, we expect offshore winds to increase in polynya formation due to an enhanced salt flux as ice is advected away from the coast. We analyze the flux of salt in the Ronne Polynya region during JJA (austral winter) in fig. 4.18. This analysis is performed during wintertime since offshore winds reach their annual maximum speeds during this season (Hazel and Stewart, 2019). The experimental values are colored red or blue according to the steady state condition of the FRIS cavity and averaged over the last 9-year complete atmospheric forcing cycle for each respective simulation. A linear relationship exists in fig. 4.18, where the linear regression explains 95% of the variance in the salt flux in the cold FRIS steady state simulations and 97% of the variance in the warm FRIS steady state experiments. From this linear relationship, the constant coefficient for the salt flux from polynya formation, $C_{polynya}$, is $4.0\times10^{8}\ \frac{g}{m}$, and $\Sigma_{polynya_o}$ is $-1.4\times10^{8}\frac{g}{s}$.

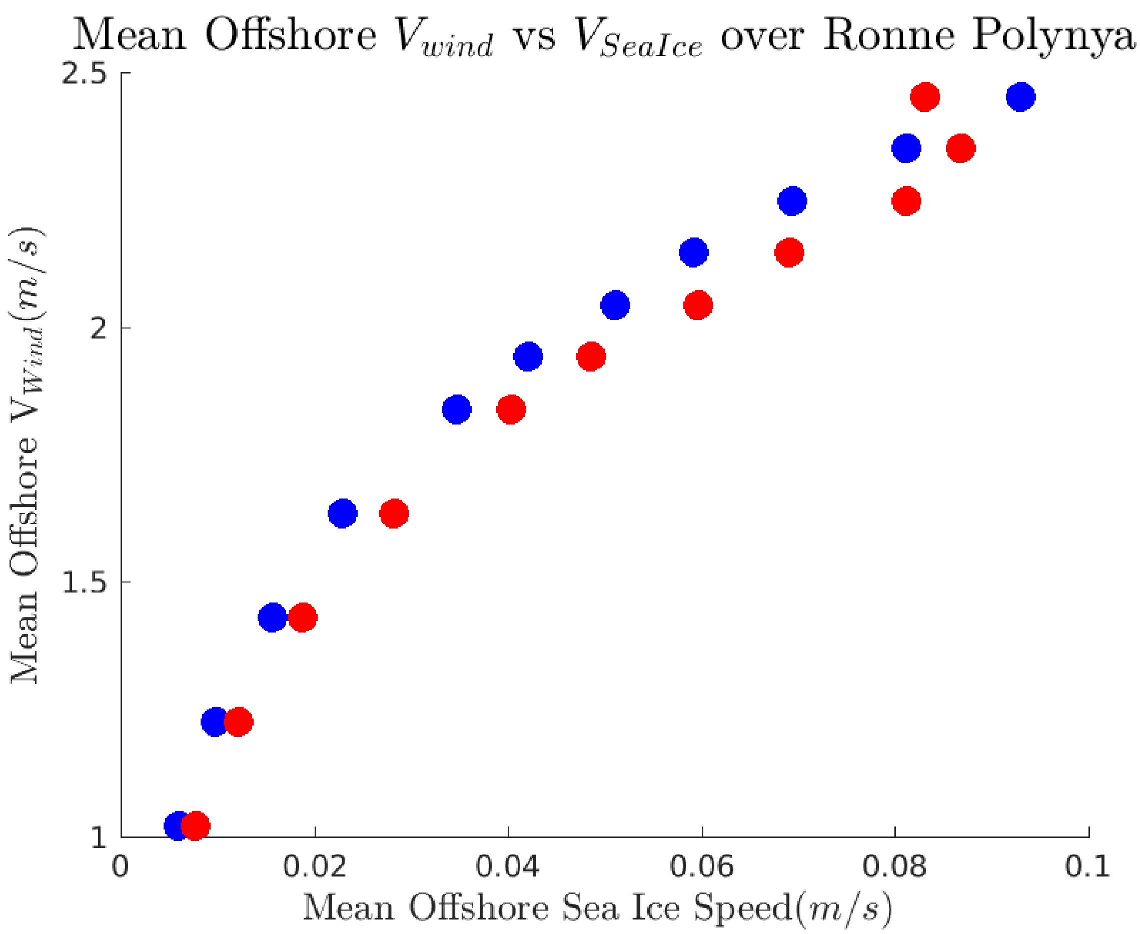

Figure 4.17: Mean Offshore Wind speed (m/s) versus mean offshore sea ice velocity (m/s) for each wind perturbation experiment. Values are calculated over the last 9-year full WSRM atmospheric forcing period and within the Ronne polynya region highlighted in fig. 6.8. Red dots represent simulations started from an initial warm FRIS cavity steady-state, and blue dots represent simulations started from an initial cold FRIS cavity steady-state.

4.5.2.2 Deducing Melt Rate from Cavity Temperature and Salinity

We explore the strength of the relationship between the cavity temperature and the freshwater flux in fig. 4.19. In this figure, we compare the integrated negative salt flux from freshwater production, -Σ_{melt}, and the melt-weighted cavity bottom temperature anomaly from θ_f. Values are averaged over the last 9-year complete atmospheric forcing cycle in each respective experiment. As in fig. 4.18, simulation results grouped as red or blue according to whether a steady-state warm (red)

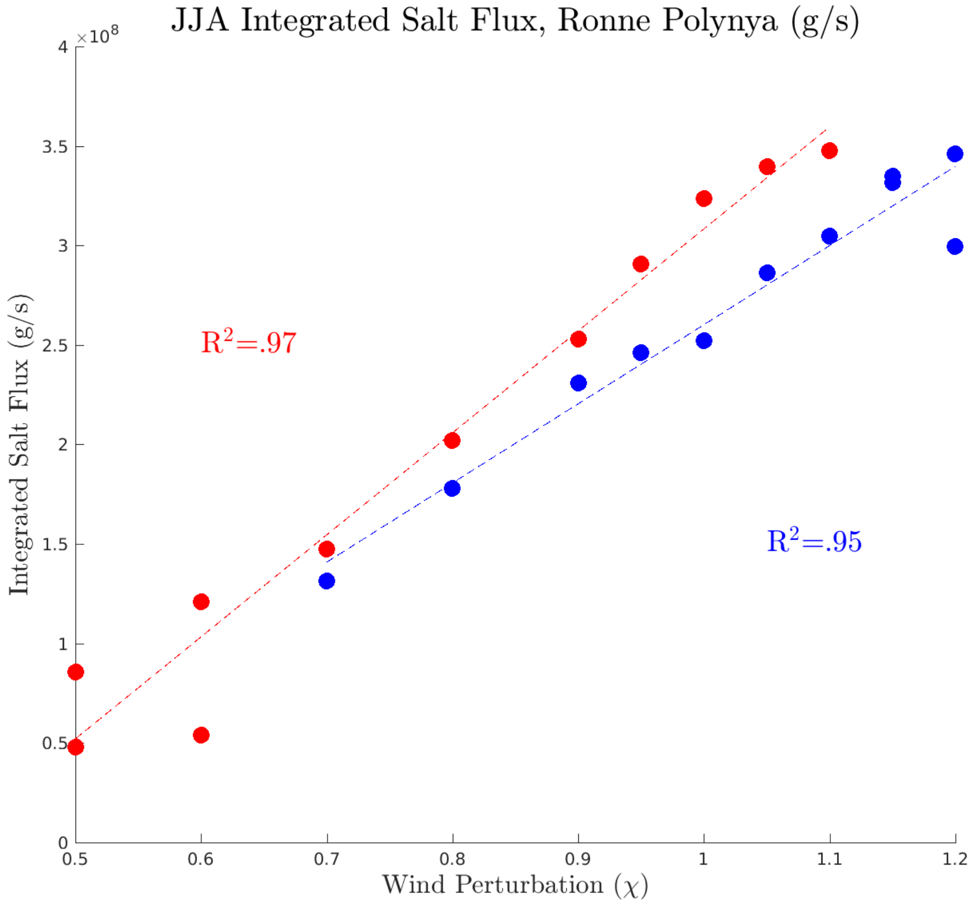

Figure 4.18: Mean JJA Integrated Salt Flux (g/s), plotted for each respective wind perturbation experiment. Values represent the JJA average over the last 9-year full WSRM atmospheric forcing period within the Ronne polynya region of the WSRM which we show in fig. 6.8. Red dots represent simulations that reach a warm FRIS cavity steady-state, and blue dots represent simulations that reach a cold FRIS cavity steady-state.

or cold (blue) FRIS cavity is reached at the end of the simulation run-time. Fig. 4.19 justifies our assumption in equation (4.7) that integrated freshwater flux varies linearly as a function of cavity temperature. A linear regression between integrated freshwater flux versus the freezing temperature anomaly for the cold FRIS states explains 92% percent of the total variance of the results, while a linear regression in the warm state explains 98% of the results. Based on the linear relation shown in fig. 4.19, the values for the constants C_{melt} and Σ_{melt_o} from equation (4.7) are

$9.6\times10^{8}\frac{g}{s*K}$ and $5.1\times10^{7}\frac{g}{s}$, respectively.

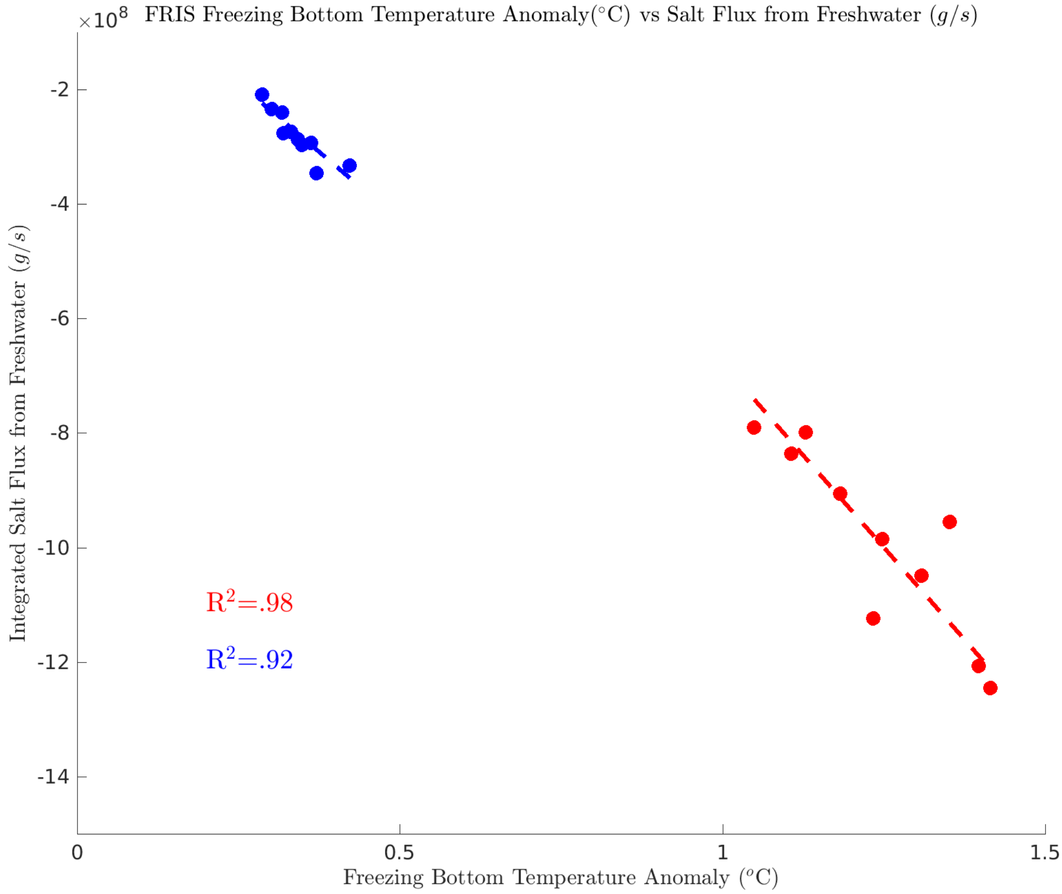

Figure 4.19: Melt-weighted cavity temperature anomaly (°C) versus integrated salt flux from freshwater (g/s), expressed as a negative salt flux, plotted for each offshore wind perturbation experiment. Values are calculated from the last 9-year full WSRM atmospheric forcing period. Red dots represent simulations that reach a steady state warm FRIS cavity, and blue dots represent simulations that reach a steady state cold FRIS cavity.

4.5.3 Solutions to Conceptual Model Equations

The offshore wind experiments determine that between a perturbation in the offshore winds of .7–1.10, the FRIS is bi-stable with both warm and cold cavity states co-occurring. In this section, expressions are derived from equations defined in §4.5.1 to arrive at theoretical solutions for FRIS bi-stability. Our solutions presented in this chapter are given primarily for illustrative purposes, but these solutions will also demonstrate the potential to solve for FRIS bi-stability from a more formal approach.

We begin with solving for the lower and upper limits of offshore wind strength, V_{lower} and V_{upper}, over which the FRIS cavity is bi-stable. Since we postulate that the density of CDW and HSSW is key in determining the state of the FRIS cavity, we write the equations of state to arrive at expressions for the density of CDW and HSSW as follows:

$$\sigma_{HSSW}\left(S,\theta,p_{ref}\right) \approx \rho_{ref}\left[1+\beta(S_{HSSW}-S_{ref})\alpha(\theta_{HSSW}-\theta_{ref})\right], \tag{4.11}$$

$$\sigma_{CDW}\left(S,\theta,p_{ref}\right) \approx \rho_{ref}\left[1+\beta(S_{CDW}-S_{ref})-\alpha(\theta_{CDW}-\theta_{ref})\right]. \tag{4.12}$$

To express the difference between σ_{HSSW} and σ_{CDW}, we combine equations (4.11) to arrive at the following expression:

$$\sigma_{HSSW}-\sigma_{CDW} \approx \rho_{ref}[\beta\left(S_{HSSW}-S_{CDW}\right)-\alpha\left(\theta_{HSSW}-\theta_{CDW}\right)]. \tag{4.13}$$

From equation (4.13), we can solve for the cold FRIS cavity condition where $\sigma_{HSSW} > \sigma_{CDW}$:

$$S_{HSSW} > S_{CDW} + \frac{\alpha}{\beta}\left(\theta_{HSSW}-\theta_{CDW}\right). \tag{4.14}$$

From equation (4.3), $\Delta S_{polynya}$, S_{AASW}, and ΔS_{melt} are substituted for S_{HSSW}. The resulting expression for the cold cavity condition is written as follows:

$$\begin{aligned}\Sigma_{polynya_o} - \Sigma_{melt_o} + C_{polynya}V_a - C_{melt}\left(\theta_{cavity}-\theta_f\right)&\\ > \rho_{ref}\psi\left[\left(S_{CDW}-S_{AASW}\right)+\frac{\alpha}{\beta}\left(\theta_{HSSW}-\theta_{CDW}\right)\right]&.\end{aligned} \tag{4.15}$$

After arriving at the above expression in equation (4.15) for the condition of a HSSW-controlled cavity, we solve for the lower limit in the offshore wind strength where the density of HSSW is greater than that of CDW. We rearrange equation 4.15 to arrive at the expression for V_{lower}:

$$\begin{aligned}V_{lower} = \frac{1}{C_{polynya}}\{\rho_{ref}\psi\left[\left(S_{CDW}-S_{AASW}\right)+\frac{\alpha}{\beta}\left(\theta_{HSSW}-\theta_{CDW}\right)\right]&\\ +C_{melt}\left(\theta_{HSSW}-\theta_f\right)-\Sigma_{polynya_o}+\Sigma_{melt_o}\}&.\end{aligned} \tag{4.16}$$

Equation (4.16) stipulates that for offshore wind speeds at strengths below V_{lower}, the density of CDW is always be greater than that of HSSW, and the FRIS cavity remains CDW-controlled.

Equations (4.14) and (4.15) can likewise be solved for the upper limit in the offshore wind strength where a warm cavity condition can exist; this gives an expression for V_{upper} as follows:

$$V_{upper} = \frac{1}{C_{polynya}} \{ \rho_{ref} \psi \big[\big(S_{CDW} - S_{AASW} \big) + \frac{\alpha}{\beta} \big(\theta_{HSSW} - \theta_{CDW} \big) \big] + C_{melt} \big(\theta_{CDW} - \theta_f \big) - \Sigma_{polynya_o} + \Sigma_{melt_o} \}. \quad (4.17)$$

Above the offshore wind strength corresponding to V_{upper}, HSSW remains denser than CDW, and the FRIS cavity is likewise HSSW-controlled. The expressions for V_{upper} and V_{lower} in equations (4.16) and (4.17) also suggest that FRIS bi-stability will exist when the offshore wind speed, V_a, falls within the range of V_{upper} and V_{lower}:

$$V_{lower} < V_a < V_{upper}. \quad (4.18)$$

Between wind strengths of V_{upper} and V_{lower}, the FRIS cavity state is determined from the initial cavity condition; a transition between warm and cold cavity states cannot occur.

The expression for the cavity density in equation (4.13) implies that a critical value of θ_{cavity} acts as a threshold for the existence of a warm or cold FRIS cavity state. We name this variable $\theta^\star$ and solve for the condition where σ_{CDW} is equal to σ_{HSSW}:

$$\theta^\star = \theta_f + \frac{1}{C_{melt}} \{ S_{AASW} + C_{polynya} V_a + \Sigma_{polynya_o} - \Sigma_{melt_o} - \rho_{ref} \psi \big[S_{CDW} + \frac{\alpha}{\beta} \big(\theta_{HSSW} - \theta_{CDW} \big) \big] \}. \quad (4.19)$$

Equation (4.19) shows that $\theta^\star$ is a function of the strength of the offshore wind. $\theta^\star$ must be greater than θ_{HSSW} in order for the FRIS cavity to exist in a cold state. In other words, the offshore-wind controlled $\theta^\star$ is the maximum temperature below which θ_{HSSW} will be found within the cavity. If θ_{HSSW} is greater than $\theta^\star$, the melt production in the cavity will lighten HSSW to the extent that CDW will become the denser water mass. On the other hand, $\theta^\star$ must be less than θ_{CDW} in order for CDW to flood the cavity. If θ_{CDW} is less than $\theta^\star$, meltwater production is too low to permit CDW to be denser than HSSW, and the FRIS cavity can remain in a cold, low-melt state. In order for $\theta^{\star}$ to permit a bi-stable FRIS cavity regime, its value must be between the temperatures of CDW and HSSW as follows:

$$\theta_{HSSW} < \theta^{\star} < \theta_{CDW}. \tag{4.20}$$

As in the value of V_a between V_{lower} and V_{upper} in equation (4.18), if $\theta^{\star}$ is within the bounds of equation (4.20), the FRIS cavity will not transition between warm and cold cavity states.

After arriving at expressions for V_{upper} and V_{lower}, we solve for their respective values with the constants listed in in table 4.2. Values of C_{melt}, $C_{polynya}$, $\Sigma_{polynya_o}$ and Σ_{melt_o} were derived in the analysis in §4.5.2.2 and §4.5.2.1. We use the control initial cold FRIS cavity state to calculate the values of $z^{\star}_{(Ice-Shelf)}$ from equation (4.8) and θ_f from equation (4.9), which give us values of $z^{\star}_{(Ice-Shelf)}$ and θ_f of -700m and -2.38∘C, respectively. α and β are calculated using the Gibbs Seawater Oceanographic toolbox (McDougall and Barker, 2011). A depth of 500m, an average temperature of θ_{CDW} and θ_{HSSW}, and a reference salinity of 34psu is used for this calculation. Values of S_{AASW} and ψ were chosen by constraining the calculated values of S_{HSSW} to the values of cavity S_{HSSW} from our experimental results. This is explained further in the Supporting Information in fig. 6.9, which shows the variation of the calculated cavity S_{HSSW} using the constants in table 4.2. Finally, values of θ_{HSSW} and θ_{CDW} were computed from the average temperature anomalies from θ_f in the steady-state cold and warm FRIS cavity experiments shown in fig. 4.19.

The calculated values for V_{lower} and V_{upper} from equations (4.16) and (4.17) are $1.55m/s$ and $3.91m/s$, respectively, which equate to χ values of .60 and 1.45. In addition to calculating the offshore wind limits to cavity bi-stability, we use equation (4.7) to find the upper and lower limits in integrated melt rate in both the warm and cold cavity states. A cavity temperature of θ_{CDW} of $\approx$ -1°C in the warm FRIS cavity state produces an average melt rate of $\approx$ 1100 (Gt/yr). For the cold FRIS cavity, a cavity temperature with properties of θ_{HSSW}, $\approx$ -2.1°C, yields a melt rate of $\approx$ 220(Gt/yr). Fig. 4.20 re-plots the integrated shelf ice melt presented in fig. 4.10 with the calculated superimposed limits of V_{lower} and V_{upper}.

The solutions of the conceptual model capture the essence of FRIS cavity bi-stability. The conceptual model's simple framework has the quantitative power to offer a crude approximation of the wind limits that allow for a bi-stable cavity. Future work will aim to more formally quantify the

Table 4.2: Constants Used for Conceptual Model Solutions

Parameter	Description	Value
$C_{polynya}$	Constant for the polynya salt flux	$4.0\times10^{8}\ \frac{g}{m}$
C_{melt}	Constant for the salt flux from freshwater production	$9.6\times10^{8}\frac{g}{s*K}$
$\Sigma_{polynya_o}$	Initial polynya salt flux	$-1.4\times10^{8}\ \frac{g}{s}$
Σ_{melt_o}	Initial salt flux from freshwater	$5.1\times10^{7}\frac{g}{s}$
α	Thermal expansion coefficient	6.6e-5 K^{-1}
β	Haline contraction coefficient	7.6e-4 psu^{-1}
ψ	Transport	2.2 Sv
S_{ref}	Reference salinity	34psu
ρ_{ref}	Reference density	1000 kg/m^3
S_{AASW}	Salinity of AASW	34.2psu
S_{CDW}	Salinity of CDW	34.35 psu
θ_{CDW}	Temperature of Cavity CDW	-1.1°C
θ_{HSSW}	Temperature of Cavity HSSW	-2.08°C

values of the constants of the conceptual model equations. To this extent, a water mass transformation analysis in density coordinates could diagnose the variation S_{HSSW} and S_{CDW} in the FRIS cavity given perturbations to offshore wind strength. This analysis would offer a more quantitative approach to defining the region over which HSSW formation occurs and more accurately define the constant $C_{polynya}$.

4.6 Conclusion

In this chapter, we explore the sensitivity of the FRIS cavity circulation, water mass properties, and meltwater production to the pre-existing FRIS cavity conditions. We discover that initial density determines whether the FRIS cavity enters a steady-state warm, high-melt or cold, low-melt regime. A restoring of the initial cavity salinity to a value of 34psu leads to a warm steady-

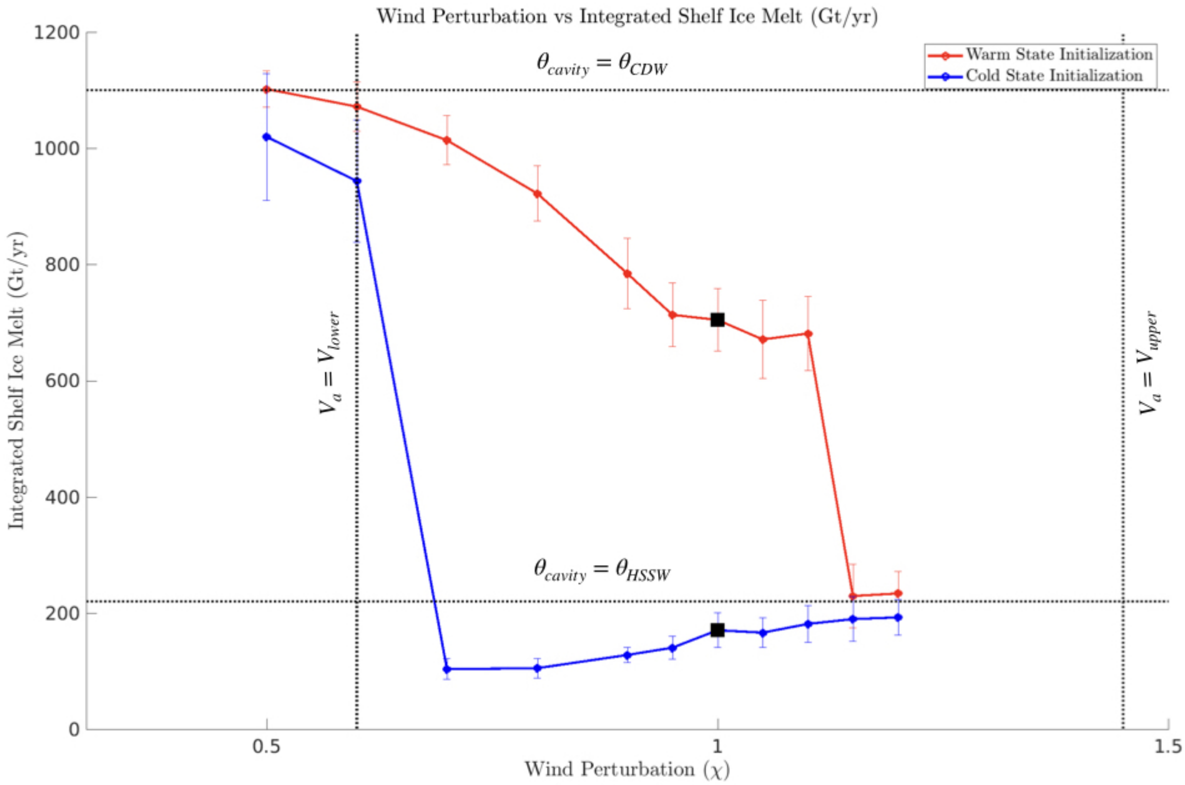

Figure 4.20: Wind perturbation (χ) versus integrated shelf ice melt (Gt/yr). Values represent the monthly mean average over the last 9-year full WSRM atmospheric forcing period from experiments initialized with either a warm (red) or cold (blue) initial FRIS cavity state. Solutions for V_{upper} and V_{lower} limits are represented with vertical black dotted lines, corresponding to the limit of $V_a = V_{upper}$ and $V_a = V_{lower}$, respectively. Horizontal dotted black lines denote our predicted melt rates for the warm and cold FRIS cavity states, corresponding to the condition of $\theta_{cavity} = \theta_{CDW}$ or $\theta_{cavity} = \theta_{HSSW}$, respectively.

state, while a denser cavity-restoring of 34.45psu gives a cold steady-state FRIS cavity. After establishing the existence of two FRIS cavity steady-state circulations, we explore the potential to transition between warm and cold states. From experimentation, we find that perturbations of a few tens of percent to the offshore winds allows the FRIS cavity to switch between cold and warm steady state circulations. Above a 15% increase in the offshore wind strength, the FRIS cavity remains cold and HSSW-controlled, regardless of the initial cavity condition. In contrast, when the offshore wind strength is reduced by 40%, the FRIS cavity remains warm and CDW-controlled.

The offshore wind perturbations experimentally determine the range of FRIS cavity bi-stability between offshore wind perturbations of -30% – +10%, for which steady-states can co-occur with an order of magnitude change in melt between them. In this range of offshore wind strength, FRIS cavity circulation, melt rate, and water mass properties are determined from the initial cavity stratification.

To further validate the experimental results, we develop a conceptual model to illustrate the mechanisms involved in FRIS cavity bi-stability. Using carefully chosen constants, V_{lower} and V_{upper} limits to bi-stability are calculated to be $1.55 m/s$ and $3.91 m/s$, respectively, which equate to offshore wind perturbations of -40% and +45%, respectively. In future work, a first-principles approach to the solutions will be developed. For instance, explicit pathways and properties of HHSW will be quantified using a water mass transformation calculation to arrive at more formal definitions of the constants $C_{polynya}$, S_{CDW}, and S_{HSSW}. Overall, the findings presented in this chapter imply that climatic changes may have significant impacts for near-Antarctic ice shelf melt rates. Given a transition of ice shelves to a high-melt regime, it would be unlikely to return to s state of low melt.

CHAPTER 5

Conclusion and Future Work

In this work, we highlight the importance of the wind-driven near-Antarctic Circulation. Near-Antarctic circulation is fundamental for global ocean freshwater, heat, and tracer exchange as well as the closure of the meridional overturning circulation, which ventilates the deep ocean with 0_2 and takes up atmospheric CO_2. In addition, the response ocean-ice sheet interactions to climate change could alter the important processes near Antarctica and dictate future levels of sea level rise. Our work focuses on the changes to the climate of Antarctica from an increase in the positive index of the SAM.

We quantified recent changes in near-Antarctic surface forcing in §2 in our calculation of the trend in the along-slope multi-decadal wind stress. In this study, we found that the easterlies have strengthened by $.0044\,\mathrm{N\,m^{-2}}$, or by around 7%, though this trend was not statistically significant. This trend in the easterlies corresponded to an anomalous shoreward Ekman transport of around 0.6 Sv around the $\sim$18,000km length of the Antarctic shelf break. However, the wind stress exhibited substantial seasonal trends that further strengthened its seasonality. In DJF and MAM, the easterlies weakened by $.0055\,\mathrm{N\,m^{-2}}$ (12%) and $.0022\,\mathrm{N\,m^{-2}}$ (3%), equivalent to offshore Ekman transport anomalies of approximately 0.7 Sv and 0.3 Sv, respectively. In JJA and SON, the easterlies strengthened by $.0112\,\mathrm{N\,m^{-2}}$ (15%) and $.0143\,\mathrm{N\,m^{-2}}$ (22%), equivalent to shoreward Ekman transport anomalies of 1.5 Sv and 1.9 Sv, respectively. The quantified trends have widespread implications for regional processes, including dense water formation, and may influence water mass properties and regional melt rates.

The trends in the near-Antarctic surface forcing motivated the development of a regional model of the Weddell Sea (WSRM) using MITgcm framework The WSRM region includes the adjacent Filchner-Ronne Ice Shelf (FRIS), Antarctica's largest floating glacier, and an upstream portion of the Weddell gyre. The WSRM currently runs at $\frac{1}{3}^{\circ}$ horizontal resolution and has 139 vertical levels. Tides, static shelf ice, and thermodynamic-dynamic sea ice are parameterized to achieve water mass properties and circulation patterns that mimic those in observations. We implemented observational tools, including as CTD sections and satellite data, to validate the WSRM; we found that the WSRM sea ice state, temperature, and salinity properties compare well with observations. We plan to refine the WSRM further to an eddy-permitting resolution of $\mathscr{O}(1\text{km})$. This resolution is required to resolve small-scale processes involved in the transport of heat across the shelf break (Thoma et al., 2008) and the closure of the overturning circulation (Stewart and Thompson, 2012).

Motivated by research suggesting that the FRIS cavity will enter a state of high melt in future climate scenarios (Hellmer et al., 2012; Hellmer et al., 2017), we investigated the steady state FRIS cavity circulation and the factors that control the propensity to meltwater intrusion into the cavity. From experimentation with initial WSRM cavity restoring, we discovered two distinct FRIS cavity steady-states, governed by the pre-existing cavity density; these states were characterized by either a "warm" (high-melt) or a "cold" (low-melt) FRIS cavity. We investigated the potential to transition between these states with a series of surface forcing perturbations to the WSRM. We found that the FRIS cavity is sensitive to changes in the offshore wind strength but rather insensitive to changes in the zonal winds and atmospheric temperature. Future work will involve a more thorough array of perturbation experiments to the atmospheric temperature and zonal wind in addition to the experiments shown at present.

With changes to the strength of the offshore meridional winds of only a few tens of percent, the FRIS cavity transitioned from a warm steady-state to a cold steady-state, and vice-versa. We empirically determined that at a value of χ between .7–1.10, both cold and warm bi-stable states co-exist, with an order of magnitude difference in melt between them. At an offshore wind perturbation at or greater than +15%, the FRIS cavity steady state remained cold and HSSW-controlled, whereas at or below a wind perturbation of .6, only a warm, CDW-controlled FRIS cavity state existed. With perturbations to the offshore wind between -30–+10%, the FRIS cavity state is determined by the initial cavity stratification. A cold, dense cavity buffers against warm, CDW intrusions, whereas a fresh cavity allows persistent pathways of CDW to enter the cavity and anomalously high melt rates.

A conceptual model was developed from a simple framework to solve for the offshore wind range that permits a FRIS cavity bi-stable state. The fundamental component of the conceptual model is that FRIS steady-state cavity circulations remains warm when CDW preferentially enters the cavity over HSSW; this occurs when the density of CDW is greater than that of HSSW. In contrast, the FRIS cavity exists in a cold steady-state when HSSW has a higher density than CDW. Using the equation of state, solutions for the values of V_{lower} and V_{upper} of $1.55 m/s$ (-40%) and $3.91 m/s$ (+45%) were found that closely match the limits found in experimental results. Future work will be done to arrive at solutions to the conceptual model with more formally derived constants, which will involve quantifying the overturning circulation and exploring the pathways and transformation of CDW and HSSW.

This thesis motivates various future directions and research on the subject of wind-driven near-Antarctic circulation. One such direction surrounds the application of the WSRM framework to other regions along the Antarctic coast. The WSRM is written in a generalized fashion and can be adapted to fit other ice-shelf ocean regions around Antarctica to explore whether the bi-stable tendency of the FRIS cavity is applicable elsewhere.

In a broader sense, the research presented in this thesis highlights the importance of an enhanced observational effort around Antarctica, especially within ice shelf cavities. Various observational efforts have already been made; for example, Kobs et al. (2014) demonstrate an improvement to the employment of bore-holes to continuously monitor ocean and ice shelf temperatures to a depth of $\approx$ 800m below the McMurdo Ice Shelf. Novel observational techniques, including autonomous vehicles (Heywood et al., 2014) and seals (Hattermann et al., 2012), have provided more insight into spatial and temporal variability around the Antarctic margins. Given the complexity of ice-ocean interaction within distinct ice shelves along the Antarctic coast, it is necessary to prolong these observational efforts and extend them to other ice shelf cavity regimes to better understand ice-ocean interactions and ice shelf stability. Overall, a greater observational effort of the physical properties and mechanisms around Antarctica will improve modeling efforts, which is a fundamental step forward towards prediction.

CHAPTER 6

Appendix

6.1 Chapter 2

In addition to the wind stress trend comparison with CFSR, JRA-55, and MERRA, we performed an additional comparison between ERA-Interim (Dee et al., 2011) and the NCEP reanalysis product (Saha et al., 2010). Fig. 6.1 shows the multi-decadal trend in the wind stress in the NCEP-NCAR 40-year reanalysis product, which is the source of the wind stress in the widely-used CORE.v2 dataset (Large, McWilliams, and Doney, 1994). The multi-decadal trends are broadly similar in NCEP and ERAInterim, but the trends in NCEP are spuriously large (Hines, Bromwich, and Marshall, 2000). For this reason, we keep the NCEP comparison apart from the main analysis.

6.2 Chapter 3

In §3.4, WSRM results are validated against observational data from various sources. We provide a visual reference in the bottom of fig. 6.2 for the locations of the A12 and SR4 WOCE CTD transects (Schlitzer, 2002). In addition, we note the location of the Kappa Norvegia transect (Hattermann, 2018) in the bottom panel of fig. 6.2.

6.3 Chapter 4

6.3.1 34.9psu Initial FRIS Cavity

In §4, we explore the dependence of FRIS circulation, water mass properties, and melt rate on the strength of the pre-existing FRIS cavity stratification. Two experiments are analyzed with a FRIS

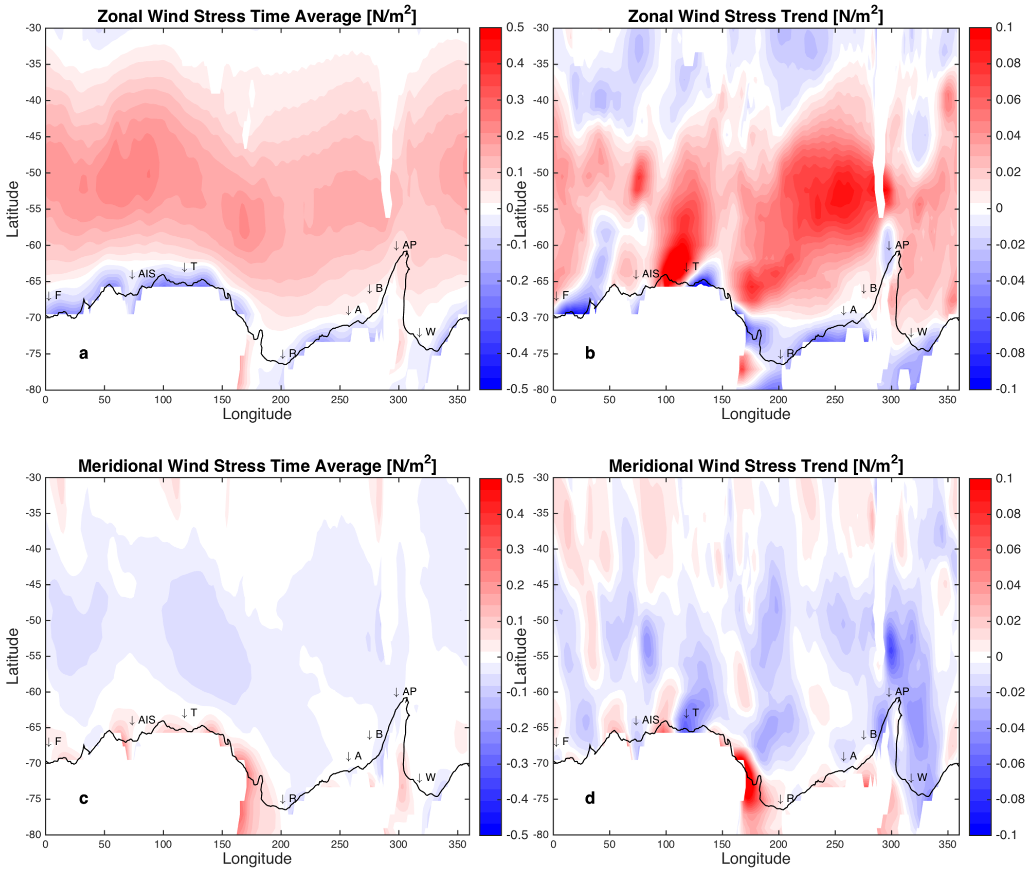

Figure 6.1: 1979-2014 mean and trend of the zonal and meridional wind stress in NCEP. (a) Mean zonal wind stress, (b) trend in the zonal wind stress, (c) mean meridional wind stress and (d) trend in the meridional wind stress.

cavity restoring to salinities of 34.45psu and 34psu. In addition to the two FRIS cavity restoring experiments analyzed in in §4.2, we performed an additional experiment with a FRIS cavity restoring to 34.9psu. In this section, we present additional analysis regarding this experiment.

In fig. 6.3, time-series of integrated ice shelf melt for the 34psu,34.45psu, and 34.9psu FRIS cavity restoring experiments are given. Note that the 34.9psu case follows roughly the same pattern of low melt as in the 34.45psu cavity restoring. As discussed in §4, the 34psu case reveals a high melt (800Gt) that diverges from the other initialization experiments. To delve further into the differences in the water mass properties between the 34.9psu case and the 34.45psu case, we plot

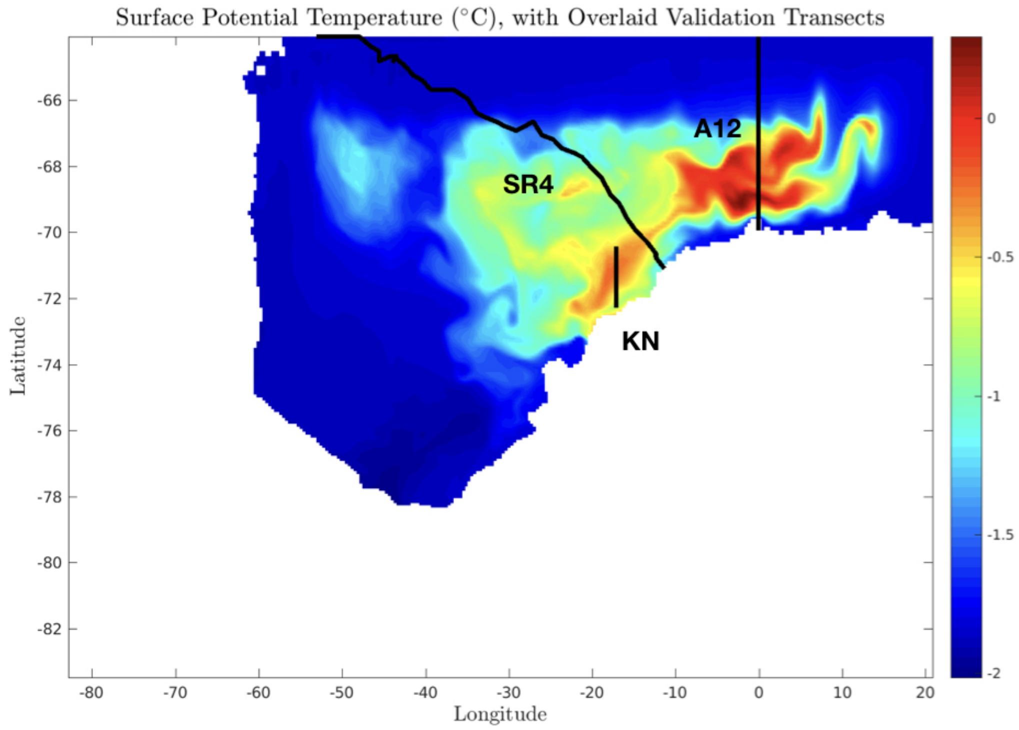

Figure 6.2: 9-year averaged surface potential temperature (°C), overlaid with the approximate locations of the Kapp Norvegia validation transect (Hattermann, 2018) as well as the SR4 and A12 WOCE transects (Schlitzer, 2002). We validate the temperature and salinity properties in the WSRM along these CTD transects in §3.4

time-series of mean bottom temperature (°C) and mean bottom salinity (psu) in all three runs in figs. 6.4 and 6.5, respectively. In these time-series, temperature and salinity values are from gridcells with positive melt rates. These values are then weighted by the amount of meltwater production within each gridcell (see equations (4.1a) and (4.1b)). In addition, we plot the 34.9psu T/S properties in fig. 6.6.

In Fig. 6.5, the 34.9psu initialization experiment has a higher average bottom salinity than in the 34.45psu experiment. The high salinity anomaly persists for 18 years after the initial relaxation period, which suggests that the initial density of the cavity in the 34.9 case is too high to be flushed by either HSSW or CDW. The water mass properties also show remnants of the initialized 34.9psu

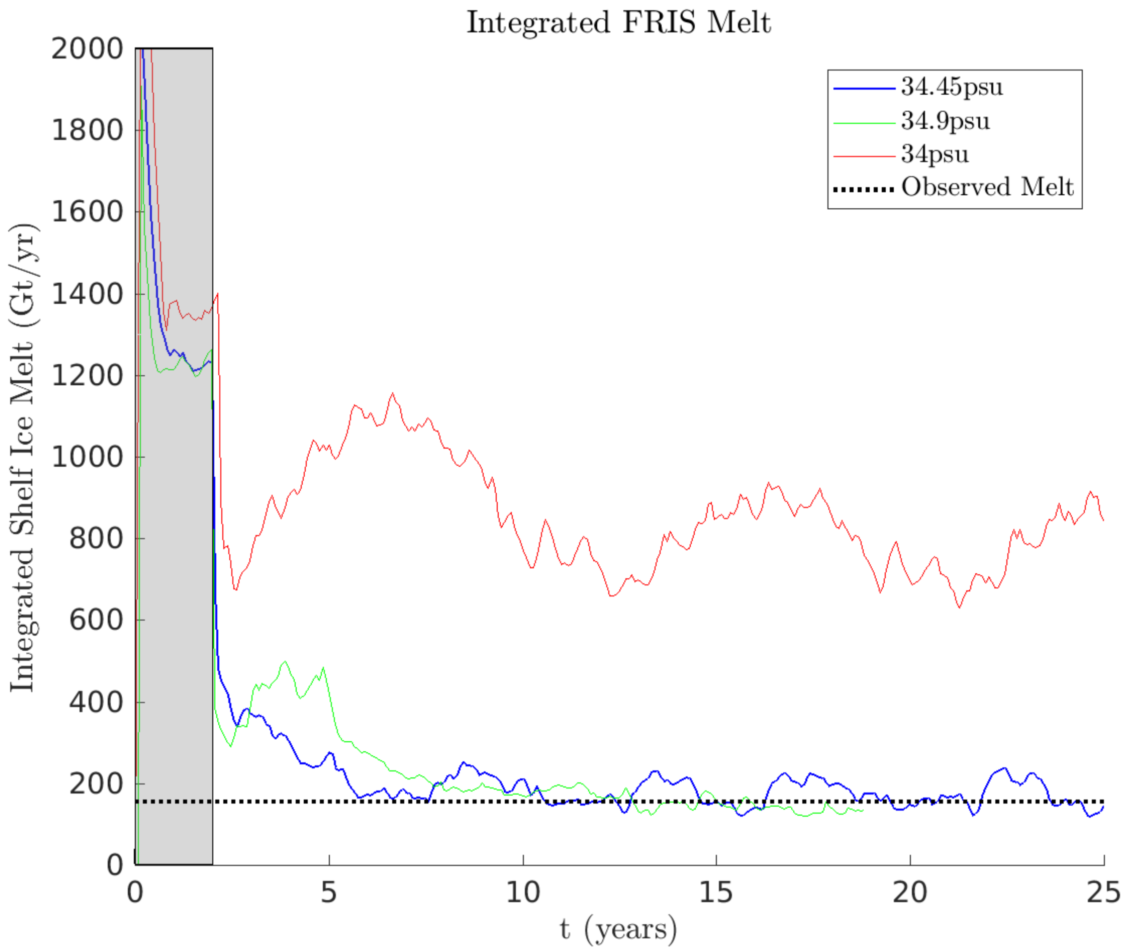

Figure 6.3: Integrated FRIS melt (Gt) time-series for the 34psu (red), 34.45psu (blue), and 34.9psu (green) initial FRIS cavity restoring experiments. The shaded portion of the figure in gray corresponds to the two-year restoring period of FRIS cavity properties at the start of each respective run. The dotted black line corresponds to the observed FRIS melt (Rignot et al., 2013).

salinity in Fig. 6.6.

The 34.9psu FRIS cavity initialization experiment is omitted from the main analysis in §4. The choice of restoring the FRIS cavity to the initial salinity of 34.9psu leads to an artificially high initial FRIS cavity density. This initial dense water within the cavity cannot be "flushed" on timescales of 30–40 years. Therefore, we choose not include this experiment in the main text in §4.

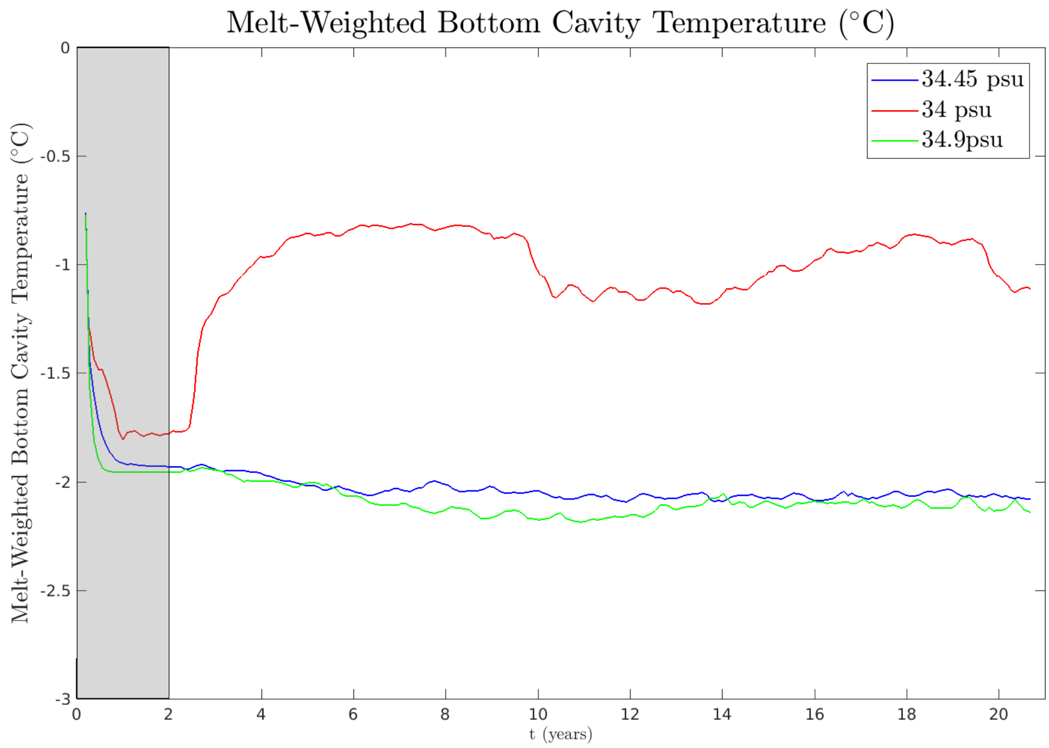

Figure 6.4: Time-series of melt-weighted cavity bottom temperature for the 34psu (red), 34.45psu (blue), and 34.9psu (green) initial FRIS cavity restoring experiments. Temperature values are extracted from grid cells with positive melt rate and normalized by weighting temperature values by the requisite amount of freshwater flux in each gridcell (see equation (4.1b)). The shaded region corresponds to the 2-year restoring period of FRIS cavity properties at the start of each run.

6.3.2 Length of Offshore Wind Perturbation Experiments

In table 6.1, we provide the model run times for each of the offshore wind perturbation experiments. The diagnostics analyzed in §4 are averaged over the last complete 9-year WSRM atmospheric forcing cycle.

6.3.3 FRIS Analysis Region

The bulk of §4 focuses on the analysis of FRIS integrated ice shelf melt rates and FRIS water mass property analysis. For clarity, we highlight the FRIS region in fig. 6.7.

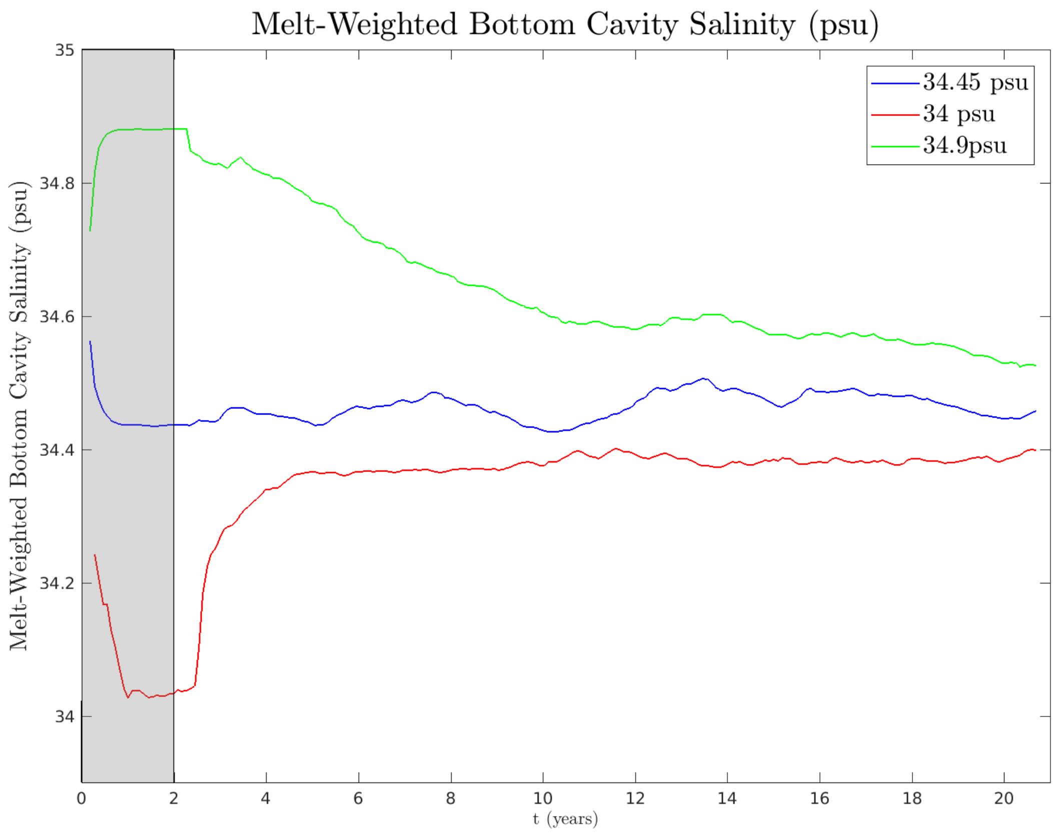

Figure 6.5: Time series of FRIS cavity bottom salinity for the 34psu (red), 34.45psu (blue), and 34.9psu (black) initialization experiments. Salinity values are taken from WSRM gridcells with positive melt rate and normalized by weighting the salinity values by the requisite amount of freshwater flux in each gridcell (see equation (4.1a)). The shaded region represents the two-year relaxation period of the FRIS cavity properties at the start of each run.

6.3.4 Ronne Polynya Analysis Region

We analyze the relationship between experimental offshore wind speed and integrated salt flux within the Ronne Polynya region in §4. This region is highlighted in gray for clarity in fig. 6.8. The highlighted region is superimposed upon the average winter (JJA) salt flux in our control 34.45psu initialization case simulation. The salt flux data is seasonally averaged in winter over the last complete 9-year atmospheric forcing cycle. The geographical limits for this region are based on those used by Haid and Timmermann (2013). We define this region as extending zonally from

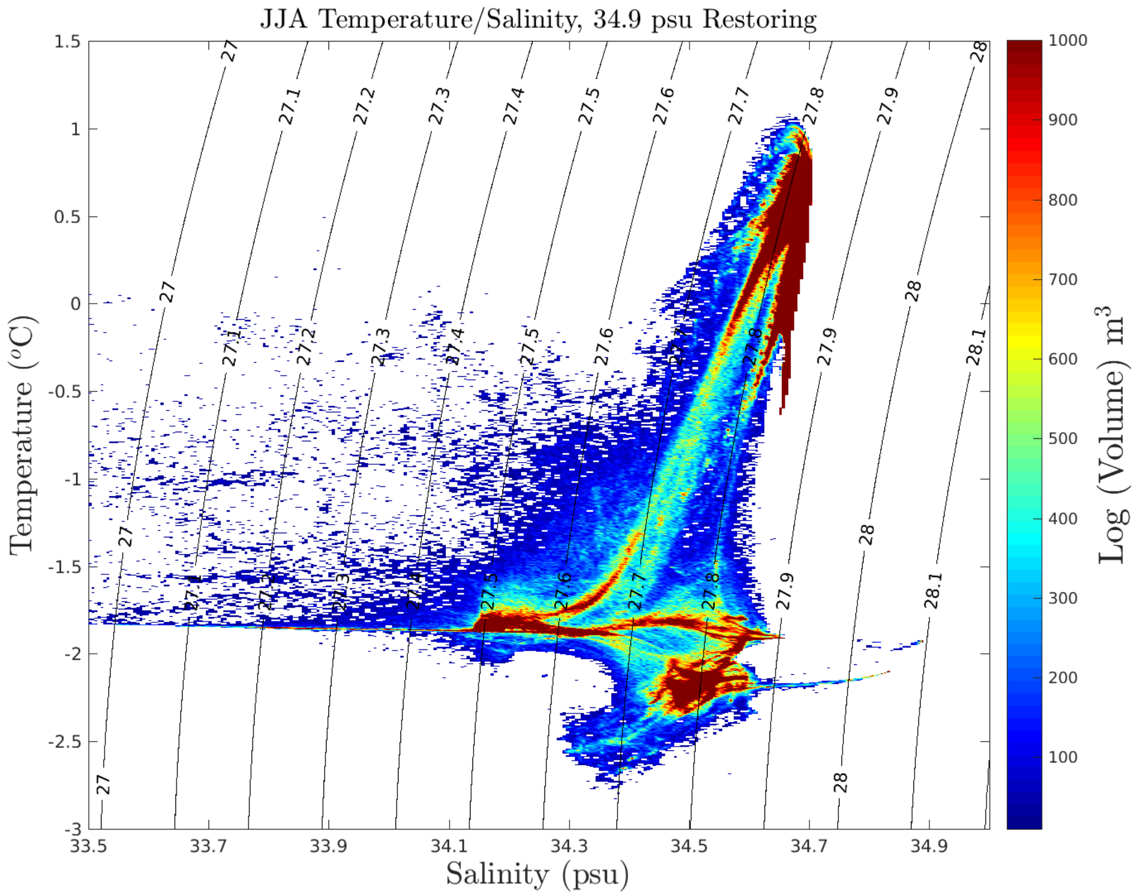

Figure 6.6: JJA Temperature/Salinity properties taken from the 34.9psu FRIS cavity restoring experiment. Values are averaged over the last complete 9-year atmospheric forcing cycle of the simulation and binned by log(Volume). Surface-referenced potential density is overlaid in black contours and spaced at .1kgm^{-3}.

45°W westward to the coastline. The region extends several kilometers off the shelf in order to capture the region of highest salt production.

6.3.5 Constraining Values of Constants in Conceptual Model Solutions

Values of ψ and S_{HSSW} to solve V_{upper} and V_{lower} from the conceptual model equations (4.16) and (4.17) were constrained to fit the experimentally determined values of cavity S_{HSSW} shown in fig. 4.12. In fig. 6.9, we re-plot fig. 4.12 with the values of calculated cavity S_{HSSW} given changes

Table 6.1: List of offshore wind experiments and their respective run-times in model years

χ	Duration (model years) Initial Cold Cavity	Duration (model years) Initial Warm Cavity
.5	30	18
.4	36	20
.3	18	20
.2	20	20
.1	20	20
.05	20	20
0	36	25
1.05	20	20
1.1	20	20
1.15	20	28
1.2	20	36

in the offshore wind perturbation, χ. S_{HSSW} is calculated re-writing equation 4.13 as follows:

$$S_{HSSW} = S_{AASW} + \frac{1}{\rho_{ref}\psi}\left(\rho_{ref} + C_{polynya}V_a - \Sigma_{melt_o} - C_{melt}\left(\theta_{HSSW} - \theta_f\right)\right)$$

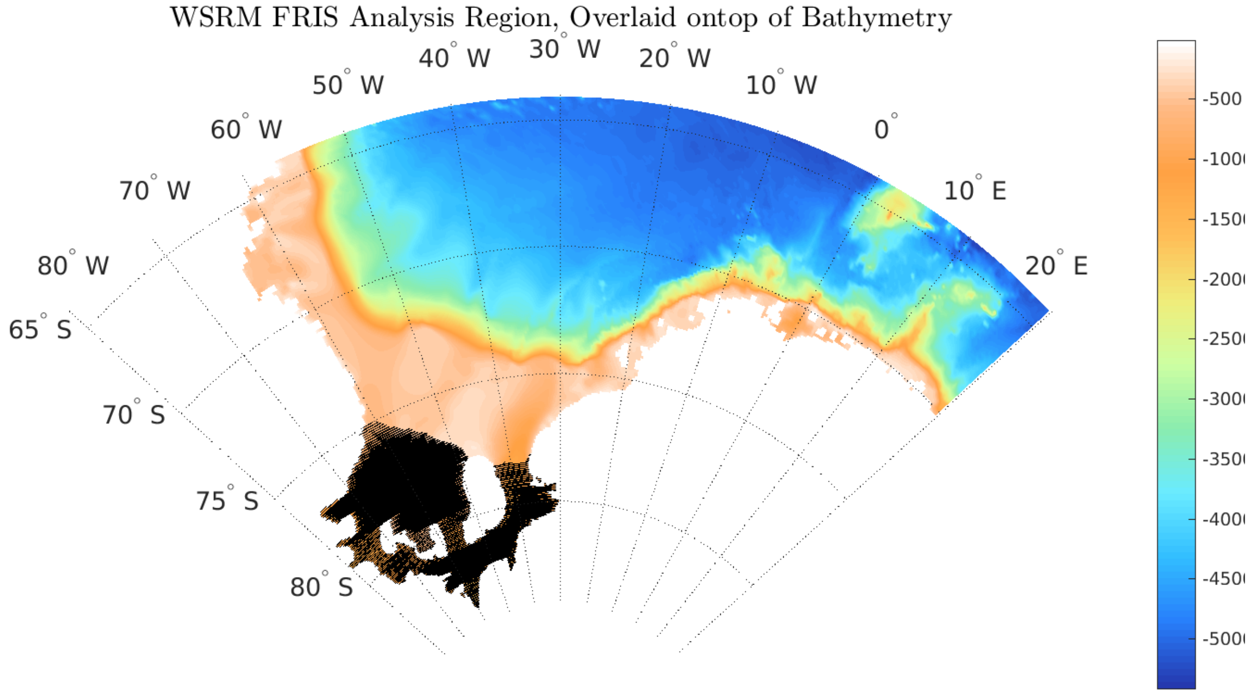

Figure 6.7: Weddell Sea model domain, contoured according to bathymetry. Our defined FRIS region is highlighted with black stippling.

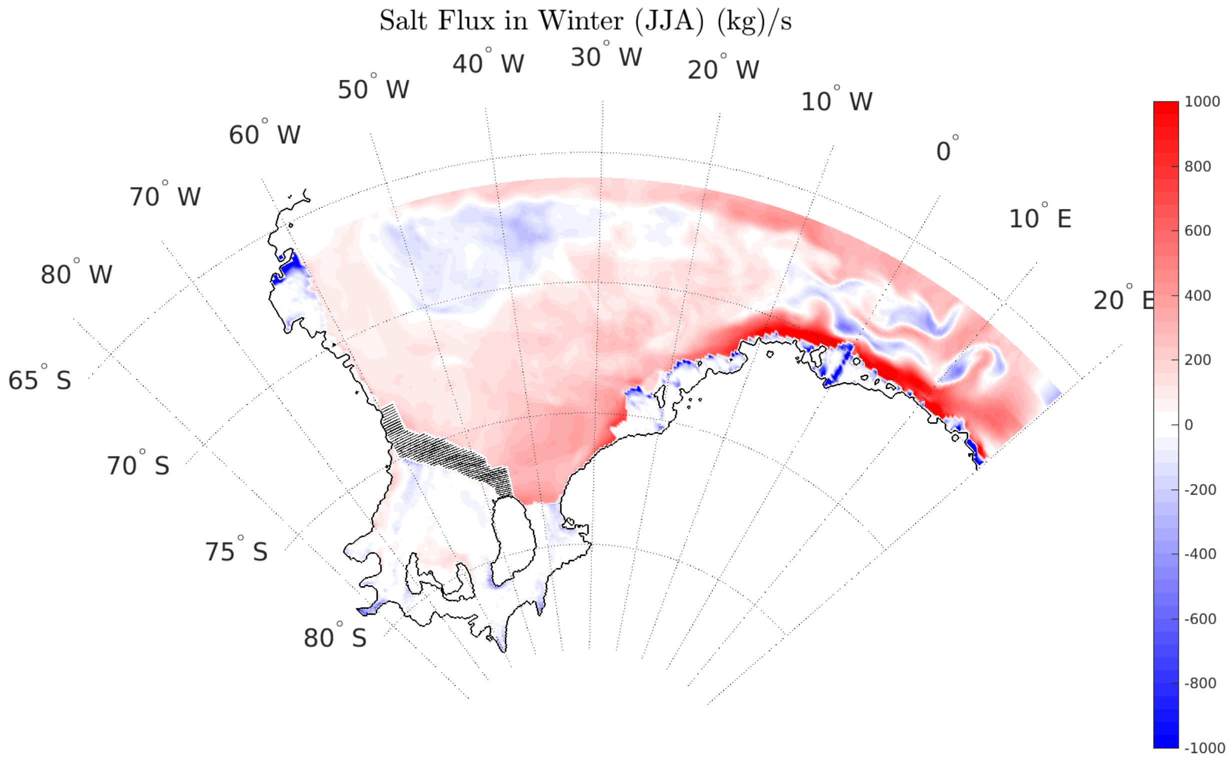

Figure 6.8: JJA integrated salt flux (kg/s) across the WSRM domain. Values are seasonally averaged over the last full 9-year atmospheric forcing cycle. Overlaid in gray hatching is the Ronne Polynya analysis region.

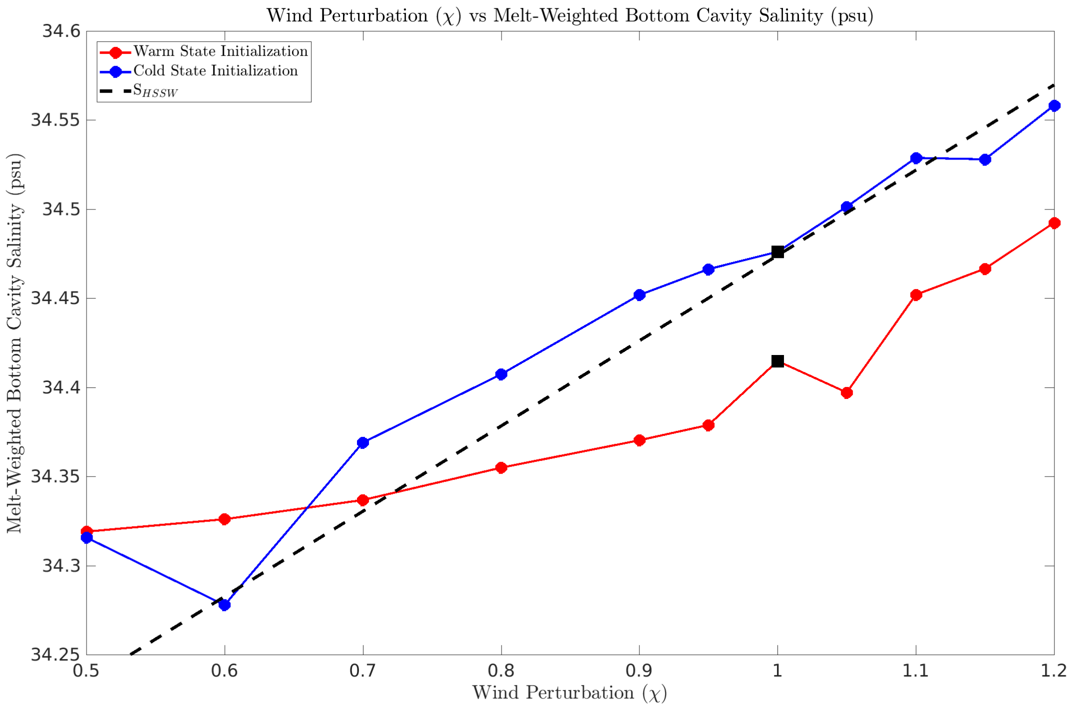

Figure 6.9: Wind perturbation versus melt-weighted FRIS cavity salinity (psu). Values represent monthly mean averages from the last 9-year full WSRM atmospheric forcing period in each run. Experiments are initialized from either a warm (red dots) or cold (blue dots) initial FRIS cavity state. Data is extracted from the FRIS cavity region of the WSRM domain shown in the Supporting Information in fig. 6.7. Plotted bottom salinity values are normalized by weighting the salinity values in gridcells with positive melt against the total freshwater flux within each respective gridcell (see equation (4.1a)). Black squares represent the control runs from the cold and warm initial FRIS cavity states. The overlaid black dotted line refers to the value of S_{HSSW} calculated from equation (6.3.5) with the constants given in table 4.2.

Bibliography

Adcroft, A., C. Hill, and J. Marshall (1997). “Representation of topography by shaved cells in a height coordinate ocean model”. In: *Monthly Weather Review* 125.9, pp. 2293–2315.

Amante, C. and B. W. Eakins (2009). *ETOPO1 1 Arc-Minute Global Relief Model: Procedures, Data Sources and Analysis*. US Department of Commerce, National Oceanic et al.

Amblas, D. and J. A. Dowdeswell (2018). “Physiographic influences on dense shelf-water cascading down the Antarctic continental slope”. In: *Earth-Sci. Rev.*

Andreas, E. L. (1995). “Air-ice drag coefficients in the western Weddell Sea: 2. A model based on form drag and drifting snow”. In: *Journal of Geophysical Research: Oceans* 100.C3, pp. 4833–4843.

Armitage, T. W. K. et al. (2018). “Dynamic topography and sea level anomalies of the Southern Ocean: Variability and teleconnections”. In: *Journal of Geophysical Research: Oceans* 123.1, pp. 613–630.

Beckmann, A., H. H. Hellmer, and R. Timmermann (1999). “A numerical model of the Weddell Sea: Large-scale circulation and water mass distribution”. In: *Journal of Geophysical Research: Oceans* 104.C10, pp. 23375–23391.

Bintanja, R. et al. (2014). “The future of Antarctica’s surface winds simulated by a high-resolution global climate model: 1. Model description and validation”. In: *Journal of Geophysical Research: Atmospheres* 119.12, pp. 7136–7159.

Bracegirdle, T. J. (2013). “Climatology and Recent Increase of Westerly Winds Over the Amundsen Sea Derived from Six Reanalyses”. In: *International Journal of Climatology* 33.4, pp. 843–851.

Bracegirdle, T. J. and G. J. Marshall (2012). “The Reliability of Antarctic Tropospheric Pressure and Temperature in the Latest Global Reanalyses”. In: *Journal of Climate* 25.20, pp. 7138–7146.

Bromwich, D. H. and R. L. Fogt (2004). “Strong trends in the skill of the ERA-40 and NCEP–NCAR reanalyses in the high and midlatitudes of the Southern Hemisphere, 1958–2001”. In: *Journal of Climate* 17.23, pp. 4603–4619.

Bromwich, D. H., J. P. Nicolas, and A. J. Monaghan (2011). "An Assessment of Precipitation Changes over Antarctica and the Southern Ocean since 1989 in Contemporary Global Reanalyses*". In: *Journal of Climate* 24.16, pp. 4189–4209.

Callahan, J. E. (1972). "The Structure and Circulation of Deep Water in the Antarctic". In: *Deep Sea Research and Oceanographic Abstracts*. Vol. 19. 8. Elsevier, pp. 563–575.

Clem, K. R. et al. (2016). "The relative influence of ENSO and SAM on Antarctic Peninsula climate". In: *Journal of Geophysical Research: Atmospheres* 121.16, pp. 9324–9341.

Comiso, J. C and A. L. Gordon (1998). "Interannual Variability In Summer Sea Ice Minimum, Coastal". In: *Antarctic Research Series* 74, pp. 293–315.

Daae, K. et al. (2017). "On the effect of topography and wind on warm water inflow: An idealized study of the southern Weddell Sea continental shelf system". In: *Journal of Geophysical Research: Oceans*.

Dansereau, V., P. Heimbach, and M. Losch (2014). "Simulation of subice shelf melt rates in a general circulation model: Velocity-dependent transfer and the role of friction". In: *Journal of Geophysical Research: Oceans* 119.3, pp. 1765–1790.

Darelius, E., I. Fer, and K. W. Nicholls (2016). "Observed vulnerability of Filchner-Ronne Ice Shelf to wind-driven inflow of warm deep water". In: *Nature communications* 7, p. 12300.

Darelius, E. et al. (2014). "Hydrography and circulation in the Filchner Depression, Weddell Sea, Antarctica". In: *Journal of Geophysical Research: Oceans* 119.9, pp. 5797–5814.

De Lavergne, C. et al. (2014). "Cessation of deep convection in the open Southern Ocean under anthropogenic climate change". In: *Nature Climate Change* 4.4, pp. 278–282.

De Rydt, J. et al. (2014). "Geometric and oceanographic controls on melting beneath Pine Island Glacier". In: *Journal of Geophysical Research: Oceans* 119.4, pp. 2420–2438.

Deb, P. et al. (2016). "An assessment of the Polar Weather Research and Forecasting (WRF) model representation of near-surface meteorological variables over West Antarctica". In: *Journal of Geophysical Research: Atmospheres*.

DeConto, R. M. and D. Pollard (2016). "Contribution of Antarctica to past and future sea-level rise". In: *Nature* 531.7596, p. 591.

Dee, D. P. et al. (2011). “The ERA-Interim Reanalysis: Configuration and Performance of the Data Assimilation System”. In: *Quarterly Journal of the Royal Meteorological Society* 137.656, pp. 553–597.

Dinniman, M. S., J. M. Klinck, and E. E. Hofmann (2012). “Sensitivity of Circumpolar Deep Water transport and ice shelf basal melt along the west Antarctic Peninsula to changes in the winds”. In: *Journal of Climate* 25.14, pp. 4799–4816.

Dinniman, M. S., J. M. Klinck, and W. O. Smith (2011). “A Model Study of Circumpolar Deep Water on the West Antarctic Peninsula and Ross Sea Continental Shelves”. In: *Deep Sea Research Part II: Topical Studies in Oceanography* 58.13, pp. 1508–1523.

Dinniman, M. S. et al. (2016). “Modeling ice shelf/ocean interaction in Antarctica: A review”. In: *Oceanography* 29.4, pp. 144–153.

Döös, K. and D. J. Webb (1994). “The Deacon cell and the other meridional cells of the Southern Ocean”. In: *Journal of Physical Oceanography* 24.2, pp. 429–442.

Dutrieux, P. et al. (2014). “Strong sensitivity of Pine Island ice-shelf melting to climatic variability”. In: *Science* 343.6167, pp. 174–178.

Ebert, E. E. and J. A. Curry (1993). “An intermediate one-dimensional thermodynamic sea ice model for investigating ice-atmosphere interactions”. In: *Journal of Geophysical Research: Oceans* 98.C6, pp. 10085–10109.

Fahrbach, E., G. Rohardt, and G. Krause (1992). “The Antarctic coastal current in the southeastern Weddell Sea”. In: *Polar Biology* 12.2, pp. 171–182.

Fer, I., E. Darelius, and K. B. Daae (2016). “Observations of energetic turbulence on the Weddell Sea continental slope”. In: *Geophysical Research Letters* 43.2, pp. 760–766.

Flexas, M. M. et al. (2015). “Role of tides on the formation of the Antarctic Slope Front at the Weddell-Scotia Confluence”. In: *J. Geophys. Res. Oceans* 120.5, pp. 3658–3680.

Foldvik, A. et al. (2004). “Ice shelf water overflow and bottom water formation in the southern Weddell Sea”. In: *Journal of Geophysical Research: Oceans* 109.C2.

Foldvik A., Gammelsrød T. Nygaard E. and S. Østerhus (2001). “Current measurements near Ronne Ice Shelf: Implications for circulation and melting”. In: *Journal of Geophysical Research: Oceans* 106.C3, pp. 4463–4477.

Foster, T. D. and E. C. Carmack (1976). “Frontal zone mixing and Antarctic Bottom Water Formation in the Southern Weddell Sea”. In: *Deep Sea Research and Oceanographic Abstracts*. Vol. 23. 4. Elsevier, pp. 301–317.

Fox, A. J., A. Paul, and R. Cooper (1994). “Measured properties of the Antarctic ice sheet derived from the SCAR Antarctic digital database”. In: *Polar Record* 30.174, pp. 201–206.

Gade, H. G. (1979). “Melting of ice in sea water: A primitive model with application to the Antarctic ice shelf and icebergs”. In: *Journal of Physical Oceanography* 9.1, pp. 189–198.

Gammelsrød, T. et al. (1994). “Distribution of water masses on the continental shelf in the southern Weddell Sea”. In: *The polar oceans and their role in shaping the global environment*, pp. 159–176.

Gelaro, R. et al. (2017). “The modern-era retrospective analysis for research and applications, version 2 (MERRA-2)”. In: *Journal of Climate* 30.14, pp. 5419–5454.

Gill, A. E. (1973). “Circulation and Bottom Water Production in the Weddell Sea”. In: *Deep Sea Research and Oceanographic Abstracts*. Vol. 20. 2. Elsevier, pp. 111–140.

Gille, S. T., D. C. McKee, and D. G. Martinson (2016). “Temporal Changes in the Antarctic Circumpolar Current: Implications for the Antarctic Continental Shelves”. In: *Oceanography* 29.4, pp. 96–105.

Gnanadesikan, A. and R. W. Hallberg (2000). “On the Relationship of the Circumpolar Current to Southern Hemisphere Winds in Coarse-Resolution Ocean Models”. In: *Journal of Physical Oceanography* 30.8, pp. 2013–2034.

Gordon, A., M. Visbeck, and B. Huber (2001). “Export of Weddell Sea deep and bottom water”. In: *Journal of Geophysical Research-Oceans* 106, pp. 9005–9017.

Gordon, A. L., B. A. Huber, and J. Busecke (2015). “Bottom Water Export from the Western Ross Sea, 2007 through 2010”. In: *Geophysical Research Letters* 42.13, pp. 5387–5394.

Gordon, A. L. and H. W. Taylor (1975). “Seasonal change of Antarctic sea ice cover”. In: *Science* 187.4174, pp. 346–347.

Gordon, A. L. et al. (2009). “Western Ross Sea Continental Slope Gravity Currents”. In: *Deep Sea Research Part II: Topical Studies in Oceanography* 56.13, pp. 796–817.

Gordon, A. L. et al. (2010). “A seasonal cycle in the export of bottom water from the Weddell Sea”. In: *Nature Geoscience* 3.8, p. 551.

Gordon, Arnold L (1981). “Seasonality of Southern Ocean sea ice”. In: *Journal of Geophysical Research: Oceans* 86.C5, pp. 4193–4197.

Graham, J. A. et al. (2013). “Seasonal variability of water masses and transport on the Antarctic continental shelf and slope in the southeastern Weddell Sea”. In: *Journal of Geophysical Research: Oceans* 118.4, pp. 2201–2214.

Haid, V. and R. Timmermann (2013). “Simulated heat flux and sea ice production at coastal polynyas in the southwestern Weddell Sea”. In: *Journal of Geophysical Research: Oceans* 118.5, pp. 2640–2652.

Hanawa, K. and L. D. Talley (2001). “Mode waters”. In: *International Geophysics Series* 77, pp. 373–386.

Hattermann, T. (2018). “Antarctic Thermocline Dynamics along a Narrow Shelf with Easterly Winds”. In: *Journal of Physical Oceanography* 48.10, pp. 2419–2443.

Hattermann, T. et al. (2012). “Two Years of Oceanic Observations Below the Fimbul Ice Shelf, Antarctica”. In: *Geophysical Research Letters* 39.12.

Hattermann, T. et al. (2014). “Eddy-Resolving Simulations of the Fimbul Ice Shelf Cavity Circulation: Basal Melting and Exchange with the Open Ocean”. In: *Ocean Modelling* 82, pp. 28–44.

Haumann, F. A. et al. (2016). “Sea-ice transport driving Southern Ocean salinity and its recent trends”. In: *Nature* 537.7618, p. 89.

Hazel, J. E. and A. L. Stewart (2019). “Are the Near-Antarctic Easterly Winds Weakening in Response to Enhancement of the Southern Annular Mode?” In: *Journal of Climate* 32.6, pp. 1895–1918.

Hellmer, H. H. (2004). “Impact of Antarctic ice shelf basal melting on sea ice and deep ocean properties”. In: *Geophysical Research Letters* 31.10.

Hellmer, H. H. et al. (2012). “Twenty-First-Century Warming of a Large Antarctic Ice-Shelf Cavity by a Redirected Coastal Current”. In: *Nature* 485.7397, pp. 225–228.

Hellmer, H. H. et al. (2017). “The fate of the southern Weddell Sea continental shelf in a warming climate”. In: *Journal of Climate* 30.12, pp. 4337–4350.

Heuzé, C. et al. (2013). “Southern Ocean bottom water characteristics in CMIP5 models”. In: *Geophysical Research Letters* 40.7, pp. 1409–1414.

Heywood, K. J. et al. (2014). “Ocean processes at the Antarctic continental slope”. In: *Philosophical Transactions of the Royal Society A: Mathematical, Physical and Engineering Sciences* 372.2019.

Heywood, K. J. et al. (2016). “Between the devil and the deep blue sea: the role of the Amundsen Sea continental shelf in exchanges between ocean and ice shelves”. In: *Oceanography* 29.4, pp. 118–129.

Hines, K. M., D. H. Bromwich, and G. J. Marshall (2000). “Artificial Surface Pressure Trends in the NCEP-NCAR Reanalysis over the Southern Ocean and Antarctica*”. In: *Journal of Climate* 13.22, pp. 3940–3952.

Hines, K. M. et al. (2011). “Development and testing of polar WRF. Part III: Arctic Land”. In: *Journal of Climate* 24.1, pp. 26–48.

Hogg, A. M. et al. (2015). “Recent trends in the Southern Ocean eddy field”. In: *Journal of Geophysical Research: Oceans* 120.1, pp. 257–267.

Holland, P. R., A. Jenkins, and D. M. Holland (2010). “Ice and ocean processes in the Bellingshausen Sea, Antarctica”. In: *Journal of Geophysical Research: Oceans* 115.C5.

Holland, P. R. and R. Kwok (2012). “Wind-Driven Trends in Antarctic Sea-Ice Drift”. In: *Nature Geoscience* 5.12, pp. 872–875.

Hughes, C. W., M. P. Meredith, and K. J. Heywood (1999). “Wind-Driven Transport Fluctuations Through the Drake Passage: A Southern Mode”. In: *Journal of Physical Oceanography* 29.8, pp. 1971–1992.

Jacobs, S. S. (1991). “On the Nature and Significance of the Antarctic Slope Front”. In: *Marine Chemistry* 35.1, pp. 9–24.

— (2004). “Bottom water production and its links with the thermohaline circulation”. In: *Antarctic Science* 16.4, pp. 427–437.

Jenkins, A. and A. Bombosch (1995). "Modeling the effects of frazil ice crystals on the dynamics and thermodynamics of ice shelf water plumes". In: *Journal of Geophysical Research: Oceans* 100.C4, pp. 6967–6981.

Jenkins, A., H. H. Hellmer, and D. M. Holland (2001). "The Role of Meltwater Advection in the formulation of conservative boundary conditions at an ice–ocean interface". In: *Journal of physical oceanography* 31.1, pp. 285–296.

Jenkins, A. et al. (2016). "Decadal ocean forcing and Antarctic ice sheet response: Lessons from the Amundsen Sea". In: *Oceanography* 29.4, pp. 106–117.

Jinlun, Z. and W.D. Hibler (1997). "On an efficient numerical method for modeling sea ice dynamics". In: *Oceanographic Literature Review* 11.44, p. 1235.

Jourdain, N. C. et al. (2017). "Ocean circulation and sea-ice thinning induced by melting ice shelves in the Amundsen Sea". In: *Journal of Geophysical Research: Oceans* 122.3, pp. 2550–2573.

Jullion, L. et al. (2010). "Wind-controlled export of Antarctic Bottom Water from the Weddell Sea". In: *Geophysical Research Letters* 37.9.

Jullion, L. et al. (2013). "Decadal freshening of the Antarctic Bottom Water exported from the Weddell Sea". In: *Journal of Climate* 26.20, pp. 8111–8125.

Kida, S. (2011). "The impact of open oceanic processes on the Antarctic Bottom Water outflows". In: *Journal of Physical Oceanography* 41.10, pp. 1941–1957.

Klinck, J.M. and M.S. Dinniman (2010). "Exchange across the shelf break at high southern latitudes". In: *Ocean Science* 6.2.

Kobayashi, S. et al. (2015). "The JRA-55 reanalysis: General specifications and basic characteristics". In: *Journal of the Meteorological Society of Japan.* 93.1, pp. 5–48.

Kobs, S. et al. (2014). "Novel monitoring of Antarctic ice shelf basal melting using a fiber-optic distributed temperature sensing mooring". In: *Geophysical Research Letters* 41.19, pp. 6779–6786.

Kodama, Y. and G. Wendler (1986). "Wind and temperature regime along the slope of Adélie Land, Antarctica". In: *Journal of Geophysical Research: Atmospheres* 91.D6, pp. 6735–6741.

Kwok, R., S. S. Pang, and S. Kacimi (2017). “Sea ice drift in the Southern Ocean: Regional patterns, variability, and trends”. In: *Elementa: Science of the Anthropocene* 5.

Langlais, C. E., S. R. Rintoul, and J. D. Zika (2015). “Sensitivity of Antarctic Circumpolar Current Transport and Eddy Activity to Wind Patterns in the Southern Ocean*”. In: *Journal of Physical Oceanography* 45.4, pp. 1051–1067.

Large, W. G., J. C. McWilliams, and S. C. Doney (1994). “Oceanic vertical mixing: A review and a model with a nonlocal boundary layer parameterization”. In: *Reviews of Geophysics* 32.4, pp. 363–403.

Lee, S.-K. et al. (2017). “Wind-driven ocean dynamics impact on the contrasting sea-ice trends around West Antarctica”. In: *Journal of Geophysical Research: Oceans* 122.5, pp. 4413–4430.

Legg, S. et al. (2009). “Improving oceanic overflow representation in climate models: the gravity current entrainment climate process team”. In: *Bulletin of the American Meteorological Society* 90.5, pp. 657–670.

Lenton, A. and R. J. Matear (2007). “Role of the Southern Annular Mode (SAM) in Southern Ocean CO2 Uptake”. In: *Global Biogeochemical Cycles* 21.2.

Leppäranta, M. (2011). *The drift of sea ice*. Springer Science & Business Media.

Lewis, E.L. and R.G. Perkin (1986). “Ice pumps and their rates”. In: *Journal of Geophysical Research: Oceans* 91.C10, pp. 11756–11762.

Losch, M. (2008). “Modeling ice shelf cavities in a z coordinate ocean general circulation model”. In: *Journal of Geophysical Research: Oceans* 113.C8.

Losch, M. et al. (2010). “On the formulation of sea-ice models. Part 1: Effects of different solver implementations and parameterizations”. In: *Ocean Modelling* 33.1-2, pp. 129–144.

Lüpkes, C. and G. Birnbaum (2005). “Surface drag in the Arctic marginal sea-ice zone: a comparison of different parameterisation concepts”. In: *Bound.-Layer Meteorol.* 117.2, pp. 179–211.

Mack, S. L. et al. (2017). “Dissolved iron transport pathways in the Ross Sea: Influence of tides and horizontal resolution in a regional ocean model”. In: *Journal of Marine Systems* 166, pp. 73–86.

Marshall, G. J. (2003). “Trends in the Southern Annular Mode from observations and reanalyses”. In: *Journal of Climate* 16.24, pp. 4134–4143.

Marshall, J. and T. Radko (2003). “Residual-Mean Solutions for the Antarctic Circumpolar Current and its Associated Overturning Circulation”. In: *Journal of Physical Oceanography* 33.11, pp. 2341–2354.

Marshall, J. and K. Speer (2012). “Closure of the meridional overturning circulation through Southern Ocean upwelling”. In: *Nature Geoscience* 5.3, pp. 171–180.

Matear, R. J. et al. (2015). “Sources of heterogeneous variability and trends in Antarctic sea-ice”. In: *Nature communications* 6, p. 8656.

Mathiot, P. et al. (2011). “Modelling the seasonal variability of the Antarctic Slope Current”. In: *Ocean Science* 7.4, pp. 445–532.

Mazloff, M. R., P. Heimbach, and C. Wunsch (2010). “An eddy-permitting Southern Ocean state estimate”. In: *Journal of Physical Oceanography* 40.5, pp. 880–899.

McDougall, T. J. and P. M. Barker (2011). “Getting started with TEOS-10 and the Gibbs Seawater (GSW) oceanographic toolbox”. In: *SCOR/IAPSO WG* 127, pp. 1–28.

McKee, D. C. et al. (2011). “Climate Impact on Interannual Variability of Weddell Sea Bottom Water”. In: *Journal of Geophysical Research: Oceans* 116.C5.

McWilliams, J. C., W. R. Holland, and J. H.S. Chow (1978). “A Description of Numerical Antarctic Circumpolar Currents”. In: *Dynamics of Atmospheres and Oceans* 2.3, pp. 213–291.

Meehl, G. A. (1991). “A reexamination of the mechanism of the semiannual oscillation in the Southern Hemisphere”. In: *Journal of Climate* 4.9, pp. 911–926.

Meijers, A.J.S. et al. (2016). “Wind-driven export of Weddell Sea slope water”. In: *Journal of Geophysical Research: Oceans* 121.10, pp. 7530–7546.

Meredith, M. P. and A. M. Hogg (2006). “Circumpolar Response of Southern Ocean Eddy Activity to a Change in the Southern Annular Mode”. In: *Geophysical Research Letters* 33.16.

Meredith, M. P. et al. (2008). “Evolution of the deep and bottom waters of the Scotia Sea, Southern Ocean, during 1995–2005”. In: *J. Climate* 21.13, pp. 3327–3343.

Millero, F.J. (1978). “Freezing point of sea water”. In: *Eighth Report of the Joint Panel of Oceanographic Tables and Standards* 6, pp. 29–31.

Moholdt, G., L. Padman, and H. A. Fricker (2014). “Basal mass budget of Ross and Filchner-Ronne ice shelves, Antarctica, derived from Lagrangian analysis of ICESat altimetry”. In: *Journal of Geophysical Research: Earth Surface* 119.11, pp. 2361–2380.

Munk, W. H. and E. Palmén (1951). “Note on the Dynamics of the Antarctic Circumpolar Current”. In: *Tellus A* 3.1.

Nakayama, Y. et al. (2014). “A numerical investigation of formation and variability of Antarctic Bottom Water off Cape Darnley, East Antarctica”. In: *Journal of Physical Oceanography* 44.11, pp. 2921–2937.

Newsom, E. R. et al. (2016). “Southern Ocean deep circulation and heat uptake in a high-resolution climate model”. In: *Journal of Climate* 29.7, pp. 2597–2619.

Nicholls K. W., Boehme L. Biuw M. and M. A. Fedak (2008). “Wintertime ocean conditions over the southern Weddell Sea continental shelf, Antarctica”. In: *Geophysical Research Letters* 35.21.

Nicholls, K. et al. (2009). “Ice-ocean processes over the continental shelf of the southern Weddell Sea, Antarctica: A review”. In: *Reviews of Geophysics* 47.3.

Nicholls, K.W. et al. (2001). “Oceanographic conditions south of Berkner Island, beneath Filchner-Ronne Ice Shelf, Antarctica”. In: *Journal of Geophysical Research: Oceans* 106.C6, pp. 11481–11492.

Nøst, O. A. et al. (2011). “Eddy Overturning of the Antarctic Slope Front Controls Glacial Melting in the Eastern Weddell Sea”. In: *Journal of Geophysical Research: Oceans (1978–2012)* 116.C11.

Ohshima, K. I. et al. (2013). “Antarctic Bottom Water production by intense sea-ice formation in the Cape Darnley polynya”. In: *Nature Geoscience* 6.3, pp. 235–240.

Olbers, D. et al. (2004). “The dynamical balance, transport and circulation of the Antarctic Circumpolar Current”. In: *Antarctic science* 16.04, pp. 439–470.

Orsi, A. H., T. Whitworth, and W. D. Nowlin (1995). “On the Meridional Extent and Fronts of the Antarctic Circumpolar Current”. In: *Deep Sea Research Part I: Oceanographic Research Papers* 42.5, pp. 641–673.

Orsi, A. H. et al. (2001). “Cooling and ventilating the abyssal ocean”. In: *Geophysical Research Letters* 28.15, pp. 2923–2926.

Orsi, A.H., G.C. Johnson, and J.L. Bullister (1999). “Circulation, mixing, and production of Antarctic Bottom Water”. In: *Progress in Oceanography* 43.1, pp. 55–109.

Padman, L. et al. (2002). “A new tide model for the Antarctic ice shelves and seas”. In: *Annals of Glaciology* 34.1, pp. 247–254.

Padman, L. et al. (2009). “Tides of the northwestern Ross Sea and their impact on dense outflows of Antarctic Bottom Water”. In: *Deep Sea Research Part II: Topical Studies in Oceanography* 56.13, pp. 818–834.

Parish, T. R. and D. H. Bromwich (1997). “On the forcing of seasonal changes in surface pressure over Antarctica”. In: *Journal of Geophysical Research: Atmospheres* 102.D12, pp. 13785–13792.

— (2007). “Reexamination of the near-surface airflow over the Antarctic continent and implications on atmospheric circulations at high southern latitudes”. In: *Monthly Weather Review* 135.5, pp. 1961–1973.

Parish, T. R., P. Pettré, and G. Wendler (1993). “The influence of large-scale forcing on the katabatic wind regime at Adélie Land, Antarctica”. In: *Meteorology and Atmospheric Physics* 51.3-4, pp. 165–176.

Parish, T. R. and K. T. Waight III (1987). “The Forcing of Antarctic Katabatic Winds”. In: *Monthly Weather Review* 115.10, pp. 2214–2226.

Petrich, C. and H. Eicken (2017). “Overview of sea ice growth and properties”. In: *Sea ice*, pp. 1–41.

Powers, J. G. et al. (2003a). “Real-time mesoscale modeling over Antarctica: The Antarctic mesoscale prediction system”. In: *Bull. Am. Meteorol. Soc.* 84.11, pp. 1533–1545.

— (2003b). “Real-time mesoscale modeling over Antarctica: The Antarctic mesoscale prediction system”. In: *Bulletin of the American Meteorological Society* 84.11, pp. 1533–1545.

Powers, J. G. et al. (2012). “A decade of Antarctic science support through AMPS”. In: *Bulletin of the American Meteorological Society* 93.11, pp. 1699–1712.

Pritchard H. Ligtenberg, S.R.M. Fricker H.A. Vaughan D.G. Van den Broeke M.R. and L. Padman (2012). “Antarctic ice-sheet loss driven by basal melting of ice shelves”. In: *Nature* 484.7395, p. 502.

Purkey, S. G. and G. C. Johnson (2010). “Warming of Global Abyssal and Deep Southern Ocean Waters Between the 1990s and 2000s: Contributions to Global Heat and Sea Level Rise Budgets”. In: *Journal of Climate* 23.23, pp. 6336–6351.

Renfrew, I. A. et al. (2002). “A comparison of surface layer and surface turbulent flux observations over the Labrador Sea with ECMWF analyses and NCEP reanalyses”. In: *Journal of Physical Oceanography* 32.2, pp. 383–400.

Renner, A. H.H. and V. Lytle (2007). “Sea-ice thickness in the Weddell Sea, Antarctica: a comparison of model and upward-looking sonar data”. In: *Annals of Glaciology* 46, pp. 419–427.

Rienecker, M. M. et al. (2011). “MERRA: NASA’s modern-era retrospective analysis for research and applications”. In: *Journal of climate* 24.14, pp. 3624–3648.

Rignot, E. et al. (2013). “Ice-shelf melting around Antarctica”. In: *Science* 341.6143, pp. 266–270.

Rintoul, S.R. (2010). “Antarctic circumpolar current”. In: *Ocean Currents: A derivative of the encyclopedia of Ocean Sciences* 196.

Rocha, C. B. et al. (2016). “Mesoscale to submesoscale wavenumber spectra in Drake Passage”. In: *Journal of Physical Oceanography* 46.2, pp. 601–620.

Saha, S. et al. (2010). “The NCEP climate forecast system reanalysis”. In: *Bulletin of the American Meteorological Society* 91.8, pp. 1015–1057.

Sallée, J. B., K. G. Speer, and S. R. Rintoul (2010). “Zonally Asymmetric Response of the Southern Ocean Mixed-Layer Depth to the Southern Annular Mode”. In: *Nature Geoscience* 3.4, pp. 273–279.

Schlitzer, R. (2002). “eWOCE-Electronic Atlas of WOCE Data, Alfred Wegener Institute for Polar and Marine Research, Bremerhaven”. In:

Schmidtko, S. et al. (2014). “Multi-Decadal Warming of Antarctic Waters”. In: *Science* 346.6214, pp. 1227–1231.

Semtner, A. J. (1976). “A model for the thermodynamic growth of sea ice in numerical investigations of climate”. In: *Journal of Physical Oceanography* 6.3, pp. 379–389.

Shindell, D. T. and G. A. Schmidt (2004). "Southern Hemisphere climate response to ozone changes and greenhouse gas increases". In: *Geophysical Research Letters* 31.18.

Simmonds, I. and D. A. Jones (1998). "The mean structure and temporal variability of the semiannual oscillation in the southern extratropics". In: *International Journal of Climatology* 18.5, pp. 473–504.

Smith, S. D., R. D. Muench, and C. H. Pease (1990). "Polynyas and leads: An overview of physical processes and environment". In: *Journal of Geophysical Research: Oceans* 95.C6, pp. 9461–9479.

Smith, S. R., P. J. Hughes, and M. A. Bourassa (2011). "A comparison of nine monthly air–sea flux products". In: *International Journal of Climatology* 31.7, pp. 1002–1027.

Snow, K. et al. (2015). "Sensitivity of abyssal water masses to overflow parameterisations". In: *Ocean Modelling* 89, pp. 84–103.

Spence, P. et al. (2014). "Rapid Subsurface Warming and Circulation Changes of Antarctic Coastal Waters by Poleward Shifting Winds". In: *Geophysical Research Letters* 41.13, pp. 4601–4610.

St-Laurent, P., J. M. Klinck, and M. S. Dinniman (2013). "On the role of coastal troughs in the circulation of warm Circumpolar Deep Water on Antarctic shelves". In: *Journal of Physical Oceanography* 43.1, pp. 51–64.

Stammerjohn, S.E. et al. (2008). "Trends in Antarctic annual sea ice retreat and advance and their relation to El Niño–Southern Oscillation and Southern Annular Mode variability". In: *Journal of Geophysical Research: Oceans* 113.C3.

Stark, J. D. et al. (2007). "OSTIA: An operational, high resolution, real time, global sea surface temperature analysis system". In: *Oceans 2007-Europe*. IEEE, pp. 1–4.

Stewart, A. L., A. Klocker, and D. Menemenlis (2018). "Circum-Antarctic Shoreward Heat Transport Derived From an Eddy-and Tide-Resolving Simulation". In: *Geophysical Research Letters* 45, pp. 834–845.

Stewart, A. L. and A. F. Thompson (2012). "Sensitivity of the ocean's deep overturning circulation to easterly Antarctic winds". In: *Geophysical Research Letters* 39.18.

— (2013). "Connecting Antarctic cross-slope exchange with Southern Ocean overturning". In: *Journal of Physical Oceanography* 43.7, pp. 1453–1471.

Stewart, A. L. and A. F. Thompson (2015a). “Eddy-mediated transport of warm Circumpolar Deep Water across the Antarctic shelf break”. In: *Geophysical Research Letters* 42.2, pp. 432–440.

— (2016). “Eddy generation and jet formation via dense water outflows across the Antarctic continental slope”. In: *Journal of Physical Oceanography* 46.12, pp. 3729–3750.

Stewart, A.L. and A.F. Thompson (2015b). “The neutral density temporal residual mean overturning circulation”. In: *Ocean Modelling* 90, pp. 44–56.

Stewart, K.D. et al. (2017). “Vertical resolution of baroclinic modes in global ocean models”. In: *Ocean Modelling* 113, pp. 50–65.

Stössel, A., Z. Zhang, and T. Vihma (2011). “The Effect of Alternative Real-Time Wind Forcing on Southern Ocean Sea Ice Simulations”. In: *Journal of Geophysical Research: Oceans (1978–2012)* 116.C11.

Su, Z., A. L. Stewart, and A. F. Thompson (2014). “An idealized model of Weddell Gyre export variability”. In: *Journal of Physical Oceanography* 44.6, pp. 1671–1688.

Swart, N. C. and J. C. Fyfe (2012). “Observed and simulated changes in the Southern Hemisphere surface westerly wind-stress”. In: *Geophysical Research Letters* 39.16.

Tastula, E.-M., T. Vihma, and E. L. Andreas (2012). “Evaluation of polar WRF from modeling the atmospheric boundary layer over Antarctic sea ice in autumn and winter”. In: *Monthly Weather Review* 140.12, pp. 3919–3935.

Thoma, M. et al. (2008). “Modelling Circumpolar Deep Water Intrusions on the Amundsen Sea Continental Shelf, Antarctica”. In: *Geophysical Research Letters* 35.18.

Thompson, A. F. et al. (2014). “Eddy Transport as a Key Component of the Antarctic Overturning Circulation”. In: *Nature Geoscience* 7.12, pp. 879–884.

Thompson, A. F. et al. (2018). “The Antarctic Slope Current in a Changing Climate”. In: *Reviews of Geophysics* 56.4, pp. 741–770.

Thompson, D. W. J. and S. Solomon (2002). “Interpretation of recent Southern Hemisphere climate change”. In: *Science* 296.5569, pp. 895–899.

Timmermann, R. (2010). “RTOPO-1: A consistent dataset for Antarctic ice shelf topography and global ocean bathymetry”. In: *EGU General Assembly Conference Abstracts*. Vol. 12, p. 5304.

Timmermann, R., A. Beckmann, and H. Hellmer (2002). “Simulations of ice-ocean dynamics in the Weddell Sea 1. Model configuration and validation”. In: *Journal of Geophysical Research: Oceans* 107.C3.

Timmermann, R., S. Danilov, and J. Schröter (2009). “Validation of a global finite element sea ice-ocean model”. In:

Timmermann, R., Q. Wang, and H.H. Hellmer (2012). “Ice-shelf basal melting in a global finite-element sea-ice/ice-shelf/ocean model”. In: *Annals of Glaciology* 53.60, pp. 303–314.

Toggweiler, J. R., J. L. Russell, and S. R. Carson (2006). “Midlatitude westerlies, atmospheric CO2, and climate change during the ice ages”. In: *Paleoceanography* 21.2.

Toggweiler, J.R. (2008). “Origin of the 100,000-year timescale in Antarctic temperatures and atmospheric CO2”. In: *Paleoceanography* 23.2.

Turner, J. et al. (2005). “Antarctic Climate Change During the Last 50 years”. In: *International Journal of Climatology* 25.3, pp. 279–294.

Turner, J. et al. (2013). “The Amundsen Sea Low”. In: *International Journal of Climatology* 33.7, pp. 1818–1829.

Turner, J. et al. (2017). “Atmosphere-ocean-ice interactions in the Amundsen Sea Embayment, West Antarctica”. In: *Reviews of Geophysics* 55.1, pp. 235–276.

Wang, G., W. Cai, and A. Purich (2014). “Trends in Southern Hemisphere Wind-Driven Circulation in CMIP5 Models Over the 21st Century: Ozone Recovery Versus Greenhouse Forcing”. In: *Journal of Geophysical Research: Oceans* 119.5, pp. 2974–2986.

Wang, Q. et al. (2012). “On the Impact of Wind Forcing on the Seasonal Variability of Weddell Sea Bottom Water transport”. In: *Geophysical Research Letters* 39.6.

Wang, Q. et al. (2013). “Enhanced cross-shelf exchange by tides in the western Ross Sea”. In: *Geophysical Research Letters* 40.21, pp. 5735–5739.

Whitworth, T. and A.H. Orsi (2006). “Antarctic Bottom Water production and export by tides in the Ross Sea”. In: *Geophysical Research Letters* 33.12.

Whitworth III, T. (1983). “Monitoring the Transport of the Antarctic Circumpolar Current at Drake Passage”. In: *Journal of Physical Oceanography* 13.11, pp. 2045–2057.

Zhang, J. and W.D. Hibler (1997). “On an efficient numerical method for modeling sea ice dynamics”. In: *Journal of Geophysical Research: Oceans* 102.C4, pp. 8691–8702.

Zhang, Z. et al. (2015). “The Role of Wind Forcing from Operational Analyses for the Model Representation of Antarctic Coastal Sea Ice”. In: *Ocean Modelling* 94, pp. 95–111.

Zhou, Q. et al. (2014). “Wind-Driven Spreading of Fresh Surface Water Beneath Ice Shelves in the Eastern Weddell Sea”. In: *Journal of Geophysical Research: Oceans* 119.6, pp. 3818–3833.

Zika, J. D. et al. (2013). “Acceleration of the Antarctic Circumpolar Current by Wind Stress Along the Coast of Antarctica”. In: *Journal of Physical Oceanography* 43.12, pp. 2772–2784.